

AD-A247 332



2

# NAVAL POSTGRADUATE SCHOOL Monterey, California



DTIC  
ELECTE  
MAR 12 1992  
S B D

## THESIS

ANALYSIS OF RADIATION DAMAGED AND ANNEALED GALLIUM ARSENIDE AND INDIUM PHOSPHIDE SOLAR CELLS USING DEEP LEVEL TRANSIENT SPECTROSCOPY TECHNIQUES

by

Dimas Pinzon, Jr.

March 1991

Thesis Advisor:

Sherif Michael

Approved for public release; distribution is unlimited

92 3 10 143

92-06412



UNCLASSIFIED

SECURITY CLASSIFICATION OF THIS PAGE

REPORT DOCUMENTATION PAGE				Form Approved OMB No. 0704-0188	
1a. REPORT SECURITY CLASSIFICATION <b>UNCLASSIFIED</b>			1b. RESTRICTIVE MARKINGS		
2a. SECURITY CLASSIFICATION AUTHORITY			3. DISTRIBUTION / AVAILABILITY OF REPORT Approved for public release; distribution is unlimited		
2b. DECLASSIFICATION / DOWNGRADING SCHEDULE			4. PERFORMING ORGANIZATION REPORT NUMBER(S)		
4. PERFORMING ORGANIZATION REPORT NUMBER(S)			5. MONITORING ORGANIZATION REPORT NUMBER(S)		
6a. NAME OF PERFORMING ORGANIZATION Naval Postgraduate School		6b. OFFICE SYMBOL (if applicable) EC	7a. NAME OF MONITORING ORGANIZATION Naval Postgraduate School		
6c. ADDRESS (City, State, and ZIP Code) Monterey, CA 93943-5000			7b. ADDRESS (City, State, and ZIP Code) Monterey, CA 93943-5000		
8a. NAME OF FUNDING / SPONSORING ORGANIZATION		8b. OFFICE SYMBOL (if applicable)	9. PROCUREMENT INSTRUMENT IDENTIFICATION NUMBER		
8c. ADDRESS (City, State, and ZIP Code)			10. SOURCE OF FUNDING NUMBERS		
		PROGRAM ELEMENT NO.	PROJECT NO.	TASK NO.	WORK UNIT ACCESSION NO.
11. TITLE (Include Security Classification) ANALYSIS OF RADIATION DAMAGED AND ANNEALED GAL ARSENIDE AND INDIUM PHOSPHIDE SOLAR CELLS USING DEEP LEVEL TRANSIENT SPECTROSCOPY TECHNIQUES					
12. PERSONAL AUTHOR(S) PINZON, Jr., Dimas					
13a. TYPE OF REPORT Master's Thesis		13b. TIME COVERED FROM _____ TO _____		14. DATE OF REPORT (Year, Month, Day) 1991 March	15. PAGE COUNT 181
16. SUPPLEMENTARY NOTATION The views expressed in this thesis are those of the author and do not reflect the official policy or position of the Department of Defense or the US Government.					
17. COSATI CODES			18. SUBJECT TERMS (Continue on reverse if necessary and identify by block number)		
FIELD	GROUP	SUB-GROUP	Radiation effects on solar cells; DLTS; annealing of solar cells; gallium arsenide; indium phosphide		
19. ABSTRACT (Continue on reverse if necessary and identify by block number) Degradation of solar cell performance from radiation damage was found to be reversed through annealing processes. The mechanism behind the degradation and recovery is based on deep-level traps, or defects, in the lattice structure of the solar cell. Through a process known as Deep Level Transient Spectroscopy (DLTS), a correlation can be made between damage/recovery and trap energy level/concentration of the cell. Gallium Arsenide (GaAs) and Indium Phosphide (InP) solar cells were subjected to 1 MeV electron irradiation by a Dynamitron linear acceleration at two fluence levels of 1E14 and 1E14 electrons/cm <sup>2</sup> . The process of annealing included thermal annealing at 90°C with forward bias current and thermal annealing alone (for GaAs). After each cycle, DLTS measurements were taken to determine the energy level of the traps and their concentration. Multiple cycles of irradiation, annealing and DLTS were					
20. DISTRIBUTION / AVAILABILITY OF ABSTRACT <input checked="" type="checkbox"/> UNCLASSIFIED/UNLIMITED <input type="checkbox"/> SAME AS RPT. <input type="checkbox"/> DTIC USERS			21. ABSTRACT SECURITY CLASSIFICATION <b>UNCLASSIFIED</b>		
22a. NAME OF RESPONSIBLE INDIVIDUAL MICHAEL, Sherif			22b. TELEPHONE (Include Area Code) 408-646-2252		22c. OFFICE SYMBOL EC/Mi

UNCLASSIFIED

SECURITY CLASSIFICATION OF THIS PAGE

19. cont.

performed to observe the correlation between degradation and recovery to trap energy level and concentration.

The results show that the lower energy level traps are associated with the recovery of the cells while the higher level traps are associated with the overall permanent degradation of the cells. Applying this information to future research could allow for significant increases in satellite mission life and potentially increase mission payload.

Approved for public release; distribution is unlimited

Analysis of Radiation Damaged and Annealed  
Gallium Arsenide and Indium Phosphide Solar Cells  
Using Deep Level Transient Spectroscopy Techniques

by

Dimas Pinzon, Jr.  
Major, United States Marine Corps  
B.S., Polytechnic Institute of Brooklyn, 1975  
M.S., University of Southern California, 1985

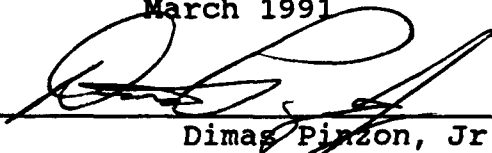
Submitted in partial fulfillment of the  
requirements for the degree of

MASTER OF SCIENCE IN ELECTRICAL ENGINEERING  
(SPACE SYSTEMS)

from the

NAVAL POSTGRADUATE SCHOOL  
March 1991

Author:

  
Dimas Pinzon, Jr.

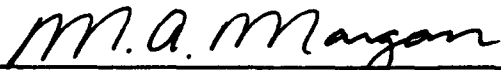
Approved by:



Sherif Michael, Thesis Advisor



Rudolf Panholzer, Second Reader



Michael A. Morgan, Chairman  
Department of Electrical and Computer Engineering



<b>Accession For</b>	
NTIS GRA&I	<input checked="" type="checkbox"/>
DTIC TAB	<input type="checkbox"/>
Unannounced	<input type="checkbox"/>
Justification	
By _____	
Distribution/	
Availability Codes	
Dist	Avail and/or
A-1	Special

## ABSTRACT

Degradation of solar cell performance from radiation damage was found to be reversed through annealing processes. The mechanisms behind the degradation and recovery is based on deep-level traps, or defects, in the lattice structure of the solar cell. Through a process known as Deep Level Transient Spectroscopy (DLTS), a correlation can be made between damage/recovery and trap energy level/concentration of the cell. Gallium Arsenide (GaAs) and Indium Phosphide (InP) solar cells were subjected to 1 MeV electron irradiation by a Dynamitron linear acceleration at two fluence levels of  $1E14$  and  $1E15$  electrons/cm<sup>2</sup>. The process of annealing included thermal annealing at 90°C with forward bias current and thermal annealing alone (for GaAs). After each cycle, DLTS measurements were taken to determine the energy level of the traps and their concentration. Multiple cycles of irradiation, annealing and DLTS were performed to observe the correlation between degradation and recovery to trap energy level and concentration.

The results show that the lower energy level traps are associated with the recovery of the cells while the higher level traps are associated with the overall permanent degradation of the cells. Applying this information to future research could allow for significant increases in satellite mission life and potentially increase mission payload.

## TABLE OF CONTENTS

I.	INTRODUCTION.....	1
A.	BACKGROUND.....	1
B.	RESEARCH PURPOSES.....	3
II.	PHOTOVOLTAIC.....	6
A.	SEMICONDUCTOR THEORY.....	6
1.	Bonding Mechanisms.....	6
2.	Lattice Structure.....	7
3.	Energy Bands and Band Gap.....	10
4.	Temperature Effects.....	13
B.	PHOTOVOLTAIC EFFECT.....	15
1.	Theory of Solar Cells.....	15
2.	Efficiency.....	18
3.	Factors Affecting Solar Cell Efficiency..	23
a.	Bandgap Energy.....	24
b.	Temperature.....	24
c.	Recombination.....	27
C.	CARRIER TRANSPORT.....	27
D.	P-N JUNCTION.....	30
E.	P-N JUNCTION CAPACITANCE.....	32
III.	SOLAR CELL RADIATION DAMAGE.....	34
A.	ENVIRONMENT.....	34
B.	THEORY OF RADIATION DAMAGE.....	38
C.	LATTICE STRUCTURE DAMAGE.....	40
IV.	THEORY OF ANNEALING.....	43
A.	RADIATION EFFECTS.....	43

B.	RADIATION DEFECTS IN SOLAR CELLS -- DAMAGE EQUIVALENCE.....	47
C.	SOLAR CELL ANNEALING.....	48
D.	PREVIOUS ANNEALING RESEARCH.....	49
V.	DEEP LEVEL TRANSIENT SPECTROSCOPY.....	51
A.	DEEP-LEVEL TRANSIENT SPECTROSCOPY THEORY.....	51
B.	DATA AND EQUATIONS.....	57
VI.	GALLIUM ARSENIDE SOLAR CELLS.....	65
A.	GaAs CELL CHARACTERISTICS.....	65
B.	EXPERIMENT OBJECTIVE AND PLAN.....	66
C.	EXPERIMENTAL PROCEDURE AND RESULTS.....	68
D.	DLTS.....	69
E.	CONCLUSIONS.....	70
VII.	INDIUM PHOSPHIDE SOLAR CELLS.....	73
A.	InP CELL CHARACTERISTICS.....	73
B.	EXPERIMENT OBJECTIVE AND PLAN.....	75
C.	EXPERIMENTAL PROCEDURE AND RESULTS.....	75
D.	DLTS.....	77
VIII.	CONCLUSIONS AND RECOMMENDATIONS.....	85
APPENDIX A	PHYSICAL AND ELECTRICAL PROPERTIES OF SOME IMPORTANT SEMICONDUCTORS [REF. 5].....	87
APPENDIX B	I-V CURVES FOR MULTIPLE CYCLES OF IRRADIATED AND ANNEALED GaAs SOLAR CELLS...	91
APPENDIX C	OPEN CIRCUIT VOLTAGE, SHORT CIRCUIT CURRENT, AND MAXIMUM POWER NORMALIZED PLOTS FOR GaAs SOLAR CELLS.....	110
APPENDIX D	I-V CURVES FOR MULTIPLE CYCLES OF IRRADIATED AND ANNEALED InP SOLAR CELLS....	132

APPENDIX E OPEN CIRCUIT VOLTAGE, SHORT CIRCUIT CURRENT  
AND MAXIMUM POWER NORMALIZED PLOTS FOR  
InP SOLAR CELLS.....148

APPENDIX F EQUATIONS AN SAMPLE CALCULATIONS FOR DLTS ON  
InP CELL 1073 ALONG WITH ENERGY AND CAPTURE  
CROSS SECTION PLOTS.....155

REFERENCES.....169

INITIAL DISTRIBUTION LIST.....172



## ACKNOWLEDGEMENT

As we go through life, there are a few special people that share our trials and tribulations. It is for this reason, that I wish to express my heartfelt thanks to those who worked with me on this research.

First, to Dr. Sherif Michael who introduced me to the field of solar cell research. Throughout his busy schedule there was always time for me. His confidence and support made it all possible. To Dr. Rudolf Panholzer, for convincing me after our first chance meeting to enter the Space curriculum. His inspiration helped me to achieve my goals. To Dr. Linda Halle, who literally taught me about Deep Level Transient Spectroscopy. The challenges of this research were always met and overcome through her dedication and perseverance. She exemplifies her profession. To Karen Callaghan who pulled it all together. Her exceptional work and guidance through the past two and a half years helped make this a worthwhile experience. Finally, and most of all, to my wife Maureen, fifteen years of unwaivering love and support -- she is the wind beneath my wings.

I therefore dedicate this thesis to them, for it is as much theirs' as it is mine.

## I. INTRODUCTION

### A. BACKGROUND

Since 1839 when the first photovoltaic effect was announced by Bequerel, solar energy has become an ever-increasing facet in man's technology. The development of the first silicon solar cell in 1952 by Bell Labs plunged us into a new age of reliable power generation particularly suited for space ventures where the sun presents an inexhaustible source of energy.

Solar cells are the semiconductor devices which convert solar energy to electrical power using the photovoltaic effect. The majority of spacecraft orbiting earth rely on solar power for their payload power requirements and these devices have become an integral part of the space program. As a consequence, solar cells have been the subject of vast studies to increase efficiency of power output and sustainability in the space environment.

The advent of the space program created a great need for independent power sources for spacecraft. The success of the solar cell came about with the Vanguard satellite in 1958 and as power demand increased with technology advances solar cell use quickly escalated. Solar cells present the most viable alternative for spacecraft power generation based on reliability and cost. Over the past four decades, solar cell

technology has advanced to such a degree that the power now provided by solar array designs are measured in kilowatts.

A problem, however, was to be encountered. When the United States exploded an atomic bomb within the Van Allen Belt in 1962 little was known about the effects of radiation on solar cells. Twenty-four days after the explosion three of the satellites orbiting earth failed to operate due to power loss. The radiation effects halted the photovoltaic energy conversion of the cells. Despite the inexhaustible source of energy presented by the sun, the power output of the cells were limited over the life of the spacecraft -- limited to the extent that spacecraft design is based on the end of life (EOL) power of the solar arrays. The radiation effects to include damage to the lattice structure of the cell and its compensation, have become a critical issue causing extensive research in the area.

To date, compensation of radiation damage has been minimal. The n on p cell was found to be more resistive to radiation effects than the standard p on n. A coverglass with varying thickness was utilized and provided limited shielding from bombarding electrons. However, these efforts did not extend the life of the solar cell to any appreciable extent. Development of other III-V type cells (Gallium Arsenide and Indium Phosphide) provided greater hardness against radiation. The cost of manufacture versus life extension has prohibited their wide use. What is needed is a process which would

actually reverse the damage of radiation in the cells. If this could be accomplished while on orbit, the process would present the most attractive alternative to lost spacecraft. It would extend the life of the spacecraft, decrease design requirements and increase payload. The cost-benefit would be most attractive.

The potential for on-orbit radiation damage recovery became apparent when an annealing process was found to restore the electrical degradation experienced when the cells were subjected to radiation damage [Ref. 1]. The recovery was significant enough that the end of life (EOL) of a spacecraft could be extended many times its present capability. This information opens the way for greater operational endeavors. The implications are that spacecraft can operate within the Van Allen Belts for extended periods of time staying off the long-term damaging effects of radiation on the cells (i.e., the Global Positioning System which passes through the Van Allen Belts). Thus with this process, the overall cost benefits are realizable.

#### **B. RESEARCH PURPOSES**

This research is designed to provide insight into the mechanism behind the structure deformation and reformation of Gallium Arsenide (GaAs) and Indium Phosphide (InP) solar cells through the use of Deep Level Transient Spectroscopy (DLTS). Preliminary investigation into the feasibility of annealing electron-damaged solar cells has been established [Ref. 2].

Research has established that after irradiation at a fluence level of between  $1E14$  and  $1E15$   $\text{el}/\text{cm}^2$ , the effects of damage caused by trapped electrons was reversed [Ref. 2] in GaAs and InP solar cells.

Clark [Ref. 1] and Staats [Ref. 3] conducted single annealing experiments to determine the optimum mechanism for recovery of radiation-damaged GaAs cells. Cypranowski [Ref. 2] continued the research for InP cells as well as investigating multiple cycles of radiation and annealing on GaAs and InP cells. This research will explore the forward biased current and heat annealing of GaAs and InP cells that have been electron damaged by looking into the lattice structure, via DLTS, to determine the mechanisms that affect the damage and annealing process.

Beginning with Chapter II, fundamentals of semiconductor theory and the photovoltaic effect are introduced. This information provides a foundation on which the thesis is based. Other important concepts such as p-n junction and carrier transport are also discussed. Chapter III deals with radiation effects on solar cells and the environment in which the cells must operate. Continuing the process of radiation damage, Chapter IV discusses the annealing for solar cell recovery and outlines previous annealing research. The mechanism behind damage and recovery is further brought out in Chapter V with the discussion of deep level transient spectroscopy and its relationship to solar cell measurement

parameters. The experiment is discussed in detail for GaAs in Chapter VI and InP in Chapter VII with conclusions and recommendations following in Chapter VIII. All pertinent graphs and equations are found within the appendices.

## II. PHOTOVOLTAIC

### A. SEMICONDUCTOR THEORY

In order to understand the process of photovoltaics and solar cells, i.e., the nature of electronic conduction, it is necessary that some fundamentals concerning the material involved are formed. To this end, some basics of semiconductor theory, the building block of solar cells will be dealt with.

The electrical properties and physical characteristics of a material which lie intermediate between metals and insulators characterize a class of material known as semiconductors.

#### 1. Bonding Mechanisms

Chemically, semiconductors have four valence electrons. Since there are about eight valence states with approximately the same energy level, the valence shell is only half filled. Therefore, the four remaining empty states are filled by one atom sharing one electron with each of four neighboring atoms, completing the valence shell. This bonding is referred to as covalent. It is the mechanism behind silicon crystals. For III-V compounds, i.e., GaAs and InP, the bonding mechanisms is a mixture of covalent and ionic bonding (the transfer of one or more electrons from an

electropositive element to an electronegative element, creating a positive and negative ion).

The binding energy that is associated with covalent bonding is on the order of a few electron volts per atom while the binding energy associated with ionic bonds (electrostatic attraction of oppositely charged ions) is slightly higher. Insulation or dielectrics are characterized by this binding energy.

For silicon, however, the covalent bonds are weaker than that of carbon because the valence electrons are in shells farther from the nucleus. Therefore, the bonding energy is lower. The same holds true for III-V compounds. The bonding energy for GaAs and InP are higher however, than silicon because of their ionic bonds. This becomes significant when band gap energy and its relation to the light spectrum is discussed. This weaker bonding distinguishes the semiconductor from the insulator. It also distinguishes the semiconductor from metals because the covalent and ionic bonding energy is greater than that of metallic bonding.

## **2. Lattice Structure**

A crystalline solid is characterized by an orderly, perfectly periodic array of atoms known as the lattice structure. The basic building block that defines the lattice structure of a crystal is the unit cell. By translating the unit cell, a translational symmetric lattice is generated. In other words, the symmetry of the lattice is unchanged relative

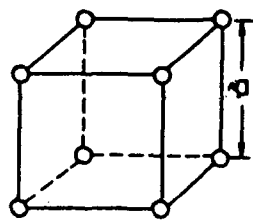


to different coordinates. Because silicon, GaAs and InP are crystalline in nature, we can exploit the symmetric characteristics when dealing with energy band gaps.

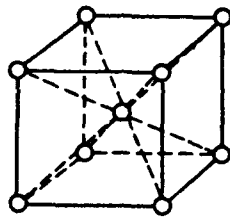
Figure 2-1 shows the unit cell of silicon and GaAs. Length (a) is known as the lattice constant.

When silicon crystallizes, it does so in a diamond structure in which each atom is bound to its four nearest neighbors in a tetrahedral arrangement. For the III-V compounds, the atom of an element from the third group of the periodic table is surrounded by four neighboring atoms of an element from the fifth group and conversely, so that the number of atoms from each group is the same. By transferring an electron from a fifth group atom to a third group atom, each lattice site becomes occupied by an ion surrounded by four oppositely charged ions in a tetrahedral arrangement similar to the diamond structure of silicon. This arrangement is known as a zinc-blende structure.

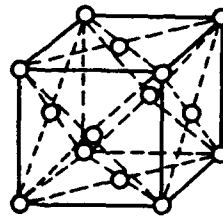
The lattice structure plays an important role in semiconductor devices particularly in the generation of band gaps. The atoms of the lattice are in a state of constant vibration. As a consequence, the atom imparts energy to the electrons surrounding it. The interaction of the electron and the vibrational energy contributes to the formation of the energy bands and the band gap by causing the discrete energy levels of the atom to spread out. This mechanism influences



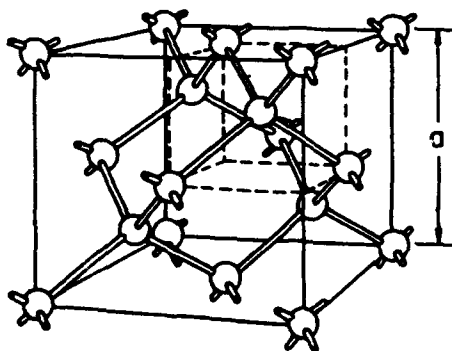
SIMPLE CUBIC  
(P, etc)



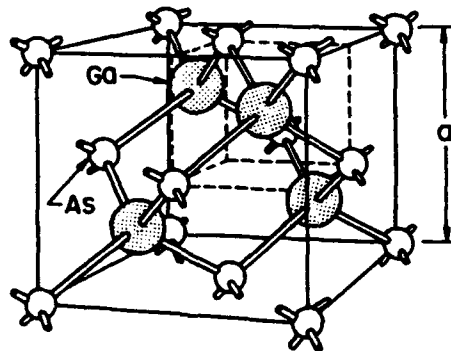
BODY-CENTERED CUBIC  
(Na, W, etc)



FACE-CENTERED CUBIC  
(Al, Au, etc)



DIAMOND  
(C, Ge, Si, etc)



ZINCBLLENDE  
(GaAs, GaP, etc)

Figure 2-1. Some important unit cells (direct lattices) and their representative elements or compounds;  $a$  is the lattice constant. [from Ref. 5:p. 9]

the electrical and thermal conductivity of the crystal and is the chief characteristic of the semiconductor.

### 3. Energy Bands and Band Gap

As a direct consequence of translational symmetry, the discrete energy levels of the atom spread out to form two major energy bands -- the valance band and the conductor band; each one with its own discrete electron levels. The valance bands are those occupied by the electrons at  $0^{\circ}\text{K}$  while the conduction bands are empty. At  $0^{\circ}\text{K}$ , a semiconductor has no delocalized electrons; all electrons are bound to individual atoms [Ref. 4:p. 52]. Hence, the number of electrons available to carry current are almost nonexistent.

Separating the two major energy bands is a gap of forbidden energy levels, better known as the bandgap. In order for an electron to escape the valence band and cross the band gap into the conduction band to carry current, it must absorb enough energy to raise its energy level to that of the conduction band. It must possess sufficient energy greater than the bandgap energy. Figure 2-2 is a diagrammatical representation of the energy bands and the bandgap. The energy gap (band gap) for semiconductor devices ranges from 0 to 2.5 eV. At room temperature ( $300^{\circ}\text{K}$ ) and under normal atmosphere, the values of the bandgap are 1.12 eV for silicon, 1.42 eV for Gallium Arsenide and 1.35 eV for Indium Phosphate [Ref. 5:p. 15 and Ref. 6:p. 42].

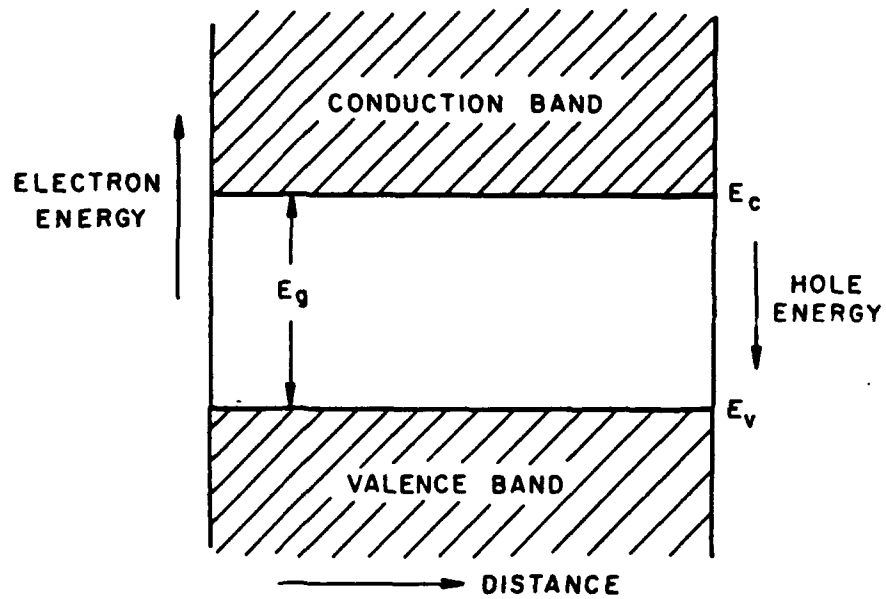


Figure 2-2. Simplified band diagram of a semiconductor  
[from Ref. 5:p. 15]

Once electrons cross the gap to the conduction band, they move freely and thereby carry current. The hole left behind in the valence band is filled by neighboring electrons, in effect causing the hole to move around the atoms. This motion can be considered the movement of a positive charge. The net result is that current carried through the semiconductor.

What distinguishes the semiconductor from an insulator is the fact that the bandgap energy is small ( $0 < E_g < 2.5\text{eV}$ ). It allows conduction with small inputs of energy.

Up to this point, only pure or intrinsic semiconductors have been discussed, where the sole mechanism for conduction is the transport of an electron from the valence band to the conduction band. There is, however, what is known as extrinsic semiconductors. Extrinsic semiconductors lower the bandgap energy by the introduction of impurity atoms or dopants into the semiconductor. If a donor atom is introduced (an atom with 5 valence electrons causing an excess of one electron when bonding occurs) then little energy is required to boost the extra electron to the conduction band. If an acceptor atom is introduced (an atom with 3 valence electrons causing excess holes) then little energy is required to move electrons in the valence band to the hole site. The net effect is less energy required for conduction. Therefore, a semiconductor's electrical properties can be improved by adding impurities to the

material. Figure 2-3 is a representation of what happens to the bandgap when impurities, either donor or acceptor are introduced. Note that the quantum state of the excess electron is located slightly below the conduction band while the energy level associated with a hole is located just above the valance band.

Doping a semiconductor with donor or acceptor atoms classifies the material now as either n-type or p-type. When these two types of material are placed in contact with each other, a junction forms which provides a necessary function in solar cells and will be discussed in more detail later.

#### **4. Temperature Effects**

Conductivity in intrinsic semiconductors is characterized by a very strong temperature dependence. Unlike metals which increase conductivity with decreasing temperature, a semiconductor increases conductivity with increasing temperature. The increased temperature provides thermal energy to break the bonded electron away for conduction. In metals, heat is absorbed by the atom and transformed to lattice vibration. Since the electron concentration is temperature in dependent, electron mobility tends to decrease. Semiconductor electron concentration is very temperature dependent. It is the absorption of the thermal energy which elevates the electron past the energy bandgap. Electron density increases exponentially with

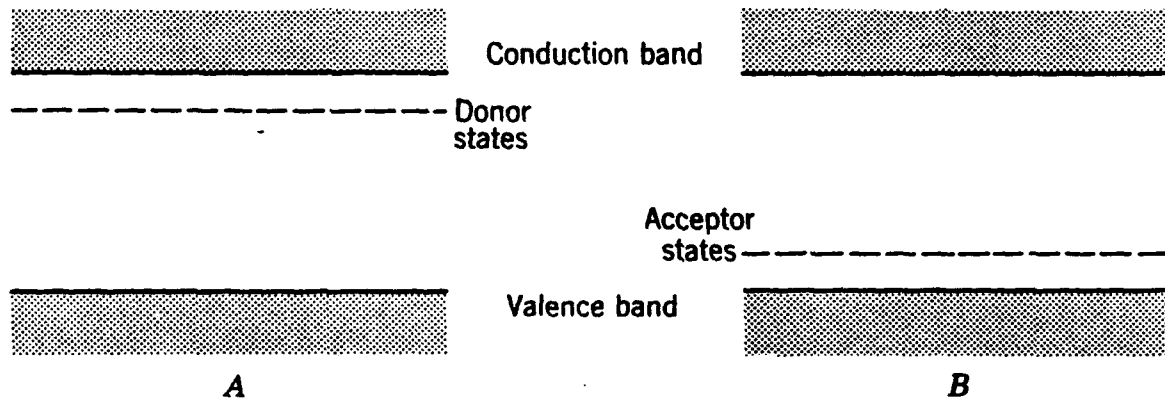


Figure 2-3. Representation of discrete, localized impurity levels in an energy-level diagram for the case of A, donor, and B, acceptor, impurities. [from Ref. 11:p. 204]

temperature and tends to overcome the lattice vibrational effects.

As impurities are added, the temperature dependence of the electron density becomes less. With heavy doping, the temperature dependence become negligible and the semiconductor acts similar to the behavior of metals. However, as will be dicussed later, the temperature effects in solar cells is quite different.

## **B. PHOTOVOLTAIC EFFECT**

### **1. Theory of Solar Cells**

When light falls incident on a semiconductor device, the photon energy is either absorbed, reflected or passed through. When absorbed, the photons collide with the atomic electrons imparting sufficient energy for the electrons to break their bonds within the atomic structure. The dislodged electron leave "holes" in the structure, and while the electrons are boosted to the conduction band, the holes are left behind in the valence band. These are normally referred to as electron-hole pairs. If nothing else happens, the electrons will eventually recombine with the holes. The net effect of the absorption process being nothing more than a heating up of the semiconductor.

The solar cell, however, introduces an internal electric field which separates and collects the electron-hole pairs before they recombine. This electric field is produced by a p-n junction formed by the contact between n-type and p-



type samples of the same material. When the contact between n-type and p-type material is made, excess electrons from the n-type region will migrate over into the p-type region near the junction and the holes from the p-type region will migrate to the n-type region. A charge field is created which sets up a barrier for further net charge movement. In other words, the barrier prevents other free charges from migrating across the junction. This barrier known as the potential barrier or depletion region, plays an important role in the generation of electricity. As light-generated electrons and holes become available, the potential barrier separates them forcing electrons from the p-region where they are called minority carriers to the n-region where they are known as majority carriers. The holes transport from the n-region to the p-region. An electron in the n-region is called a majority carrier and a hole in the n-region is called minority carrier. For the p-region, the opposite is true (holes are majority carriers and electrons are minority carriers). It is the minority carrier which must pass through the barrier. Since there are fewer carriers of opposite charge to recombine with, the minority carrier, has a high probability of reaching the respective region surface. The net result is a voltage difference between either end of the cell. The solar cell, which is a semiconductor device, will now generate current through electrical contacts to an external circuit as shown in Figure 2-4.

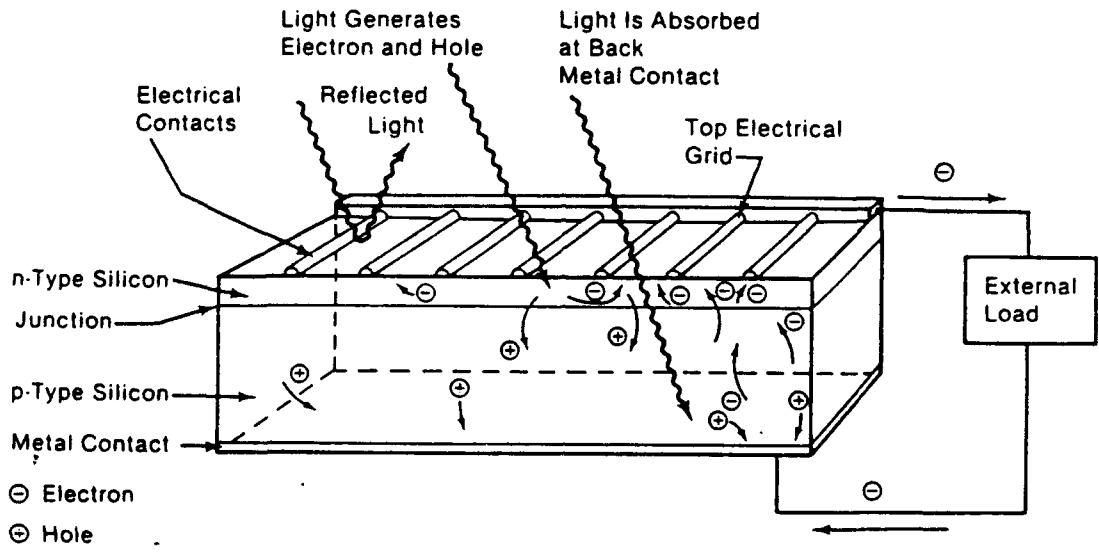


**Figure 2-4. Light incident on the cell creates electron-hole pairs, which are separated by the potential barrier, creating a voltage that drives a current through an external circuit. [from Ref. 9:p. 14]**

## 2. Efficiency

The physical phenomenon of converting light or photo energy to electricity is known as the photovoltaic effect. This process is the basis of power generation in solar cells. The energy associated with light (photons) necessary to free an electron from its atomic bonds, ranges from 0 to 2.5 eV based on the type of semiconductor used.

As photons strike the solar cell, one of a number of effects will take place. The energy can be sufficient enough to:

- produce an electron-hole pair,
- produce an electron-hole pair and generate heat in the form of atomic vibrations, or
- not produce an electron-hole pair but generate heat.

The energy can also be reflected or passed through the cell without being absorbed. Because of these events, most of the energy that strikes the cell is lost before it can be converted to electricity. The result is low conversion efficiency.

In order for a photon to be of significant use in the conversion process, it must have sufficient energy to transfer to an electron in order for the electron to breach the bandgap. It is ideal though to have energy slightly greater than the bandgap to ensure the transition of the electron from the valance band to the conduction band. Figure 2-5 shows the visible light spectrum and the associated energy. Note that the smaller the bandgap, the greater the number of electron-hole pairs generated. Too small a bandgap would result in

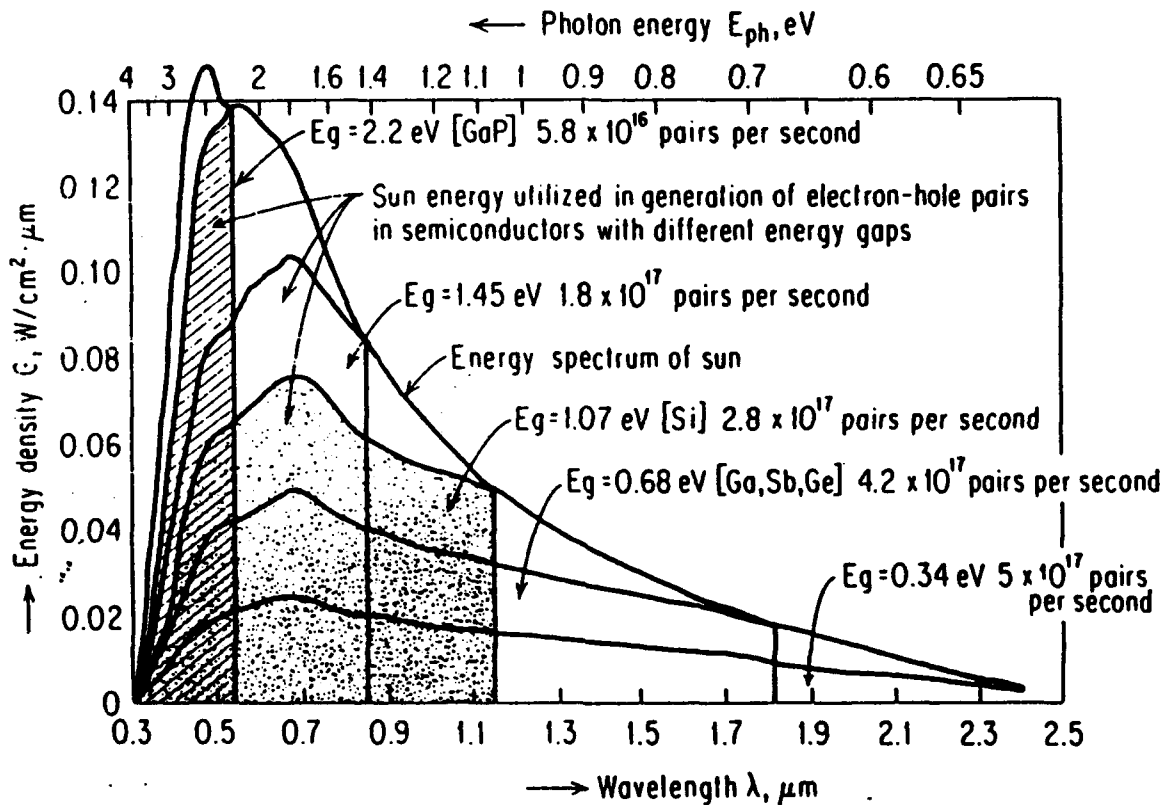


Figure 2-5. The energy spectrum of the sun on a bright, clear day at sea level (excluding water vapor absorption) and the parts of this spectrum utilizable in the generation of electron-hole pairs in semiconductors with energy gaps of 2.25, 1.45, 1.07, 0.68 and 0.34 eV, respectively. Listed for each of these cases is the number of electron-hole pairs generated, obtained under the assumption of the existence of an abrupt absorption edge with complete absorption and zero reflection on its high energy side. [from Ref. 21:p. 24-11]

photon energy being wasted as heat. It is, therefore, necessary that the material being used for photovoltaic conversion have an optical bandgap. The idea is to match the bandgap characteristic of the solar cell with the solar spectrum such that the maximum amount of energy in the sun's spectrum falls slightly above the bandgap energy of the cell for maximum efficiency. From Figure 2-6, maximum efficiency is illustrated as a function of the bandgap energy for various cells. Note where Gallium Arsenide and Indium, Phosphide fall in relation to the maximum attainable efficiency of a cell under Air Mass Zero (AMO) conditions. So, at 273°k, the desirable energy gap would be approximately 1.4 eV.

The parameters that characterize the performance of a p-n junction solar cell are:

open circuit voltage	$V_{oc}$
short circuit current	$I_{sc}$
fill factor	FF

The efficiency of a cell is the ratio of the cell's maximum output power to the power incident on the cell from radiant energy. The theoretical maximum power  $P_T$  of a cell is

$$P_T = V_{oc} I_{sc} \quad (2-1)$$

With the conversion losses mentioned above the maximum practical ( $P_m$ ) power is somewhat less than  $P_T$ . The I-V curve of Figure 2.7 shows the maximum output power ( $P_m$ ). Another solar cell parameter is the Fill Factor (FF) and is defined as:

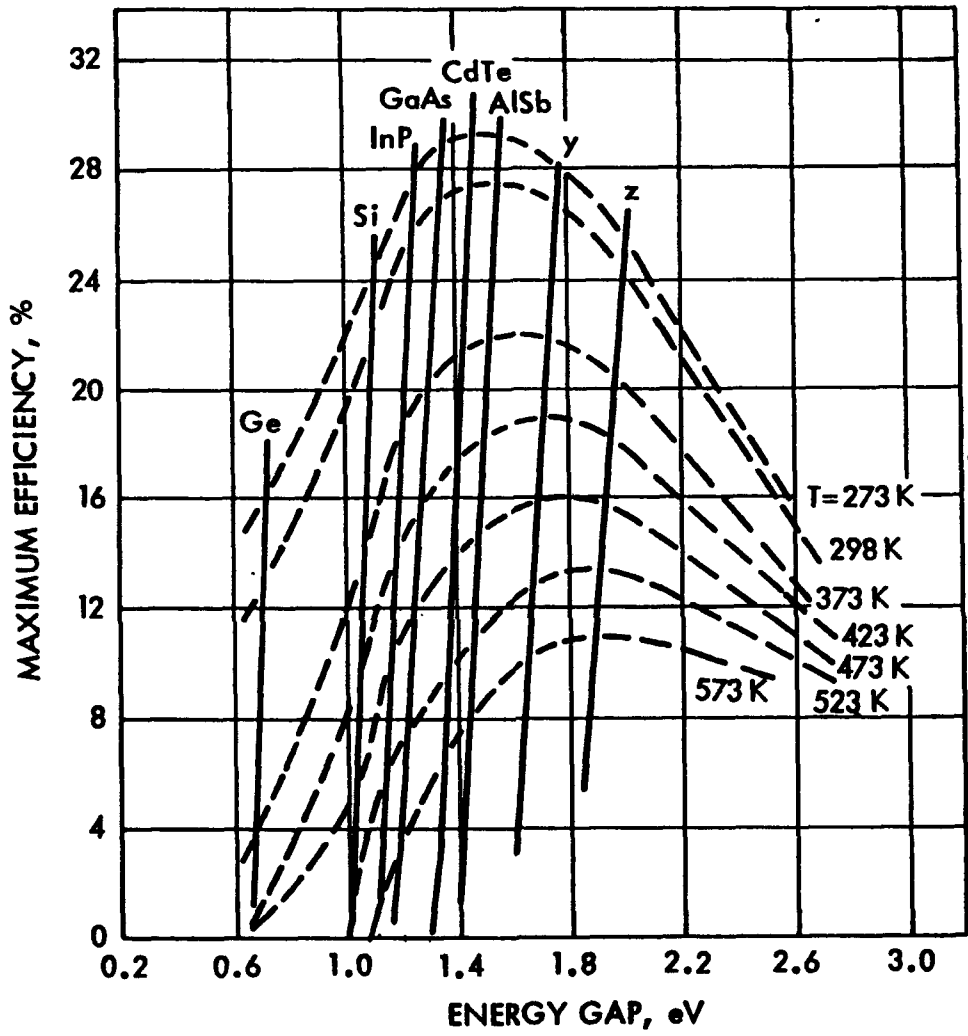


Figure 2-6. Temperature-Dependent Maximum Efficiency as a Function of Energy Gap for a Few Photovoltaic Materials [from Ref. 13:p. 1-32]

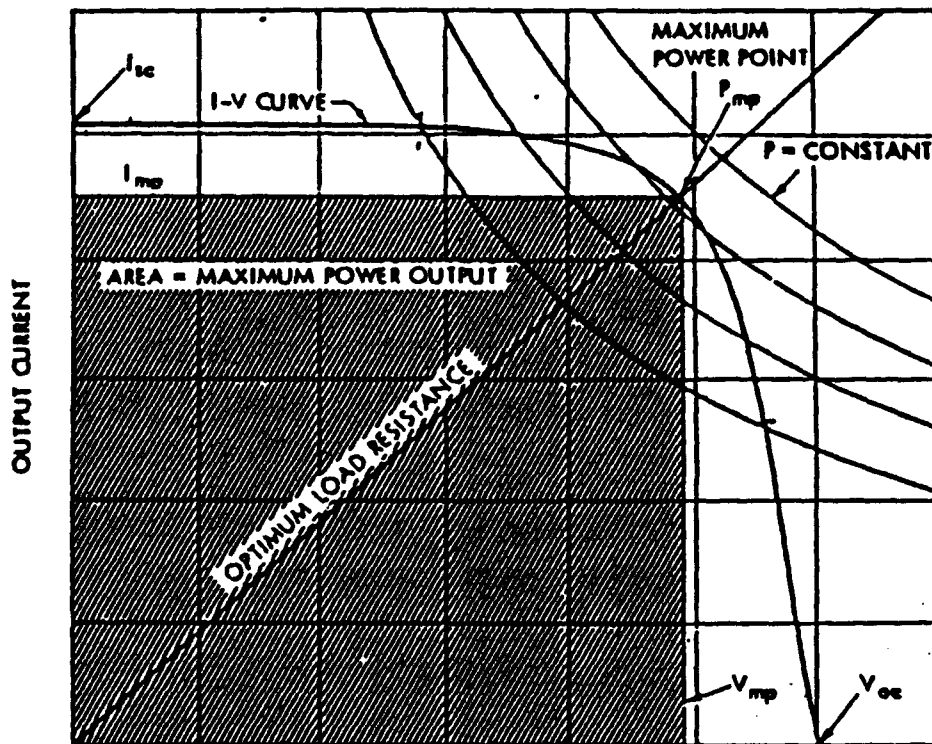


Figure 2-7. Solar cell electrical output characteristics (I-V curve) [from Ref. 31]

$$FF = \frac{P_m}{V_{oc} I_{sc}} = \frac{P_m}{P_T} \quad (2-2)$$

Under Air Mass Zero (AMO) conditions, the sunlight incident power is approximately 1.36 Kw/m<sup>2</sup>. Then the efficiency of a cell can be calculated as

$$\eta = \frac{P_m}{P_{incident}} = \frac{V_{oc} I_{sc} FF}{\text{Sunlight Incident Power}} \quad (2-3)$$

In order to achieve high conversion efficiency, the requirements are high  $V_{oc}$ ,  $I_{sc}$ , and FF (sharp corner in the I-V curve). Energy conversion efficiencies of standard solar cells range between 12 and 17 percent; the main reason being that, in the solar spectrum, 26 percent of the energy is in photons having photon energy of less than 1.1 eV (bandgap for silicon) [Ref. 7:p. 60]. From Figure 2-5, it can also be seen that approximately 40 percent of the energy is in photons having photon energy less than 1.45 eV (bandgap for GaAs). Of the remaining 60 percent (those photons with energy greater than 1.45 eV), any energy greater than the 1.45 eV required to generate an electron-hole pair is absorbed by the atomic structure and produces heat in the form of atomic vibrations. Thus, approximately 25 percent of the energy in these photons is wasted. Solar cell efficiency of 15 to 18 percent for standard GaAs is typical.

### 3. Factors Affecting Solar Cell Efficiency

The upper limits of solar cell efficiency are bound by several factors. Radiant energy passing through the cell, as



well as reflection, produce no effect in the photovoltaic conversion process. And, because sunlight is not monochromatic, much of the radiant energy absorbed produces heat. The remaining energy causes the electron-hole pairs to generate current. The factors affecting the production of electron-hole pairs to generate current are discussed. Although some of the factors are inherent to the cell, improvement is achieved through good design and material selection.

**a. Bandgap Energy**

As noted earlier, the smaller the bandgap of the cell, the greater the number of available photons there are with enough energy to create electron-hole pairs. However, should the bandgap be too small, most of the radiant energy would be wasted as heat. The most desirable range for the bandgap would be the range that matched the peak of the solar spectrum. This range would be between 1 and 2.5 eV as shown in Figure 2.5. Silicon's bandgap energy is 1.1 eV while GaAs and InP are 1.42 and 1.35 eV respectively. Note from Figure 2-6 that Gallium Arsenide's bandgap almost coincides with the peak efficiency associated with the solar spectrum.

**b. Temperature**

Figure 2-6 shows that the solar cell efficiency decreases with increasing temperature, despite the fact that conductivity in semiconductors characteristically increases

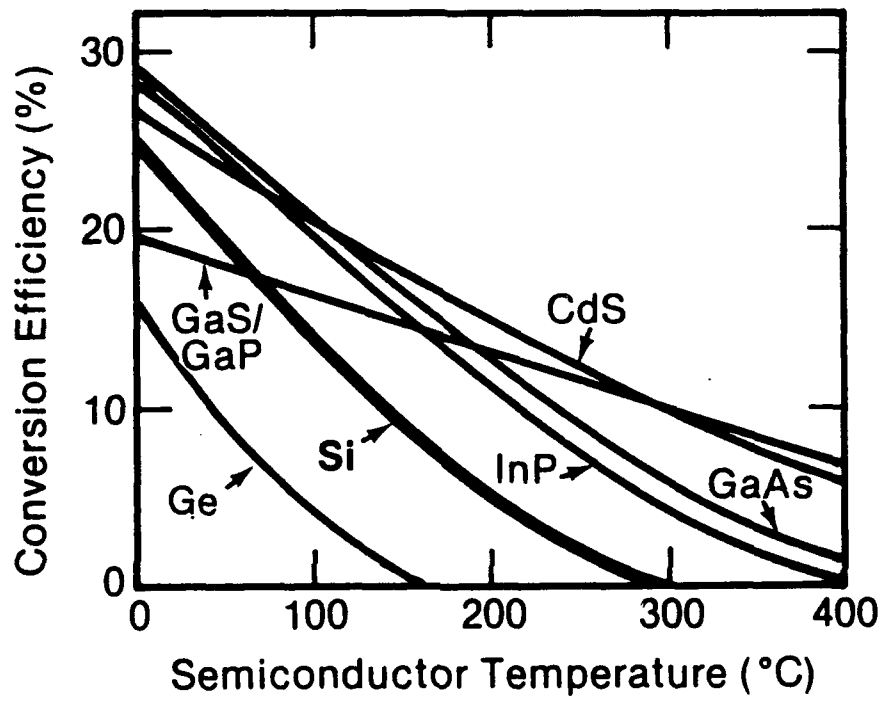


Figure 2-7. Solar cell efficiency versus temperature for various materials: Note that all materials lose efficiency in the range shown. [from Ref. 9:p. 21]

with increasing temperature (Figure 2-7). Two predominant factors cause efficiency to drop as temperature rises (as thermal energy increases): 1) lattice vibrations interfere with the free passage of charge carriers, and 2) the junction begins to lose its power to separate charges [Ref. 8:p. 17]. The first factor degrades performance even at room temperature. It is the second factor which occurs at higher temperatures, that leads to the erosion of the photovoltaic effect. At higher temperatures, a great many electrons are broken from their bonds. These electrons outnumber the free electrons supplied by dopants. Also created are the holes, formed by the thermally-freed electrons. The n-type material begins to lose its n-type characteristic. The same process occurs on the p-type side which loses its p-type characteristic. The effect is 1) the thermally agitated charge carriers have so much energy, that they cross over the p-n junction in both directions as if the barrier field were not there, and 2) ultimately, the junction itself disappears because there are no longer n- and p-type sides to create the barrier [Ref. 9:p. 22-22]. Thus, the efficiency diminishes.

It can be shown that temperature dependence can be reduced by larger bandgaps. Thus, GaAs cells are only about half as sensitive to increasing temperature as silicon cells [Ref. 10:p. 92].

### **c. Recombination**

The inadvertent random encounter of light-generated electron-hole pairs can lead to their rejoining or recombination before they contribute to current generation. Recombination occurs by either direct or indirect methods. Direct recombination occurs when an electron and a hole randomly encounter each other. The electron rebonds with the atom by falling back into a hole. The electron's energy is lost as heat. This process occurs mostly before the electron has a chance to cross the potential barrier. Once across, direct recombination is rare.

Indirect recombination occurs when an electron-hole recombination is influenced by other factors such as empty, or dangling bonds from impurities or defects which capture the free electrons. This mechanism is more prevalent.

Recombination can also occur when a free charge carrier has a collision, reducing its energy and increasing the probability that it will fall into a bond.

### **C. CARRIER TRANSPORT**

There are two major mechanisms by which current flow in a semiconductor occurs: drift and diffusion of charge carriers. Drift of charge carriers is caused by the movement of free electrons and holes in the presence of an electric field. The charge carriers are accelerated by the electric field and acquire a velocity component in addition to their velocity

associated with their thermal energy. This velocity can be expressed in relation to the field strength by:

$$v_n = \text{electron drift velocity} = \mu_n E \quad (2.4)$$

$$v_p = \text{hole drift velocity} = \mu_p E \quad (2.5)$$

where  $E$  is the electric field strength and  $\mu$  is the charge carrier's mobility constant. Since the movement of charge causes current flow, drift current in the semiconductor can be expressed as

$$J_{\text{Drift}} = -qn v_n + qp v_p = q(n\mu_n + p\mu_p)E = \sigma E \quad (2.6)$$

where  $J_{\text{Drift}}$  is the current density (current flow per unit area) and  $\sigma$  is the semiconductor conductivity constant. Table 2-1 gives electrical properties of some semiconductors.

The more significant mechanism of current flow is that associated with diffusion. This is the process whereby random movement of the particles exist due to concentration gradients. In other words, the free charge carriers will diffuse from a region of high concentration to a region of low concentration which gives rise to a net flow of charge or diffusion current. Diffusion current flow can be expressed as:

$$J_{\text{diffusion,holes}} = q D_p \frac{dp}{dx} \quad (2.7)$$

$$J_{\text{diffusion,electrons}} = q D_n \frac{dn}{dx} \quad (2.8)$$

where

$J_{\text{diffusion}}$  = diffusion current density (for holes or electrons)

$D_p$  = diffusion constant for holes

$D_n$  = diffusion constant for electrons

$\frac{dp}{dx}$  = gradient of hole concentration

$\frac{dn}{dx}$  = gradient of electron concentration

TABLE 2-1  
ELECTRICAL PROPERTIES OF SEVERAL IMPORTANT  
SEMICONDUCTOR MATERIALS AT 300 K  
[from Ref. 10:p. 42]

Material	$n_i$ (cm <sup>-3</sup> )	Mobility (cm <sup>2</sup> /V·s)		$\rho$ ( $\Omega$ -cm)	$\sigma$ (S·cm <sup>-1</sup> )	Diffusion Constant (cm <sup>2</sup> /s)	
		$\mu_n$	$\mu_p$			$D_n$	$D_p$
Si	$1.4 \times 10^{10}$	1300	500	$2.5 \times 10^3$	$4.4 \times 10^{-6}$	34	13
Ge	$2.5 \times 10^{13}$	3800	1800	43	$2.2 \times 10^{-2}$	98	46
GaAs	$9 \times 10^6$	8500	400	$4 \times 10^9$	$1.3 \times 10^{-9}$	220	10

The diffusion constant (D) is significant because it relates the mean distance that a minority carrier travels before recombination, or diffusion length (L), and the mean time of recombination (T), or minority carrier lifetime by the expression

$$L^2 = DT \quad (2.9)$$

The concept of diffusion length is used to describe the theory of operation of semiconductors and to calculate the effect of radiation. As will be discussed later, the effects of radiation on solar cell performance is due to the change in minority carrier lifetime which decreases the diffusion length.

#### D. P-N JUNCTION

A p-n junction is, for our purposes, considered to be one semiconductor (Si, GaAs, InP) with two regions of different conductivity type; n-type and p-type. The junction forms at the region where the conductivity changes from one type to the other. In the immediate neighborhood of the junction a depletion layer is formed which, by virtue of charges moving across the junction, sets up an electric field or potential barrier. This barrier, as described earlier, opposes the further flow of free charge carriers. As more carriers cross the junction, the potential barrier increases until the opposition allows no more charge carriers across. Thus, a semi-permanent electric field is established in the region of the junction as shown (Figure 2-8). The magnitude of the potential barrier depends upon the width of the forbidden-energy gap, the impurity concentration of dopant, and the temperature [Ref. 11:p. 270].

The quality of the potential barrier is that it opposes the crossing of majority charge carriers but minority carriers are not hindered from crossing. Minority carriers are in fact driven by the field to the opposite side of the junction. So, when a light-generated electron-hole pair is formed, the electron is driven to the n-type side and the hole is driven to the p-type side. Once the electrons are on the n-type side and the holes are on the p-type side, they can move around without being prevented by the recombination process from

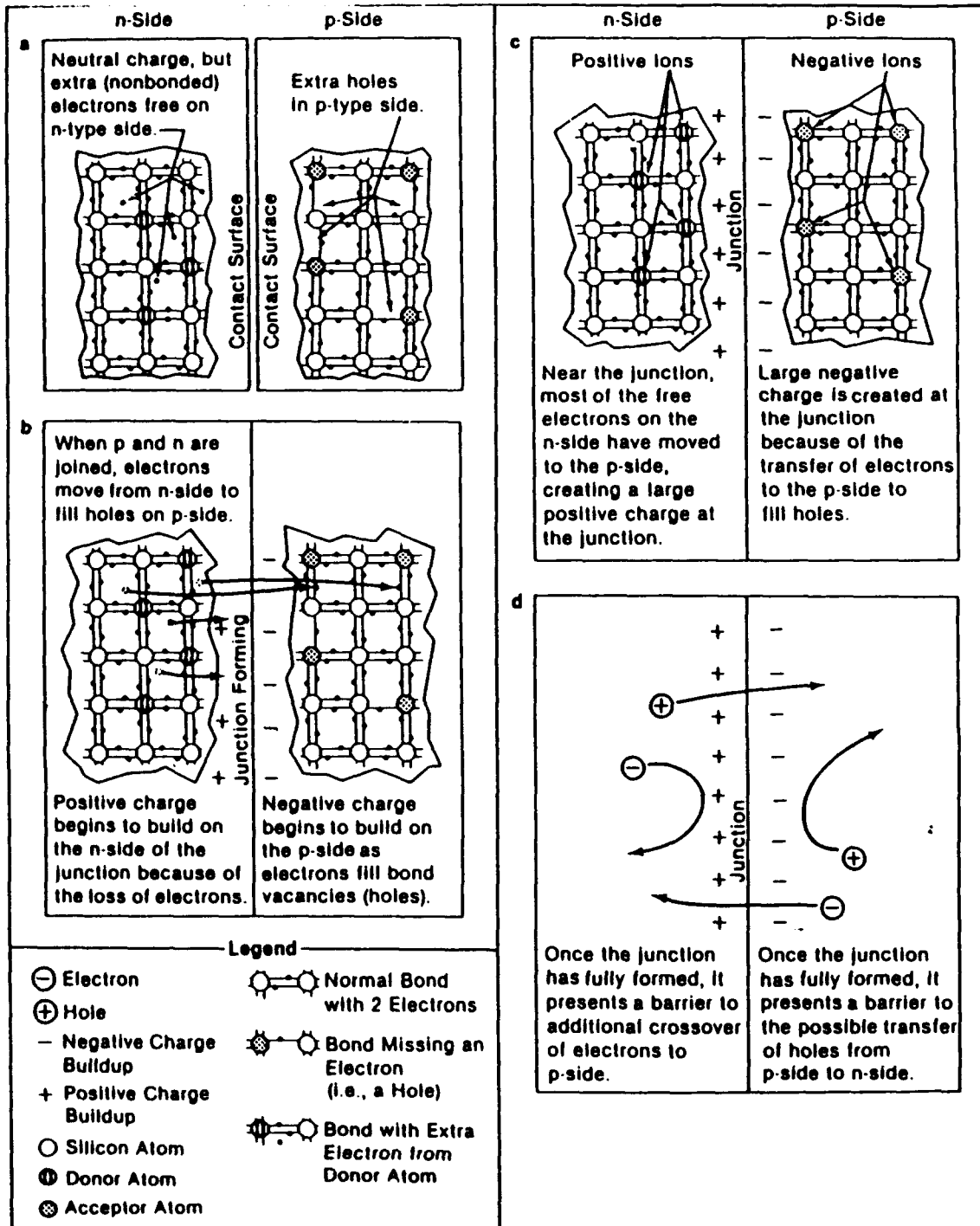


Figure 2-8. During junction formation, electrons move from the n-type silicon into the p-type, white holes move in the opposite direction. Movement of electrons into the p-type silicon and holes into the n-type silicon builds a fixed potential barrier at the junction, opposing further movement and creating a state of equilibrium. [from Ref. 8:p. 12]



reaching the surface contacts of the cell. Since a charge imbalance now exists in the cell, current can flow through a connected external circuit.

#### E. P-N JUNCTION CAPACITANCE

The p-n junction is a double layer of oppositely charge carriers separated by a small distance (the depletion region) and thus has the properties similar to a parallel plate capacitor. It, therefore, has associated capacitance. The capacitance  $C$  of the junction is given by

$$C = \frac{A \epsilon}{W} \quad (2.10)$$

where  $A$  is the area of the junction in the solar cell,  $\epsilon$  is the permittivity of the cell ( $\epsilon = K\epsilon_0$ , where  $K$  is the dielectric constant of the cell) and  $W$  is the width of the depletion region.

The acceptor or donor density in the p-type or n-type region adjacent to the depletion region can be related to the capacitance per unit area by

$$\frac{C}{A} = \left[ \frac{q\epsilon N}{2(V_b - V_a)} \right]^{1/2} \quad (2.11)$$

or

$$N = \frac{2(V_b - V_a) C^2}{qEA^2} \quad (2.12)$$

where  $N$  is the smaller value of acceptor density  $N_A$  or donor density  $N_D$ , and  $V_a$  is the applied voltage (positive in forward

bias), and  $V_b$  is barrier voltage. Using  $N_n$  assumes heavily doped n-region while  $N_p$  assumes heavily doped p-region.

Equation (2.11) illustrates that the capacitance varies with the applied voltage. Therefore, measuring  $C$  as a function of reverse bias to a solar cell and plotting  $1/C^2$  versus  $V_b$  will allow  $N$ , the doping density on the lightly doped side of the cell to be found [Ref. 10:p. 68]. These expressions assume an abrupt junction which is characteristic of conventional solar cells.

### III. SOLAR CELL RADIATION DAMAGE

#### A. SPACE ENVIRONMENT

Throughout its lifetime, a spacecraft in orbit is continually exposed to high-energy radiation. The earth's orbital environment is characterized by the magnetosphere which is created through the interaction of the solar wind and the terrestrial magnetic field as shown in Figure 3-1. Earth's radiation zone, referred to as the Van Allen Belts, consists of magnetically-trapped electrons and protons, providing the hostile environment responsible for the degradation of solar cell efficiency.

Figures 3-2 and 3-3 illustrate the distribution of the trapped protons and electrons for both the inner and outer belts. The inner belt, sometimes referred to as the hard belt, contains high energy protons of energies to 700 MeV with electron energies in the 20 keV to 1 MeV range. The outer belt called the soft belt, consists primarily of electrons from 20 keV to 5 MeV and some protons over 60 MeV [Ref. 12:p. 2.5-2].

In lower earth orbits, both geomagnetically trapped electrons and protons play significant roles in cell damage. At higher altitudes (near geosynchronous orbit) the high energy trapped electrons are the primary cause of damage except during periods of high solar activity. During these

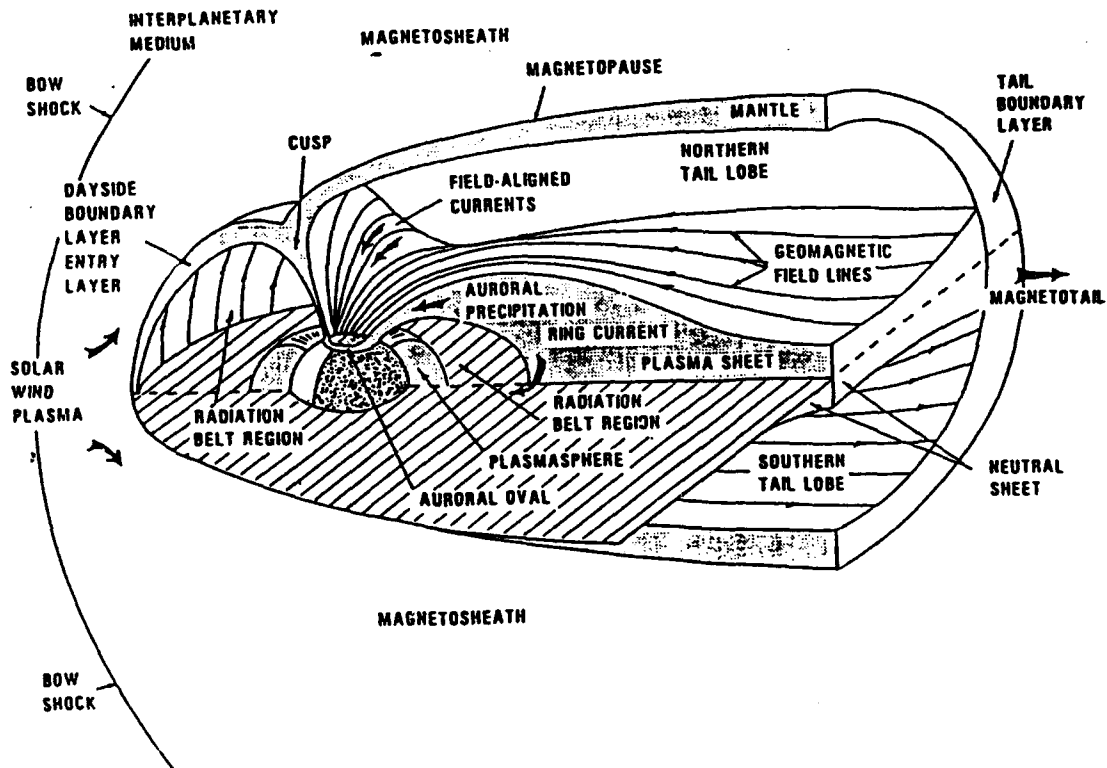
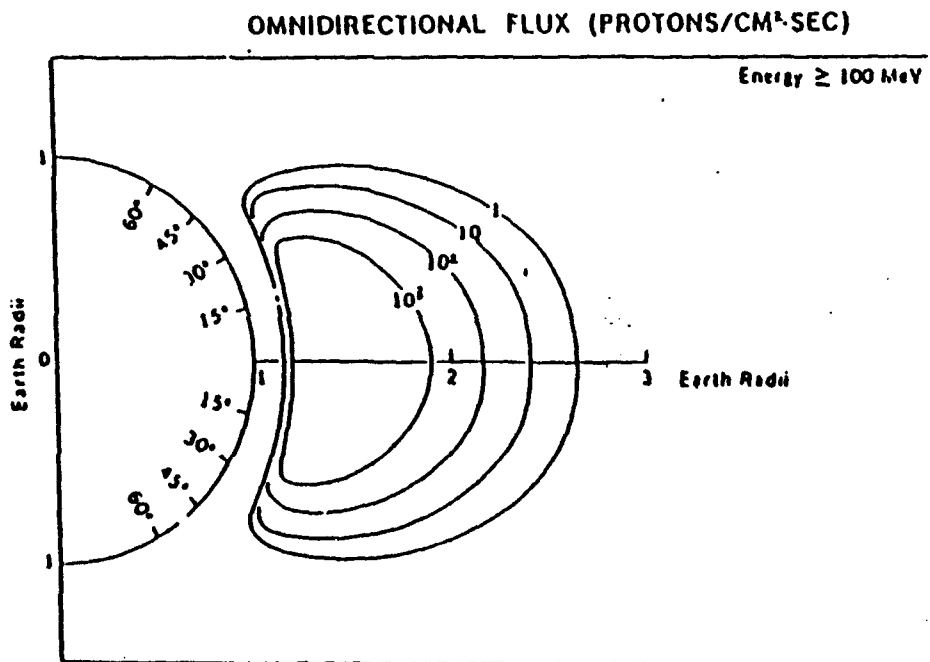
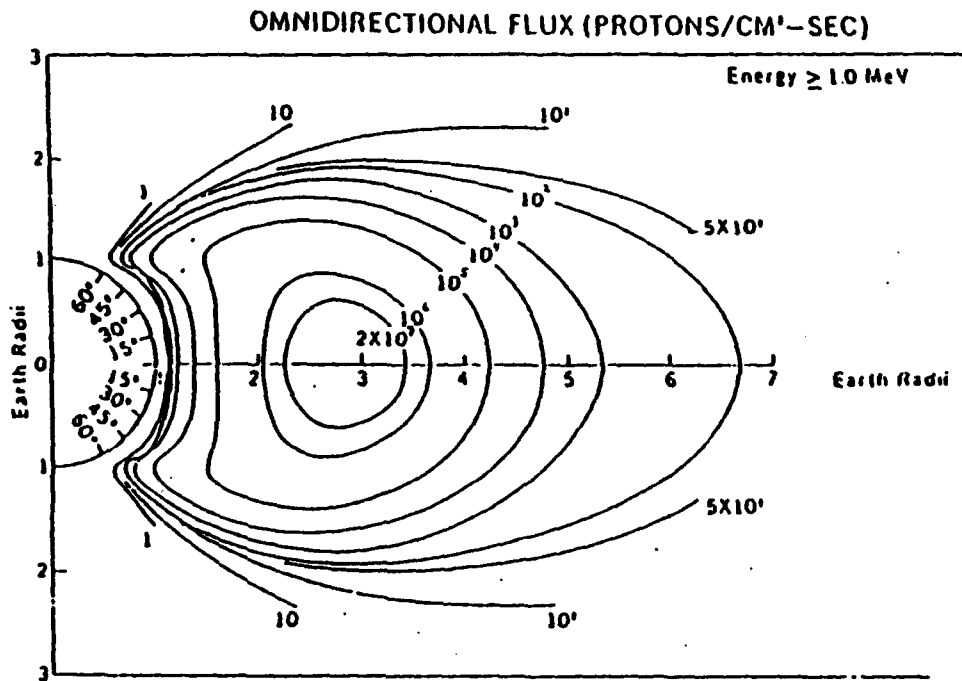


Figure 3-1. Cross section of the magnetosphere  
[from Ref. 26:p. 46]



**Figure 3-2. Distribution of trapped protons**  
 [from Ref. 26:p. 42]

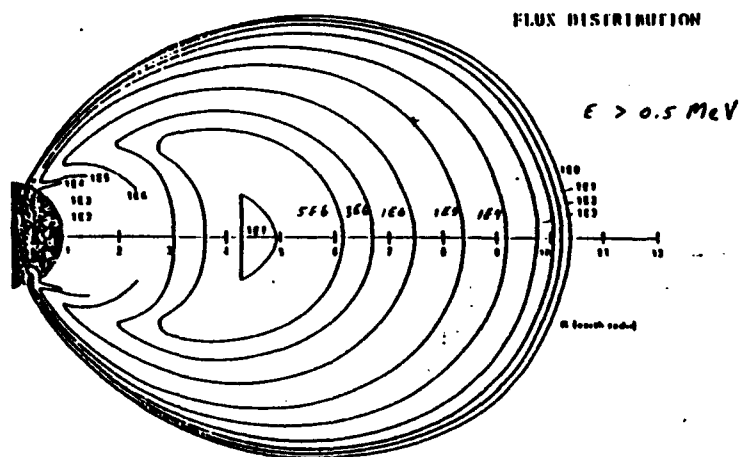
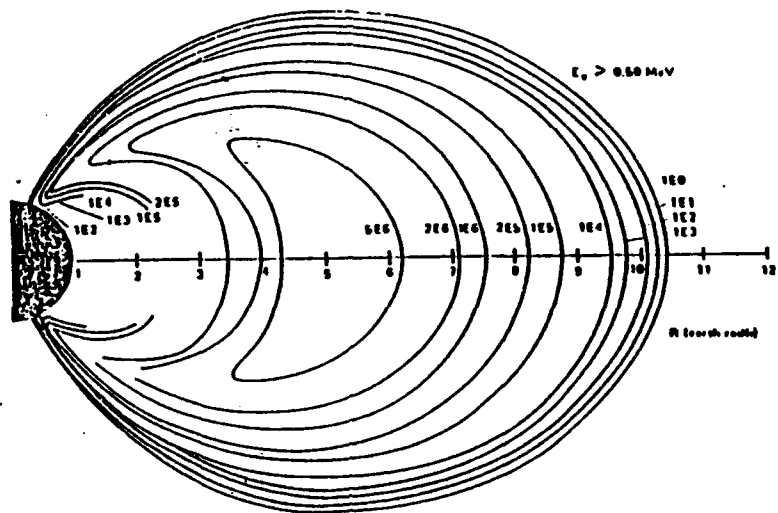


Figure 3-3. Distribution of trapped electrons  
[from Ref. 26:p. 41]

periods, solar flare protons may then add significantly to the total cell-damaging effect. To a great extent then, trapped electrons are the principle cause of solar cell degradation which is a continuing process within the space environment.

## B. THEORY OF RADIATION DAMAGE

The performance of solar cells is subject to radiation effects consisting of high energy or fast massive particles. The radiation effects are produced by electrons, protons, neutrons, or ions. Because these particles have mass, energy and sometimes charge, these particles or other particles generated by them can interact in several ways with solar cells [Ref. 13:p. 3-1]. The dominant interactions are:

- Inelastic Collisions with Atomic Electrons. An energetic charged particle (electron, proton) loses its kinetic energy to a bound atomic electron through an inelastic collision. The atomic electron experiences a transition to an excited state (excitation) or an unbound state (ionization). This is the predominant mechanism by which the energetic charged particle loses its kinetic energy.
- Elastic Collision with Atomic Nuclei. An atom can be displaced from its lattice site by the coulombic interactions of energetic charged particles and the positive charge of the atomic nucleus (Rutherford Scattering). The displaced atom may in turn collide with other atoms causing them to displace if sufficient energy was transferred to the initial displaced atom.
- Inelastic Collisions with Atomic Nuclei. The inelastic collision of highly energetic protons with the atomic nucleus causes the nucleus to be left in an excited state. Once excited, the nucleus emits energetic nucleons causing it to recoil through the lattice structure displacing itself. The recoiling nucleus in turn collides with other nuclei causing their displacement. [Ref. 13:p. 3-1]

Each interaction causes cell damage to occur. The damage phenomena can be categorized by two major types of radiation damage: ionization and atomic displacement.

Ionization occurs mainly in the solar cell cover glass. There is a reduction of transmittance of the cover glass due to its darkening. When ionizing radiation excites an orbital electron to the conduction band, the electron may become trapped by impurity atoms in the glass forming color centers. The subsequent result is a darkening of the cell cover glass reducing the illumination of the cell. Ionizing radiation will also excite the electrons in the cell from the valance band to the conduction band creating electron-hole pairs similar to the photovoltaic process. This is the beneficial effect of ionization. However, much greater energy is required from the ionization radiation than the photon to create the same number of charge pairs. The interaction with the ionization radiation and the atomic electron is inelastic, therefore, the electron experiences a transition to an excited state. If the energy transfer between the two is not sufficient to move the electron to the conduction band, the effect will be temporary. The electron will eventually recombine with a hole losing its energy to heat. The net effect would be an increase in temperature.

High energetic, fast moving particles are capable of causing atomic displacements within the crystal lattice structure of solar cells. These displaced atoms and their



associated vacancies will eventually form permanent stable defects within the crystal lattice. These defects produce the significant changes within the cell which affect the equilibrium carrier concentrations and the minority carrier lifetime and subsequently cell efficiency.

The displacement energy required to eject an atom from its lattice site is on the order of 13 eV for silicon [Ref. 13:p. 3-7] and 25 eV for GaAs [Ref. 14:p. 153]. Because the displacement of an atom involves the formation of a vacancy, the formation of an interstitial atom and other electronic and vibrational losses, the displacement energy can be expected to be much higher than the energy of formation of a vacancy [Ref. 13:p. 3-7].

### **C. LATTICE STRUCTURE DAMAGE**

Considerable lattice damage takes place as radiative particles strike a solar cell. This damage is usually in the form of crystal defects (vacancies, interstitials, vacancy-impurity complexes, defect clusters). The creation of these defects in the crystal lattice introduces additional energy states which are found in the band gap [Ref. 15:p. 157]. The defects then can act as additional recombination centers causing a reduction in minority carrier lifetime and diffusion length or they can act as additional impurities changing the net impurity concentration of the cell. In either case, the damage results in a deterioration on the cell's performance over time.

The direct result of electron displacement damage, which is of primary interest to this research, is the creation of vacancies and interstitials. Once an interaction occurs, the radiative particle may have sufficient energy to produce secondary displacements within the crystal. Therefore, the distribution of vacancies will not be uniform because the vacancies from secondary displacements will be relatively close to the associated primary vacancy [Ref. 13:p. 3-9]. The interstitials on the other hand will move randomly throughout the crystal until it loses its energy and comes to rest in the interstices of the atom. It, therefore, seems reasonable that the interstitials will have a more uniform distribution within the crystal.

Vacancies and Interstitials are extremely mobile and unstable at room temperature. Displacement damage then is caused by the various combinations available to a vacancy within the crystal. A vacancy can combine with another atom such as impurity atoms forming close coupled vacancy-oxygen pairs, vacancy donor pairs, or vacancy-acceptor pairs. In the case of vacancy-oxygen and vacancy-donor pairs, the defects are electrically active and can become negatively charged by accepting an electron from the conduction band. The energy levels of these defects are slightly below the conduction band, For vacancy-acceptor pairs, the defects can become positively charged by accepting a hole from the valance band

(giving up an electron to the valance band). The energy level of this defect is slightly above the valance band.

If a vacancy combines with an interstitial, the damage is basically eliminated. The combination returns the crystal to its original lattice structure formation. This would be the ideal condition for irradiated cells.

A divacancy defect will occur when two vacancies come together to form a stable complex. These type defects increase rapidly with increasing electron energy and appear to be of greater significance in the deteriorating performance of the cell [Ref. 13:p. 3-11]. The energy level associated with this type defect is most likely slightly above the valance band based on p-type silicon [Ref. 13:p-3-11].

The major affect that these defects have is the formation of additional recombination centers which affect the lifetime and diffusion lengths in the cell.

## IV. THEORY OF ANNEALING

### A. RADIATION EFFECTS

The performance of solar cells is represented in terms of engineering output parameters. The effect of radiation on the cells can then be described in terms of changes in these performance parameters. These parameters deal with both the physical and electrical characteristics of the cell and give insight into the mechanisms involved. Impurity concentrations, recombination, diffusion lengths and minority carrier lifetimes are the physical aspects of cell behavior while the electrical parameters include short circuit current ( $I_{sc}$ ), open circuit voltage ( $V_{oc}$ ) and power output (P).

The principal effect of radiation is the lattice defect damage caused. The displacement defects create additional recombination centers causing a reduction in minority carrier diffusion length (minority carrier lifetime). Since minority carrier lifetimes are inversely proportional to the recombination rates, the inverse lifetime is as follows [Ref. 1:p-3-16]:

$$\frac{1}{\tau} = \frac{1}{\tau_0} + \frac{1}{\tau_e} + \frac{1}{\tau_p} \quad (4.1)$$

where

- $\tau$  = minority carrier lifetime
- $\tau_0$  = minority carrier lifetime before irradiation
- $\tau_e$  = minority carrier lifetime due to electron irradiation
- $\tau_p$  = minority carrier lifetime due to proton irradiation

Because the minority carrier diffusion length (L) can be expressed as

$$L^2 = DT \quad (4.2)$$

where D is the diffusion constant, it can be shown that

$$\frac{1}{L^2} = \frac{1}{L_0^2} + K_1 \phi \quad (4.3)$$

where

- L = final minority carrier diffusion length
- L<sub>0</sub> = initial minority carrier diffusion length
- φ = particle fluence (irradiation fluence)
- K<sub>1</sub> = damage coefficient (diffusion length coefficient)

The diffusion length can be measured experimentally. It is a measure of the amount of displacement damage in the base of the solar cell [Ref. 13:p. 3-18]. Limitations do exist. Low energy protons do considerable displacement damage within the junction depletion region without changing the cell's diffusion length but seriously reducing solar cell I<sub>sc</sub> and V<sub>oc</sub>. In addition, the relationship between diffusion length and I<sub>sc</sub> and V<sub>oc</sub> are not well defined, and diffusion length is more difficult to measure than I<sub>sc</sub> or V<sub>oc</sub>. Therefore, to better evaluate the mechanism, radiation effects are expressed in terms of the electrical parameters rather than the physical ones.

Radiation will cause significant degradation in base resistivity, short circuit current (I<sub>sc</sub>), open circuit voltage (V<sub>oc</sub>) and subsequently the maximum power point (P<sub>max</sub>). The effects of radiation on I<sub>sc</sub> and V<sub>oc</sub> can be determined by

$$I_{sc} = I_{sc}(0) - C \log \left( 1 + \frac{\phi}{\phi_x} \right) \quad (4.4)$$

and

$$V_{oc} = V_{oc}(0) - K \log \left( 1 + \frac{\phi}{\phi_x} \right) \quad (4.5)$$

where

- $\phi$  = irradiation fluence
- $\phi_x$  = irradiation fluence at which  $I_{sc}$  (or  $V_{oc}$ ) starts to change to a linear function of the logarithm of the fluence
- $C, K$  = constants which represent the decrease in  $I_{sc}$  ( $V_{oc}$ ) per decade in radiation fluence in the logarithmic region

The degradation in  $I_{sc}$  and  $V_{oc}$  will result in a decreased I-V curve as shown in Figure 4-1. The maximum power ( $P_{max}$ ) is found using equation

$$P_{max} = (FF) I_{sc} V_{oc} \quad (4.6)$$

where

FF = fill factor

Since the fill factor is relatively unaffected by electron radiation, then Eqs. 4.4 and 4.5 can be substituted into Eq. (4.6) to give the expression

$$P_{max} = P_{max}(0) - H \log \left( 1 + \frac{\phi}{\phi_x} \right) \quad (4.7)$$

which closely describes the radiation effects on power.

It has been observed and reported that a relationship exists between  $I_{sc}$  and the diffusion length [Ref. 13:p. 3-18]. This relationship is expressed as

$$I_{sc} = A + B \ln L \quad (4.8)$$

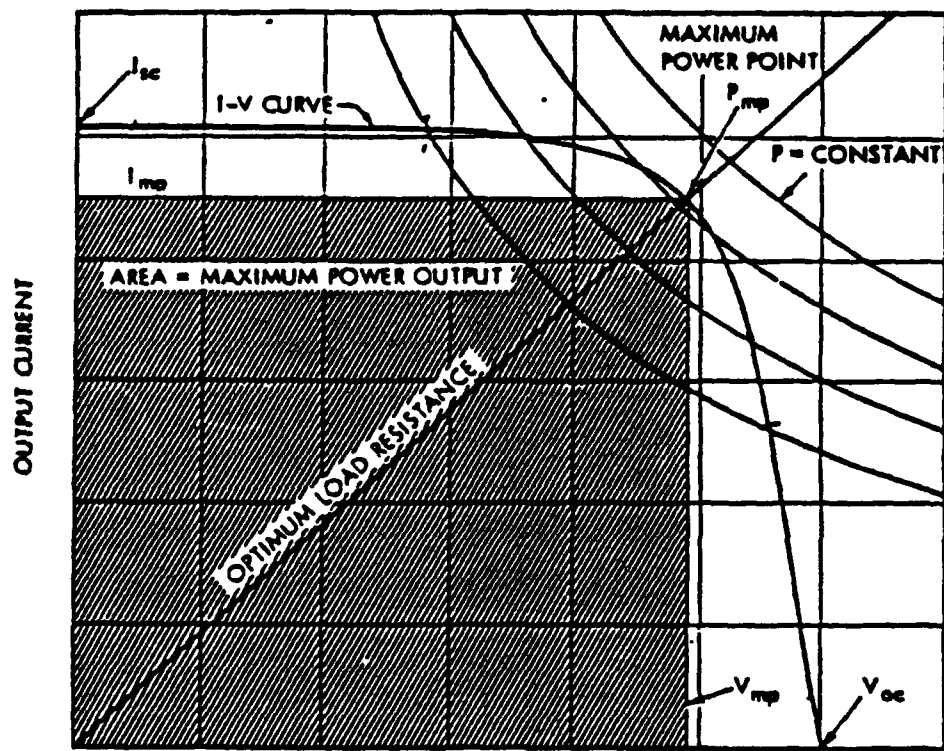


Figure 4-1. Solar cell electrical output characteristics (I-V curve) [from Ref. 31]

The constants A and B are dependent on the spectral content and intensity of the light source used to measure  $I_{sc}$ . Using Eq. 4.3 and substituting into Eq. 4.8, gives

$$I_{sc} = A - \frac{B}{2} \ln \left( K_1 \phi + \frac{1}{L_0^2} \right) \quad (4.9)$$

which is in the same form as Eq. 4.4.

#### **B. RADIATION DEFECTS IN SOLAR CELLS -- DAMAGE EQUIVALENCE**

The energies associated with electrons and protons within the space environment vary over a wide range. In order to evaluate the effects of radiation damage in solar cells, it is necessary to describe the various types of radiation in terms of an environment that can be reproduced under laboratory conditions. The concept of damage equivalence is, therefore, based on the 1 MeV electron fluence for solar cell degradation. The damage produced in solar cells by electrons of various energies is related to the damage produced, under laboratory conditions, by 1 MeV electron by the damage coefficients  $\phi_c$  (critical fluence) and  $K_1$  diffusion length damage coefficient). Similarly, the damage produced by protons of various energies is related to the damage of 10 MeV protons which induce the same amount of damage as 1 MeV electrons at 3000 times the fluence of the 10 MeV protons [Ref. 16:p. 335]. Thus, it is now possible to construct a model in which the various components of a combined radiation



environment can be described in terms of a damage equivalent fluence of a selected monoenergetic particle [Ref. 13:p. 3-24].

### C. SOLAR CELL ANNEALING

The crystalline damage and associated electrical degradation of radiation-damaged solar cells can, to some extent, be reversed. This is done by thermal and/or electrical defect annealing -- a process by which heat and/or current is introduced to the cell causing the energy level of the cell to increase. The recovery is due to atomic movement within the crystal causing the lattice structure to return to its original condition. Although the crystal is not 100% restored, the annealing process achieves sufficient recovery to extend the life of the cell's usefulness. This is accomplished via the processes: 1) a recombination of crystal vacancies and interstitials are effected creating less atomic dislocations and 2) the rearranging of dislocations to a more stable configuration without a change in the number of dislocations present. Both processes provide a more stable crystal with a partial elimination of the radiation induced lattice defects and a decrease in additional recombination centers within the energy band gap.

Increasing the base temperature of the solar cell through the addition of heat is known as thermal annealing. It is the most common method of defect annealing. The energy level increase is a function of annealing temperature. Research

conducted by Loo, et al [Ref. 17], shows that periodic thermal annealing at temperatures as low as 200°C considerably reduces the radiation damage to GaAs cells.

The use of minority carrier injection annealing (forward-bias current annealing) has provided another method for cell damage recovery. Here, a forward-biased potential is created across the cell forcing current through. The forward current increases exponentially as the potential increases [Ref. 1:p. 49]. The effect is an increase in cell temperature and minority carrier concentrations [Ref. 14:p. 36]. The premise is that the increase in minority carriers will attach to the additional recombination centers forming a more stable crystal. It was shown that annealing took place at near room temperature with minority carrier injection [Ref. 18:p. 1106].

Lang [Ref. 18] discovered an accelerated annealing rate of defect states when a forward bias was applied in GaAs at a temperature of 100°C. Thus, a combination of thermal and electrical annealing appears to provide an optimizing process for damage recovery.

#### **D. PREVIOUS ANNEALING RESEARCH**

Clark and Staats [Refs. 1 and 3] concluded that GaAs solar cells can be annealed successfully after a one-time irradiation. Recovery was a function of a combination of thermal and electrical annealing mechanisms. Results showed that 28-30% recovery of lost power was achieved after annealing at 90°C with 0.5 A/cm<sup>2</sup> of continuous current for 48

hours. Annealing past 48 hours provided no additional recovery. With the temperature constant at 90°C, and a forward-biased current of 1.0 A/cm<sup>2</sup>, cell degradation occurred after 48 hours. The optimum parameter, therefore, seemed to be 90°C with 0.5 A/cm<sup>2</sup> for 48 hours.

Cypranowski [Ref. 2] expanded the research by pioneering into the area of repetitive irradiating and annealing cycles for GaAs and InP solar cells. This time, concurrent forward-bias current and heat annealing of InP and GaAs cells was investigated. Also, optimum parameters were explored for InP. Results indicated that the optimum fluence for irradiating GaAs solar cells is in the range of 1E14 to 1E15 electrons/cm<sup>2</sup>, and the best recovery occurred with heat and forward-biased current annealing for 48 hours. For InP, the majority of the recovery process took place within two hours of annealing. It was also observed that InP cells were able to withstand higher fluence levels of irradiation and recovered a greater percentage of their power and efficiency than GaAs.

This thesis intends to verify Cypranowski's work and simultaneously delve into the mechanisms behind the deformation and recovery process through Deep Level Transient Spectroscopy.

## V. DEEP-LEVEL TRANSIENT SPECTROSCOPY

### A. DEEP-LEVEL TRANSIENT SPECTROSCOPY THEORY

Since lattice structure damage is known to take place as radiative particles strike a solar cell, it is desirable to understand the characteristics of the defects that occur. These effects have significant impact on the cell's performance by creating additional recombination centers, or traps, within the bandgap of the semiconductor material. These traps in turn cause a reduction in minority carrier lifetime and diffusion length which, in the course of time, deteriorate the photovoltaic conversion process. Investigation into the energy levels of the traps (called deep-levels), their concentration, and the effect of annealing, will provide a clearer understanding into the mechanisms of solar cell damage and insight into reversing the deteriorating effects.

In studying deep-levels, information concerning energy, density and capture cross-section of recombination centers within the bandgap, can be readily obtained. It is also possible to determine the spatial distribution of defects within the crystal structure and distinguish between minority and majority traps -- all which allow us to characterize the effect of the defect on semiconductor operation and performance.

Defect characterization and identification is accomplished through a process known as deep-level transient spectroscopy (DLTS): a high-frequency capacitance transient thermal scanning technique that uses the electrical properties of a semiconductor to measure deep-level parameters (Figure 5-1).

The basic concept deals with the change in capacitance of a semiconductor by the injection of carriers (minority or majority) into the sample by a bias pulse. This changes the electron occupation of a trap from an initial state. Because free carriers can interact with electronic defects through a thermal process, a charge exchange takes place and establishes the thermal capture and emission rates. Based on these rates, the electron occupation will return to an equilibrium state and the capacitance will return to its quiescent value. If a deep-level trap exists within the depletion region of the sample, a capacitance transient will be detected. Figures 5-2 and 5-3 illustrate an injection pulse used to produce a capacitance transient for the case of minority-carrier (electron) and majority-carrier (hole) traps respectively. The figures also illustrate that the capacitance transient is an exponential function of time. Figure 5-3 further details the time dependence where  $e_2$  is the thermal emission rate for majority carriers and  $e_1$  is the thermal emission rate for minority carriers. The sign of the capacitance change depends on an increase or decrease in the electron occupation of the trap caused by the pulse. An increase in trapped minority

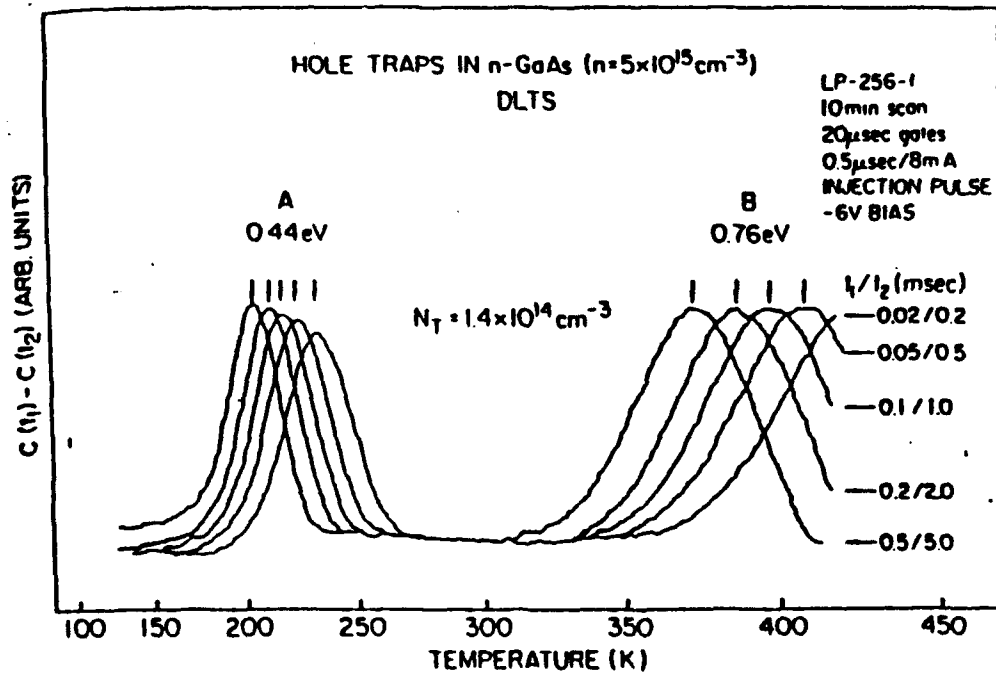


Figure 5-1. Typical experimental DLTS spectra for hole traps in n-GaAs. The two traps are labeled A and B and have activation energies measured from the valence band of 0.44 and 0.76 eV, respectively. The trap concentrations are both  $1.4 \times 10^{14} \text{ cm}^{-3}$ . Five different spectra are shown corresponding to the five rate windows determined by the values of  $t_1$  and  $t_2$ . [from Ref. 19]

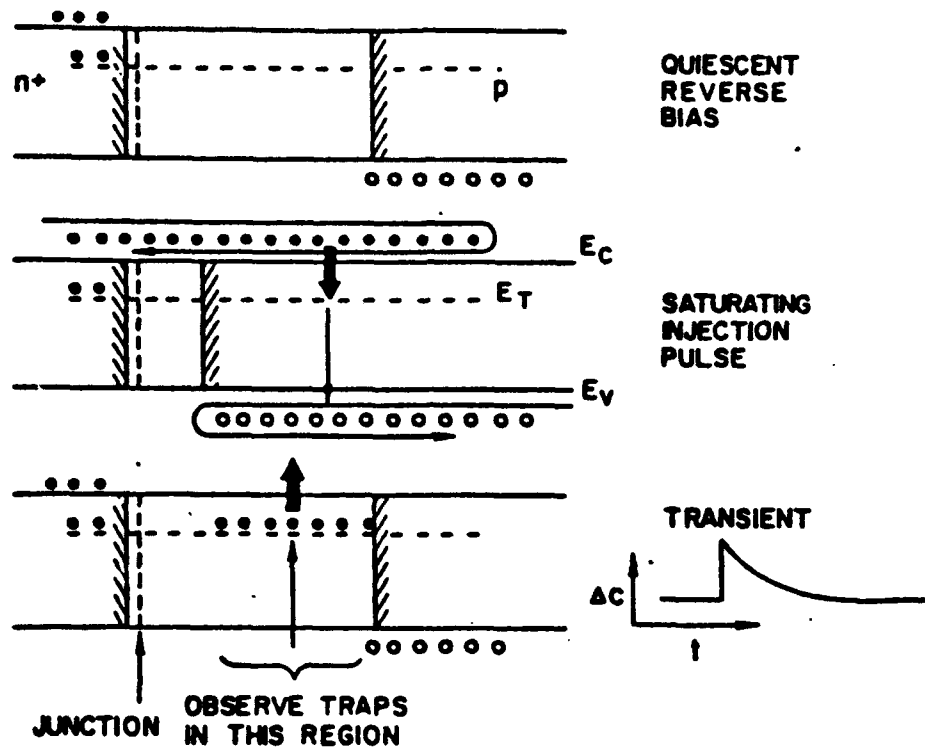


Figure 5-2. Injection pulse sequence which is used to produce a capacitance transient for a minority-carrier trap. The energy-vs-distance diagrams (will band bending omitted for simplicity) show the p n junction depletion region (edges denoted by shaded lines) as well as the capture and emission processes and trap occupation before, during, and after an injection pulse. [from Ref. 19]

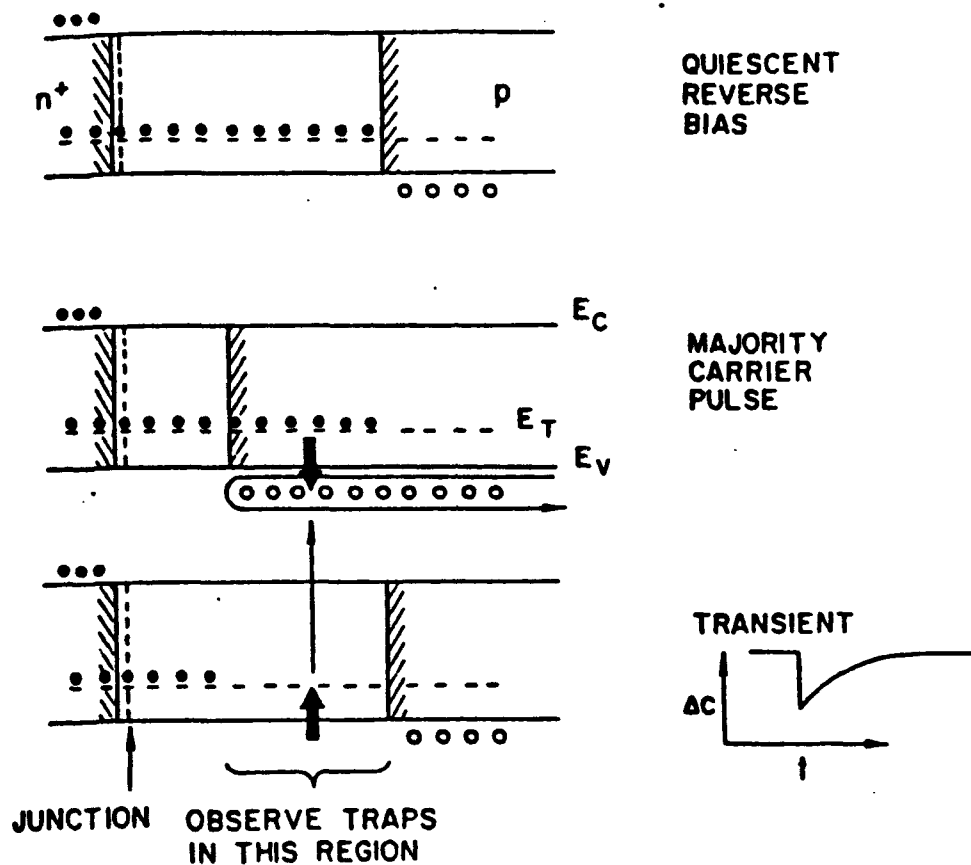


Figure 5-3. Majority-carrier pulse sequence which is used to produce a capacitance transient for a majority-carrier trap. The energy-vs-distance diagrams (with band bending omitted for simplicity) show the p n junction depletion region (edges denoted by shaded lines) as well as the capture and emission processes and trap occupation before, during, and after a majority-carrier pulse. [from Ref. 19]



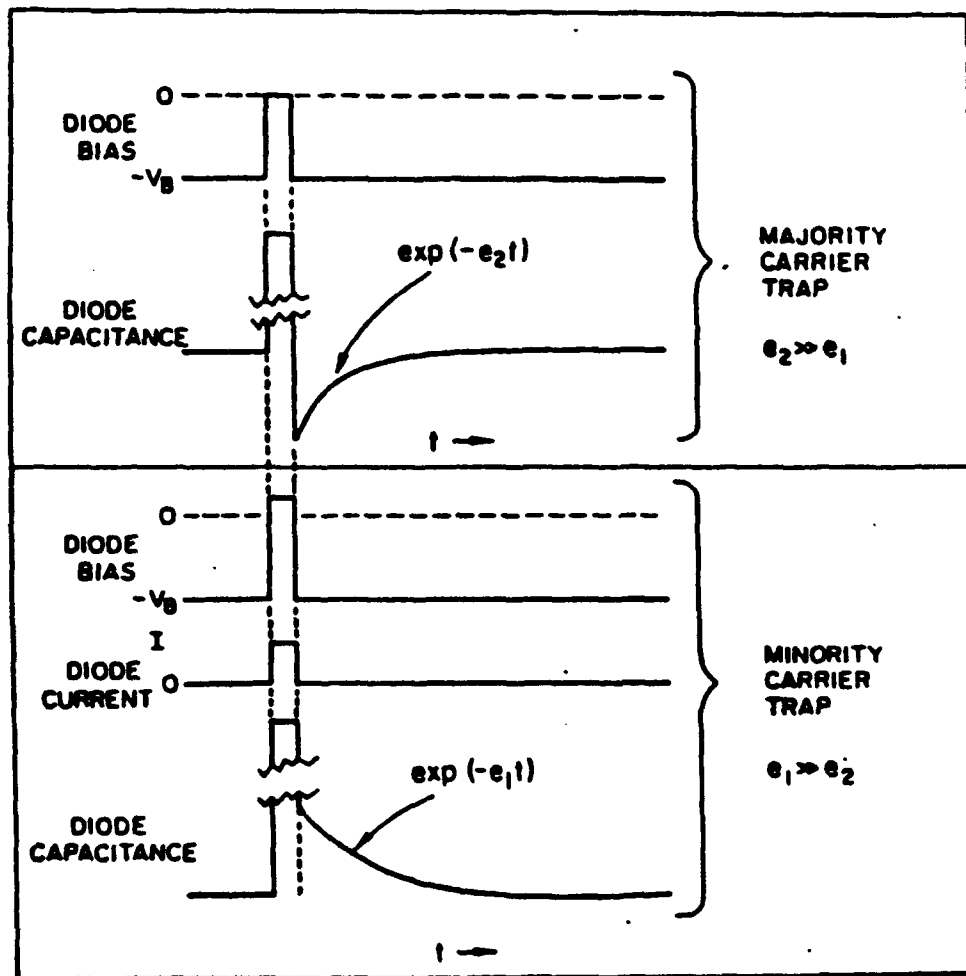


Figure 5-4. typical dependences involved in pulsed bias capacitance transients for majority- and minority-carrier traps. The upper half is a majority-carrier pulse sequence while the lower half is an injection-pulse sequence. [from Ref. 19]

carriers causes a decrease in junction capacitance. The capacitance transient due to minority carrier traps is always positive and is induced only by injected minority carriers, whereas the transient due to majority-carrier traps is always negative and is induced only by majority carriers [Ref. 19:p. 3025].

DLTS uses the capacitance transient and emission rate to uniquely identify traps. This is done by the rate window concept. Basically, a thermal emission rate window is set such that the measurement system responds only to transients with an emission rate within a particular window. Since the emission rate and thus the transient is dependent on temperature, the system will measure a peak at the temperature where the trap emission rate is within the window as shown in Figures 5-5 and 5-6. Thus, the temperature will uniquely define the trap responsible for the transient. It is from these peaks that much of the information concerning the trap is determined.

## **B. DATA AND EQUATIONS**

As stated earlier, the DLTS technique provides information concerning thermal emission rates, activation energy, density and capture cross section by recombination centers that come about from the presence of deep levels in the bandgap of the semiconductor.

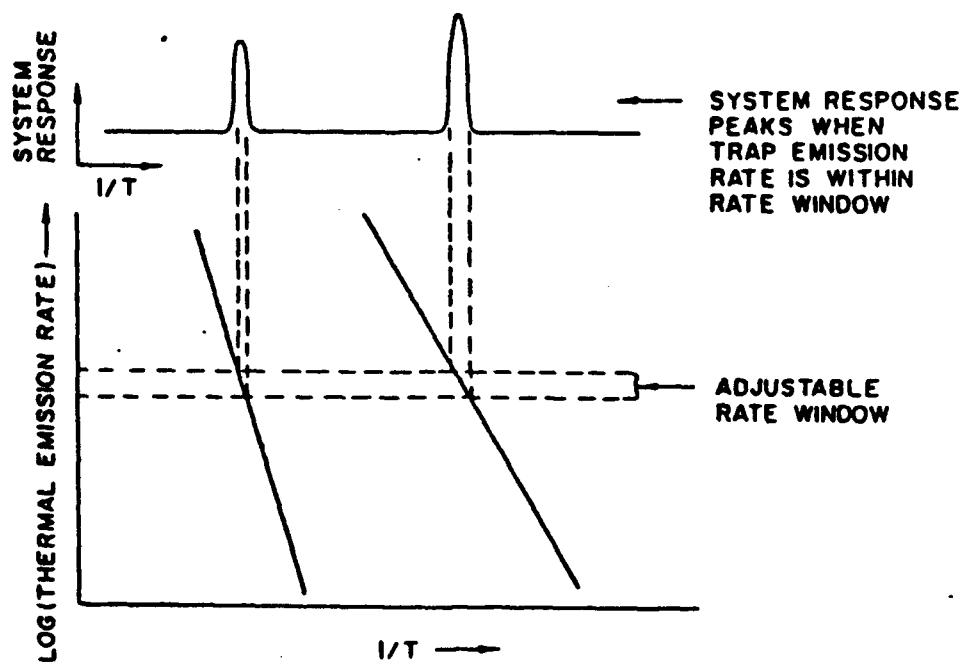


Figure 5-5. Schematic illustration of the basic idea of DLTS method, namely, the rate window concept. The lower part of the figure is a typical activation energy plot for the case of two traps. The upper part of the figure shows the resulting response of a capacitance transient measurement apparatus equipped with a rate window.

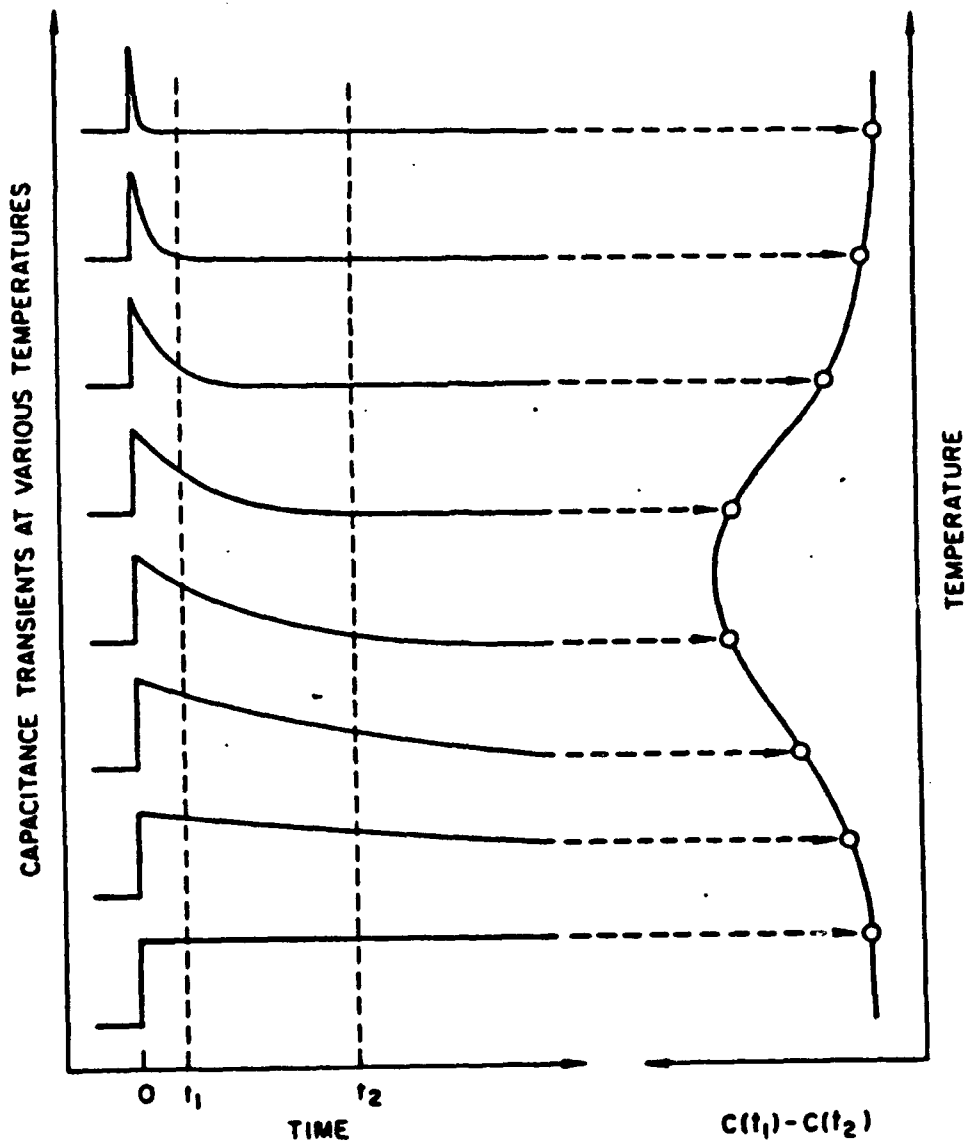


Figure 5-6. Illustration of how a DLTS signal is defined. The left-hand side shows capacitance transients at various temperatures, while the right-hand side shows the corresponding DLTS signal resulting from using the double boxcar to display the difference between the capacitance at time  $t_1$  and the capacitance at time  $t_2$  as a function of temperature. [from Ref. 19]

The thermal emission rate  $e$  is formed by

$$e = \left[ \frac{N\sigma v}{g} \right] \exp \left( \frac{-\Delta E}{kT} \right) \quad (5.1)$$

where

$N$  = effective density of states in the band with which the trapped carriers interact ( $N_c$  for minority carriers,  $N_v$  for majority carriers)

$\sigma$  = capture cross section

$v$  = thermal velocity of minority-carriers (majority carriers)

$g$  = degeneracy of the trap level

$\Delta E$  = energy of the trap (the energy separation between the trap level and the carrier band)

$k$  = Boltzsmann's constant

$T$  = temperature

The activation energy of the trap can be determined by a plot of:

$$\text{Log } e/T^2 \text{ vs } 1/T$$

as seen in Figure 5-5. The slope of the resulting straight line is reported as the activation energy of the trap.

The concentration of a trap can be obtained by either saturation injection pulse or by concentration profile. The capacitance change associated with a complete filling of the trap with a saturating injection pulse (minority carrier trap) or the largest possible majority carrier pulse provides a relationship for an electron trap in an n+p step junction by

$$N = 2(\Delta C/C)(N_A - N_D) \quad (5.2)$$

where  $N$  is the trap concentration,  $\Delta C$  is the capacitance change at  $t=0$  due to a saturating injection pulse,  $C$  is the capacitance of the semiconductor under quiescent reverse-biased conditions and  $N_A - N_D$  is the net acceptor concentration on the p side of the junction where the trap is observed [Ref. 19:p. 3025].

Concentration profiling provides a more precise determination of trap concentration even though it requires a number of scans for good resolution. Figure 5-7 shows an example of concentration profiling with DLTS. Each successive scan uses a progressively larger majority-carrier pulse. To obtain the profile, a plot of signal destruction versus pulse voltage is used (Figure 5-8). Using the following equation plus the two plots above, determines the concentration of the trap.

$$N_T = 2(\Delta C_0/C)(N_A - N_D) \quad (5.3)$$

The capture rate of the trap,  $c$ , is given by [Ref. 11:p. 179)

$$N(t) = N_T \left[ 1 - \exp(-ct) \right] \quad (5.4)$$

where

$$\begin{aligned} N(t) &= \text{density of traps filled by a bias} \\ &\quad \text{pulse of width } t \\ N_T &= \text{total trap density} \end{aligned}$$

$N(t)$  values are obtained from peak heights measured at different bias pulse widths and  $N_T$  corresponds to the pulse width that saturates all the traps [Ref. 11:p. 179]. The

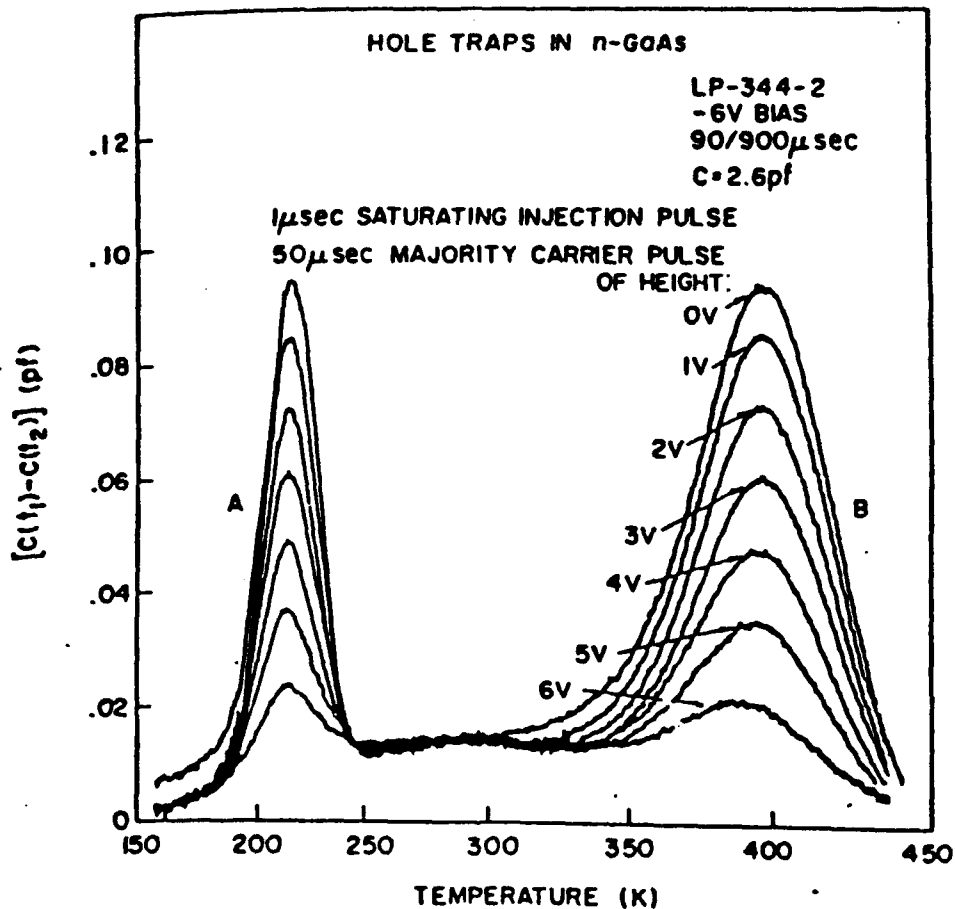


Figure 5-7. Example of concentration profiling with DLTS. On all runs the traps are filled with holes by a 1 microsecond saturating injection pulse followed a few microseconds later by a 50 microsecond majority-carrier pulse of variable amplitude. The resulting DLTS signal destruction due to successive scans with increasing amplitude of the second pulse is the basic information used to determine the trap concentration profile.

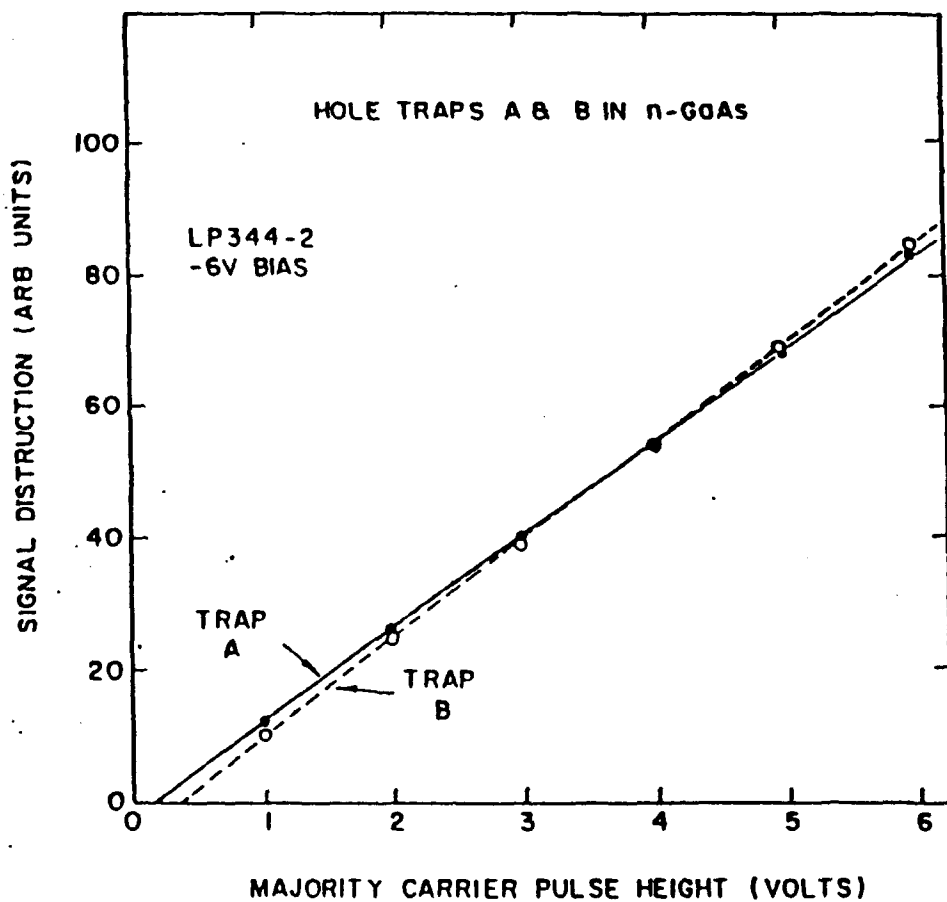


Figure 5-8. Signal destruction vs majority-carrier pulse height (in volts) for DLTS scans in Figure 5-7. The linear dependence obtained indicates a uniform concentration for these two traps of  $1.4 \times 10^{14} \text{ cm}^{-3}$ . [from Ref. 19]



value of  $c$  is determined through a plot of  $\ln [N_T - N(+)/N_T]$  versus  $t$  which in turn yields the capture cross section,  $\sigma$ , by the relationship

$$c = \sigma NV \quad (5.5)$$

Summarizing, the presence of a trap is indicated by a positive or negative peak on a plot of the DLTS signal as a function of temperature. The magnitude of the peaks is proportional to the trap concentration while the sign of the peak (positive or negative) indicates a majority or minority carrier trap. The position of the peaks is determined by the gate settings and the thermal emission properties of the traps. The proper choice of parameters enables the measurement of the thermal emission rate, activation energy, concentration profile and capture rate of each trap, uniquely identified [Ref. 19:p. 3023]. DLTS is the technique for detecting defects in semiconductor material by yielding complete information on the defect in terms of the parameters mentioned above. Through this information, further study into defect annealing can take place.

## VI. GALLIUM ARSENIDE SOLAR CELLS

### A. GaAs CELL CHARACTERISTICS

The significance of GaAs is its radiation hardness as well as its efficiency in photovoltaic conversion. These are its main advantages over silicon. Because of its nearly ideal bandgap (1.42 eV), efficiencies of up to 22% have been recorded.

As most compounds of the III-V group of the periodic table, GaAs crystallizes in the zincblende structure (Figure 2-1). Each gallium atom is surrounded by four atoms of arsenic. As such, the structure causes the material to be a direct bandgap semiconductor. In other words, photons are absorbed almost immediately after entering the cell. Also, the minority carriers' lifetimes and diffusion length are much smaller compared to a semiconductor such as silicon which is an indirect bandgap semiconductor. The quick absorption of energy also contributes to the radiation resistance of GaAs cells. A list of physical and electronic properties of GaAs as well as their semiconductor material is given in Appendix A.

The GaAs cells used in this research were 2 x 2 cm p-n type with a germanium substrate manufactured by Applied Solar Energy Corporation. The cells were produced using metalorganic chemical vapor deposition (MOCVD) techniques. A

cross-sectional view of the cell is shown in Figure 6-1 with corresponding manufactured characteristics. Four cells were used through the experiment. However, because of the results observed, additional cells were used for verification. Initial characteristics of the cells will be found in the initial I-V curves in Appendix B.

#### **B. EXPERIMENT OBJECTIVE AND PLAN**

Cypranowski [Ref. 2] determined the optimum annealing process for radiation-damaged GaAs solar cells. The objective of the experiment was to reproduce the results while analyzing the damage and annealing mechanisms associated with the process using a technique known as deep-level transient spectroscopy. An initial DLTS measurement was to be made on the pre-indicated cells to establish a baseline for the analysis. The cells were then irradiated with 1-MeV electrons at the Jet Propulsion Laboratory in Pasadena with the Dynametron Linear accelerator for a total fluence of  $1E14$  electrons/cm<sup>2</sup>. Once damaged, two cells would be annealed using thermal and forward biased annealing established in previous research [Ref. 1] and two cells would be annealed using only thermal annealing.

After each step in the process, I-V curves would be taken and the cell would then be cut to allow DLTS measurements. The process was done for multiple cycles to establish a pattern of trap level fluctuations based on damage and recovery.

## Gallium Arsenide on Germanium Solar Cells

CELL SPECIFICATIONS							
Test Conditions: AMO, 135.3 mW/cm <sup>2</sup> , 28°C							
Parameter	Symbol	Unit	22 Ge-200	24 Ge-200	24 Ge-90	44 Ge-200	44 Ge-90
Cell Size	—	cm	2 x 2	2 x 4	2 x 4	4 x 4	4 x 4
Cell Thickness	—	μm	200	200	90	200	90
Efficiency	η	%	18.5	18.5	18.0	18.5	18.0
Open Circuit Voltage	V <sub>oc</sub>	V	1.000	1.000	1.000	1.000	1.000
Short Circuit Current	I <sub>sc</sub>	mA	122	244	242	488	484
Optimum Load Voltage	V <sub>L</sub>	V	0.870	0.870	0.865	0.870	0.865
Load Current	I <sub>L</sub>	mA	115	230	225	460	450
Maximum Power	P <sub>max</sub>	mW	100	200	195	400	390
Weight	—	gm	0.454	0.908	0.425	1.816	0.850
Solar Absorptance**	α <sub>s</sub>	—	0.870	0.870	0.870	0.870	0.870

\*\*350 nm filter

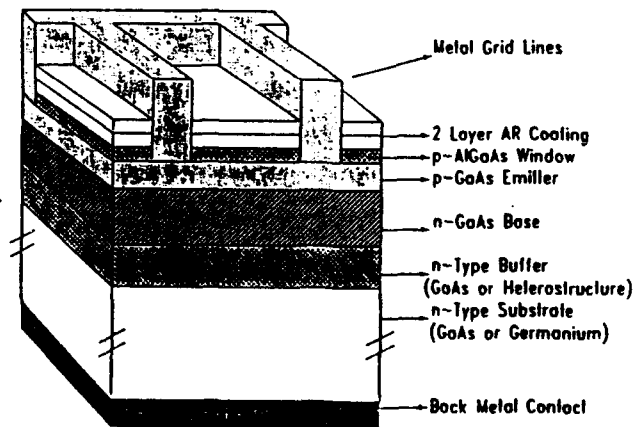
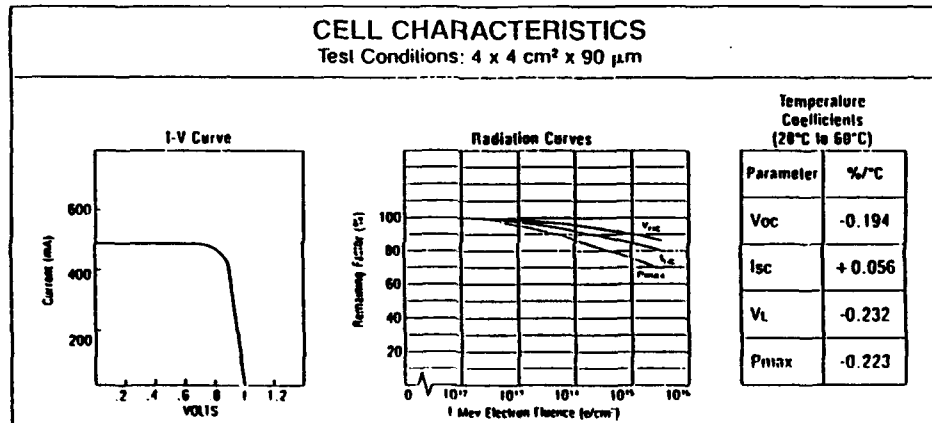


Figure 6-1. Cross sectional view and manufactured characteristics of GaAs/Ge cells (courtesy Applied Solar Energy Corporation)

### C. EXPERIMENTAL PROCEDURE AND RESULTS

Cells numbered 2 and 6 were irradiated at  $1E14$  electrons/cm<sup>2</sup> fluence for each cycle throughout the experiment. They were annealed at 90°C with 0.5A/cm<sup>2</sup> in darkness for 48 hours. The cells went through three cycles of the process. I-V curves are illustrated in Appendix B, Figures B.1 - B-6.

Open current voltage ( $V_{oc}$ ), short circuit current ( $I_{sc}$ ) and maximum power ( $P_{max}$ ) at each step was plotted for cells 2 and 6 and are illustrated in Appendix C, Figures C.1 - C.6.

Observations revealed that  $V_{oc}$  degraded on both cells particularly after annealing. The  $I_{sc}$  for cells #2 recovered and was able to maintain 93% of its initial value after receiving an accumulated dose of  $3E14$  electrons/cm<sup>2</sup>. However, after the third annealing the  $I_{sc}$  degraded to 76% of its initial value.  $I_{sc}$  for cell #6 showed initial degradation after the first irradiation and annealing. Further degradation occurred after the second irradiation and some recovery after the second anneal.

The maximum power observed in both cells showed severe degradation after the first anneal with recovery from the second irradiation. The second annealing gave slight recovery from the second irradiation. The second annealing gave slight recovery to cell #2 but continued to degrade #6.

Two additional cells were used to verify the results observed on cells 2 and 6. Similar outputs occurred. I-V

curves and parameter plots are illustrated in Appendix B, Figures B.7 - B.10 and Appendix C, Figures C.7 - C.12, respectively.

Cells numbered 4, 5, and 8 were irradiated at  $1E14$  electrons/cm<sup>2</sup> fluence for each cycle throughout the experiment. They were thermally annealed only at 90°C in darkness for 48 hours. Cells 4 and 5 went through three cycles of process while cell #8 went through one complete cycle to verify the results observed. The I-V curves are illustrated in Appendix B, Figures B.11 - B.18.

Open circuit voltage ( $V_{oc}$ ), short circuit current ( $I_{sc}$ ), and maximum power ( $P_{max}$ ) at each step was plotted and illustrated in Appendix C, Figures C.13 - C.21.

$V_{oc}$  for all three cells had little degradation, maintaining better than 96% of the initial values after an accumulated dose of  $3E14$  electrons/cm<sup>2</sup>.  $I_{sc}$  also recovered well with each annealing, maintaining better than 93% of the initial value.

The maximum power showed initial degradation but was able to recover after the annealing process. After three cycles, and an accumulated dose of  $3E14$  electrons/cm<sup>2</sup>, cells 4 and 5 were able to maintain better than 99% of the cells' initial maximum power. Cell 8 was able to maintain 95.6% of its initial maximum power after  $2E14$  electrons/cm<sup>2</sup> dose.

#### D. DLTS

Previous research with DLTS on gallium arsenide [Refs. 18 and 20] show that after electron irradiation, that three

defect levels are introduced. The deep levels are known as the E3, E4, and E5 defects with energies of 0.31, 0.71, and 0.90 eV, respectively. Sheng, et al [Ref. 20] illustrates a DLTS scan of electron traps in a one-MeV electron irradiated (AlGa)AS - GaAs solar cell as a function of annealing time (Figure 6-2). It is noted that the concentration of the traps decreases with increasing annealing time. However, the density of E5 defect increased with the 60-minute anneal time at 230°C, indicating that a greater number of defects are being created at this level through annealing.

The results observed in this research were inconsistent with both Cypranowski's work [Ref. 2] and Sheng [Ref. 20]. Previous work used cells with gallium arsenide substrates and a cell thickness of 300 microns. This research used Gallium Arsenide cells on germanium substrate and a cell thickness of 200 microns. The differences are being examined.

#### **E. CONCLUSIONS**

The cells used in this research provided results which were inconsistent with previous work [Refs. 4 and 20]. However, because the results were repeated in subsequent cells, there may be differences in the effects of the annealing processes used. Because a germanium substrate was used, the thickness of the cell was less (200 microns vs 300 microns). This may affect the forward bias annealing parameter used for GaAs substrate cells. This 0.5 Amps/cm<sup>2</sup> forward bias current may have been too great for the cell and thereby

created more degradations. Similar results using  $.75 \text{ A/cm}^2$  were observed in GaAs substrate cells [Ref. 2].

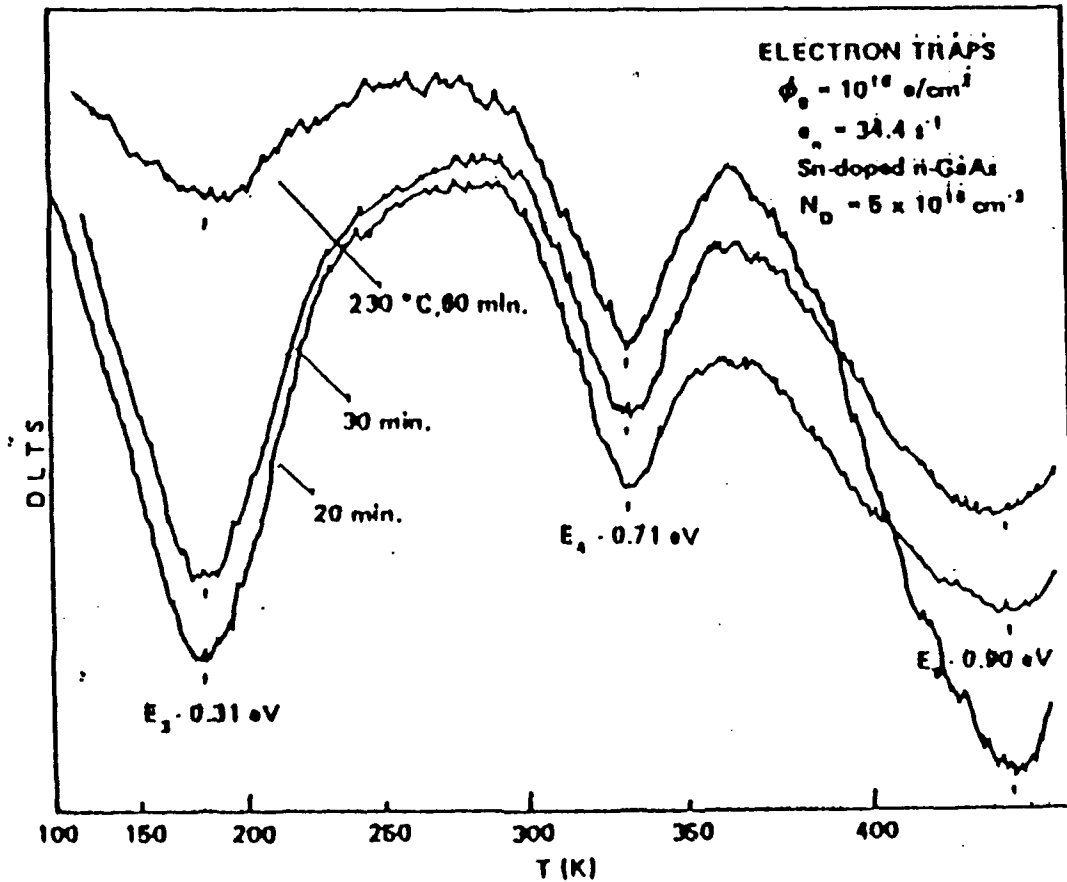


Figure 6-2. DLTS scan of electron traps in one-MeV electron irradiated (AlGa) AsGaAs solar cells as a function of annealing (230°C) time [from Ref. 20]



Thermal annealing for the germanium substrate cells was found to provide greater recovery. However, lower forward bias current could be used to enhance the annealing process.

## VII. INDIUM PHOSPHIDE SOLAR CELLS

### A. InP CELL CHARACTERISTICS

Indium phosphide's exceptionally high resistance to radiation damage compared to GaAs and silicon solar cells, makes it an extremely attractive alternative for space power/. Having a bandgap of 1.35 eV InP cells have typical conversion efficiencies of about 16.5%. The characteristics of InP cells allows for reduction in thickness and weight of the coverglasses which provide protection for the cell. This translates to increased mission payload. Cell cost is high and although InP cells are being manufactured with excellent uniformity, the price is the limiting use factor.

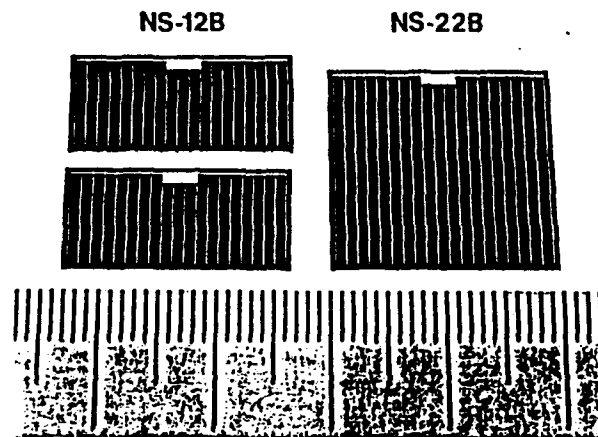
Similar to GaAs, InP crystallizes in the zincblende structure (Figure 2.1). Each indium atom is surrounded by four atoms of phosphorous. A list of physical and electronic properties of InP is given in Appendix A.

The InP cells used in this research were obtained from Cypranowski's research [Ref. 2]. They were manufactured by Nippon Mining Company and 1 x 2 cm n-p type. Typical cell properties are shown in Figure 7.1. Two cells were used throughout the experiment with DLTS measurements being taken. The cells have been previously irradiated and annealed. The

### Typical Properties of Indium Phosphide Solar Cells

Item	Symbol	Unit	Cell Type	
			NS-12B	NS-22B
Cell Area	—	cm <sup>2</sup>	1×2	2×2
Cell Thickness	—	μm	200	200
Open Circuit Voltage	Voc	V	0.825	0.825
Short Circuit Current	Isc	mA	66	134
Optimum Bias Voltage	Vm	V	0.72	0.72
Optimum Bias Current	Im	mA	63	126
Fill Factor	FF	%	83.0	82.0
Conversion Efficiency	η	%	16.5	16.5
Maximum Output Power	Pmax	mW	45.4	90.7
Cell Weight	—	mg	185	370
Power Per Unit Area	—	mW/cm <sup>2</sup>	22.7	22.7
Power Per Unit Weight	—	mW/g	245	245

Electrical properties measured at NASA Lewis Research Center.  
Conditions: Air Mass 0, 25°C



InP solar cells NS12B (1×2cm<sup>2</sup>) and NS22B (2×2cm<sup>2</sup>).

Figure 7-1. Typical cell properties for InP  
(Courtesy Nippon Mining Company)

research uses the last anneal as the reference baseline for each cell. Initial characteristics of the cells will be found in the initial I-V curves in Appendix D.

#### **B. EXPERIMENTAL OBJECTIVE AND PLAN**

Cypranowski [Ref. 2] determined the optimum annealing process for radiation damaged InP solar cells. The objective of this experiment was to reproduce the results while analyzing the damage and annealing mechanisms associated with the process using DLTS. An initial DLTS measurement was to be taken on the previously irradiated cells to establish a baseline for the analyses. The cells were then irradiated with 1-MeV electrons at the Jet Propulsion Laboratory in Pasadena with the Dynamitron lines accelerator for a total fluence of  $1E15$  electrons/cm<sup>2</sup>. Once damaged, the cells would be annealed using thermal and forward biased current annealing established by previous research [Ref. 2].

After each step in the process, I-V curves would be taken and the cell would then be cut to allow DLTS measurements. The process was done for multiple copies to establish a pattern of trap level fluctuation based on damage and recovery.

#### **C. EXPERIMENTAL PROCEDURE AND RESULTS**

Cells numbered 1073 and 1074 have been previously irradiated at  $1E15$  electrons/cm<sup>2</sup> fluence for four cycles. They have also been irradiated for one cycle at  $1E15$

electrons/cm<sup>2</sup> white illuminated. Total fluence was 5E15 electrons/cm<sup>2</sup>. After each irradiation, the cells were annealed under several different parameters [see Ref. 2]. The I-V curves for these cells are illustrated in Appendix D, Figures D.1 - D.10.

This research irradiated the cells at 1E15 electrons/cm<sup>2</sup> fluence for each cycle throughout the experiment. The cells were then annealed at 90°C with 0.25 A/cm<sup>2</sup> forward biases current in darkness 2 hours. Both cells went through two complete cycles of irradiation and annealing. I-V curves for these are found in Appendix D, Figures D.11 - D.15.

Open circuit voltage ( $V_{oc}$ ), short circuit current ( $I_{sc}$ ) and maximum power ( $P_{max}$ ) at each step were plotted and are illustrated in Appendix E, Figures E.1 - E.6.

Observations revealed that  $V_{oc}$  and  $I_{sc}$  degradation was slight after the first irradiation with good recovery after the first annealing. After the second cycle, the accumulated fluence was 7E15 electrons/cm<sup>2</sup>. Cell number 1073 maintained 96.8% of the initial  $V_{oc}$  value and 93.8% of its initial  $I_{sc}$  value while cell 1074 maintained 91.6% of its initial  $V_{oc}$  value and 89% of its initial  $I_{sc}$  value.

The maximum power observed in both cells showed marked degradation even after the annealing process. However, the annealing process did, to an extent, stem the increasing degradation of the irradiation.

#### D. DLTS

Indium Phosphide research by Yamaguchi, et al [Ref. 21] identifies two major defect levels associated with radiation damage (Figure 7.2). The DLTS was taken on p-InP after 1-MeV electron radiation with  $1E15$  electrons/cm<sup>2</sup> fluence and successive thermal annealings at 410°K. The defect centers in the figure are labeled H4 and H5 for hole traps, in accordance with Yamaguchi's findings. The major defect state introduced by electron irradiation in p-InP is the 0.37 eV hole trap H4. This has been confirmed to be a recombination center [Ref. 21, p. 5559]. This defect center is annealed out after 30 minutes of annealing at 410° K. Solar cell degradation and recovery is associated with the introduction and annealing out of the defect center.

A second hole trap, H5, is introduced with an energy level of 0.52 eV. Contrary to the effect of annealing on H4, the H5 defect density grows with increasing annealing time. This could be associated with the overall permanent degradation of the cell. H5 is considered to be a point-defect-impurity complex such as a phosphorous vacancy-zinc bond or a phosphorous interstitial-zinc bond. H4 is considered to be a point defect such as a phosphorous vacancy or phosphorous interstitial [Ref. 21].

Based on this information, the research has taken the process one step further. DLTS measurements were taken on samples that have been repetitively irradiated and annealed.

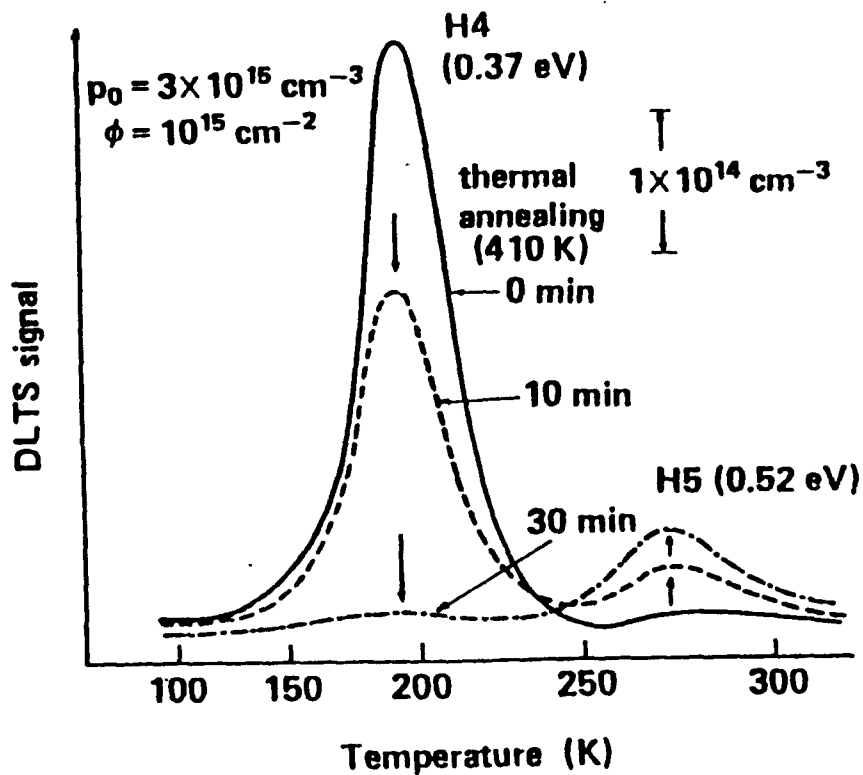


Figure 7-2. DLTS spectra for hole traps in p-InP with a carrier concentration of  $3 \times 10^{15} \text{ cm}^{-3}$  following a 1-MeV electron irradiation of  $1 \times 10^{15} \text{ cm}^{-2}$  fluence and successive thermal annealings at 410 K. [from Ref. 21]

DLTS was performed on InP cell 1073 at Aerospace Corporation using the Deep Level Spectrometer manufactured by Sula Technologies. Parameters, measurements, and calculations were set, taken and made in accordance with the DLTS operating manual [Ref. 22] and Barnes' course on DLTS [Ref. 23]. Carrier concentrations is assumed to be  $6.5E16 \text{ cm}^{-3}$ . Equations and sample calculations are illustrated in Appendix F along with energy and capture cross section plots.

Consistent with Yamaguchi's findings, two trap levels were observed H4 at a level of approximately 0.32eV and H5 at a level of 2.54 eV. Table 7.1 summarizes the data obtained from the cell. The energy levels of the traps were found by two similar methods for the Arrhenious plots. The first method plots the natural logarithm of the emission rate as a function of the inverse of the temperature. The second method plots the natural logarithm of the emission rate divided by the square of the temperature as a function of the inverse of the temperature. The latter method is considered more accurate. The capture cross sections ( $\sigma$ ) and the concentrations are also given for each step in the irradiation and annealing cycles. Figure 7.3 is a plot of the energy level calculations, the slope of the line representing the energy level of the traps.

Figure 7.4 is a concentration plot as a function of the irradiation and annealing cycles and Figure 7.5 is the DLTS spectrum of the cell. As shown, H4 increases with each



TABLE 7.1  
SUMMARY OF DLTS DATA FOR InP CELL NO. 1073

	A	B	C	D	E	F	G	H	I	J	K	L	M
1	InP 1073 Summary Data												
2													
3			Et by ep peak 1	Et by ep peak 2	Et by ep/ $T^2$ peak 1	Et by ep/ $T^2$ peak 2	Et by ep/ $T^2$	sigma	sigma	sigma	sigma	Conc.	Conc.
4								peak 1	peak 2	peak 1	peak 2	peak 1	peak 2
5													
6													
7	REF		0.44	0.58	0.4	0.53	0.53	4.7E-20	4.4E-21	4.4E-21	1.8E+14	1.8E+14	2.4E+15
8	P11		0.37	0.69	0.33	0.64	0.64	5.10E-21	3.20E-21	3.20E-21	5.1E+14	5.1E+14	2.4E+15
9	PA1		0.42	0.58	0.38	0.53	0.53	5E-22	2.1E-21	2.1E-21	2.4E+14	2.4E+14	7.7E+14
10	P12		0.42	0.68	0.38	0.63	0.63	1.1E-22	2.3E-22	2.3E-22	4E+14	4E+14	5.8E+14
11	PA2		0.37	0.67	0.33	0.62	0.62	1.3E-22	2.9E-21	2.9E-21	2E+14	2E+14	8.8E+14
12		Average	0.404	0.64	0.364	0.59	0.59						
13													

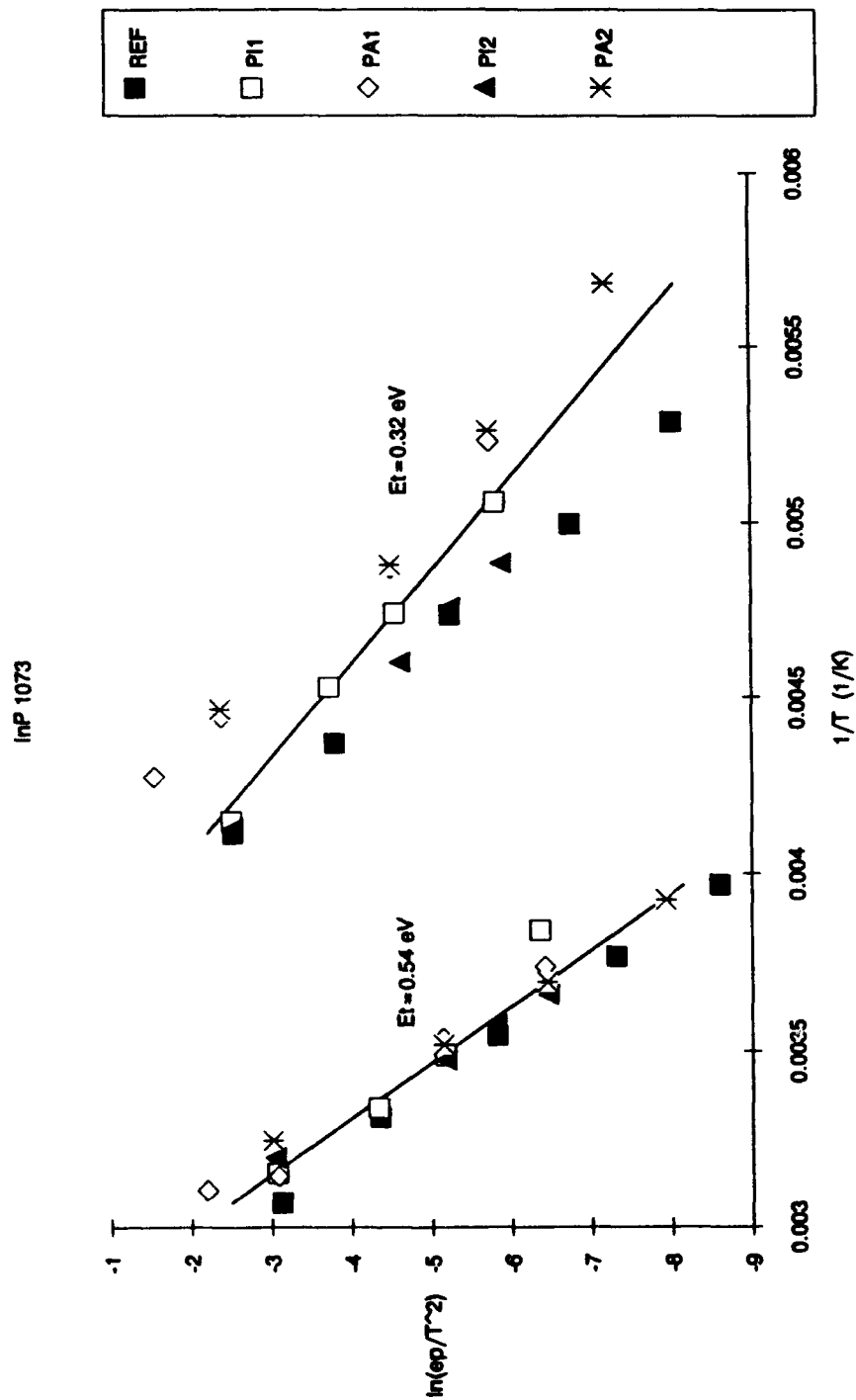


Figure 7-3. Plot of energy level calculations for InP cell 1073: Slope of the straight line represents trap energy level

InP 1073

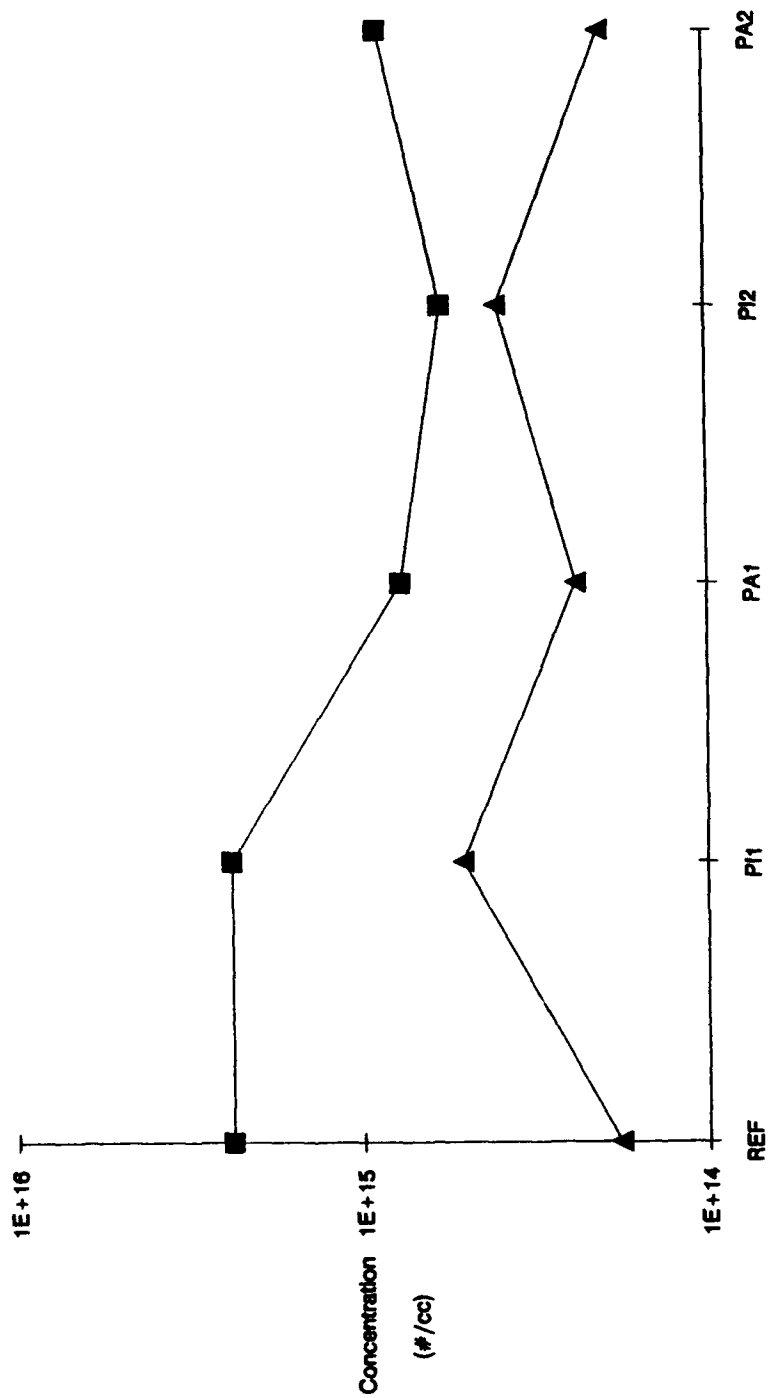


Figure 7-4. Trap level concentration for InP cell 1073

DLTS Spectra of InP Solar Cell 1073

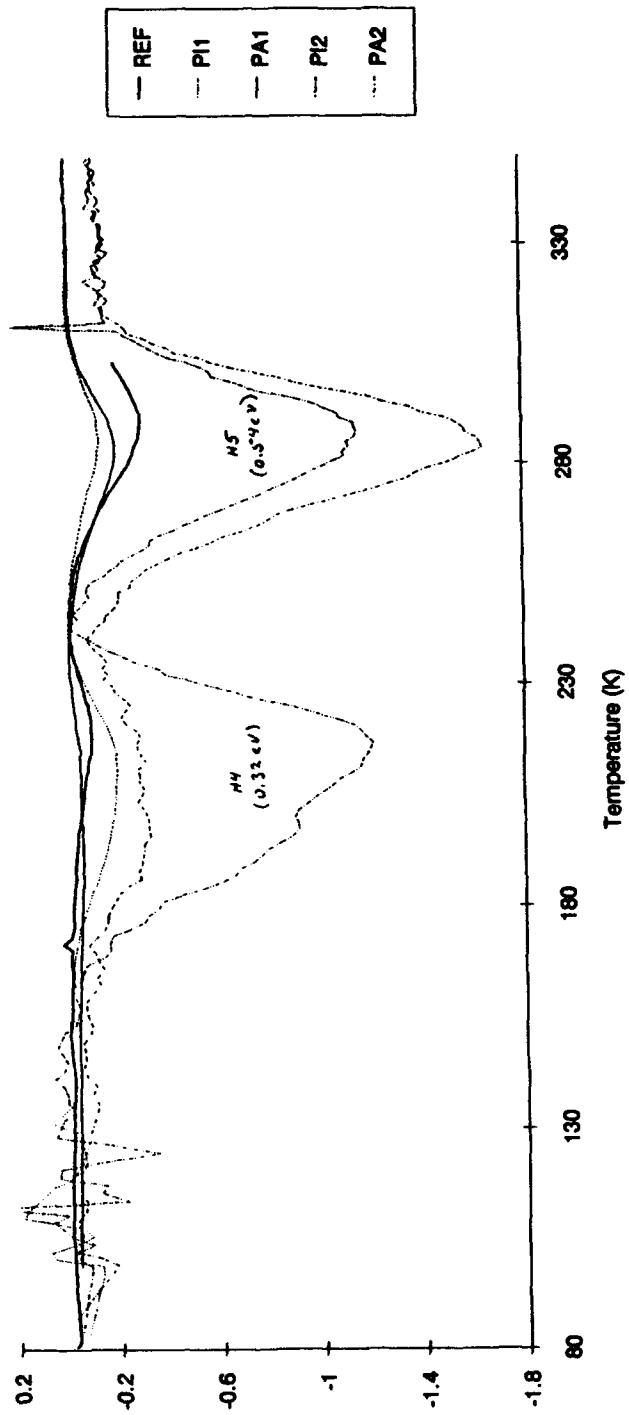


Figure 7-5. DLTS spectra of InP cell 1073

irradiation and decreases with each subsequent annealing. The higher level trap, H5, initially decreases with annealing but then grows with the second annealing cycle. It is believed that this trap will continue to grow with subsequent annealing, based on Yamaguchi's results. These concentrations seem to indicate that solar cell recovery is affected mainly by the H4 trap while the overall permanent degradation of the cell is associated with the high level H5 trap.

### VIII. CONCLUSIONS AND RECOMMENDATIONS

After several cycles of irradiating and annealing GaAs cells, it was found that thermal annealing provided significantly better recovery performance than thermal annealing with forward bias current. Because the GaAs cells were on germanium substrate and thicknesses were only 200 micron, investigation into whether a lower forward bias current is needed which would provide the optimum annealing mechanism for the cells. Chung, et al [Ref. 24] determined that GaAs/Ge cells were more responsive to thermal annealing than GaAs/GaAs cells. Sheng [Ref. 20] illustrates a DLTS scan of electron traps on a one-MeV electron irradiated (AlGa)As - GaAs cell. The illustration (Figure 6.2) shows that the E3 level trap can be annealed out while the E4 trap anneals less readily and the E5 trap grows with increasing anneal time. This indicates that, similar to InP, recovery is a function of the lower level trap and the mid level trap. The E4 trap might account for the lack of greater recovery as seen in InP. The E5 trap could be associated with the overall permanent degradation of the cell.

Indium phosphide showed the H4 and H5 traps as the main contributors to degradation and recovery. H4 is responsible for recovery and H5 is responsible for overall permanent degradation.

This research is preliminary in its context. Further research into the mechanisms behind the irradiation and annealing process is required using new InP and GaAs/Ge cells having standardized smaller sample size.

In order to obtain the proper size for DLTS measurements (approximately  $1\text{mm}^2$ ), the solar cells were cut with a diamond saw. Observations under the microscope revealed that the edge of the cut sample was jagged which may account for the degradation of solar cell performance through the increase in leakage current. Future research should take this into account. Photolithography is a viable option to cutting in providing a properly edged sample.

Methods to compensate for the growth of the H5 and E5 level traps need to be investigated also. The possibility of using heterojunction cells to overcome the H5 and E5 trap effects could be realized. Also, varying dopant concentration experiment to determine the effect on the higher level trap could be conducted.

Future research in this area should have one common purpose: power recovery in solar cells. The life extension of satellites is realizable and satellite mission life will no longer be a function of solar cell end-of-life.

APPENDIX A  
PHYSICAL AND ELECTRICAL PROPERTIES OF  
SOME IMPORTANT SEMICONDUCTORS  
[Ref. 5]



# Properties of Important Semiconductors

Semiconductor	Bandgap (eV)		Mobility at 300 K (cm <sup>2</sup> /V-s) <sup>a</sup>		Band <sup>b</sup>	Effective Mass m <sup>*</sup> /m <sub>0</sub>		ε <sub>s</sub> /ε <sub>0</sub>	
	300 K	0 K	Elec.	Holes		Elec.	Holes		
Element	C	5.47	5.48	1800	1200	I	0.2	0.25	5.7
	Ge	0.66	0.74	3900	1900	I	1.64 <sup>c</sup>	0.04 <sup>c</sup>	16.0
	Si	1.12	1.17	1500	450	I	0.082 <sup>d</sup>	0.28 <sup>f</sup>	11.9
	Sn		0.082	1400	1200	D	0.98 <sup>c</sup>	0.16 <sup>c</sup>	
							0.19 <sup>d</sup>	0.49 <sup>f</sup>	
IV-IV	α-SiC	2.996	3.03	400	50	I	0.60	1.00	10.0
III-V	AlSb	1.58	1.68	200	420	I	0.12	0.98	14.4
	BN	~7.5				I			7.1
	BP	2.0							
	GaN	3.36	3.50	380			0.19	0.60	12.2
	GaSb	0.72	0.81	5000	850	D	0.042	0.40	15.7
	GaAs	1.42	1.52	8500	400	D	0.067	0.082	13.1
	GaP	2.26	2.34	110	75	I	0.82	0.60	11.1
	InSb	0.17	0.23	80000	1250	D	0.0145	0.40	17.7
	InAs	0.36	0.42	33000	460	D	0.023	0.40	14.6
InP	1.35	1.42	4600	150	D	0.077	0.64	12.4	
II-VI	CdS	2.42	2.56	340	50	D	0.21	0.80	5.4
	CdSe	1.70	1.85	800		D	0.13	0.45	10.0
	CdTe	1.56		1050	100	D			10.2
	ZnO	3.35	3.42	200	180	D	0.27		9.0
	ZnS	3.68	3.84	165	5	D	0.40		5.2
IV-VI	PbS	0.41	0.286	600	700	I	0.25	0.25	17.0
	PbTe	0.31	0.19	6000	4000	I	0.17	0.20	30.0

<sup>a</sup>The values are for drift mobilities obtained in the purest and most perfect materials available to date.

<sup>b</sup>Transverse effective mass.

<sup>c</sup>I = indirect, D = direct.

<sup>d</sup>Light-hole effective mass.

<sup>e</sup>Longitudinal effective mass.

<sup>f</sup>Heavy-hole effective mass.

# Lattice Constants

	Element or Compound	Name	Crystal* Structure	Lattice Constant at 300 K (Å)
Element	C	Carbon (diamond)	D	3.56683
	Ge	Germanium	D	5.64613
	Si	Silicon	D	5.43095
	Sn	Grey Tin	D	6.48920
IV-IV	SiC	Silicon carbide	W	$a = 3.086, c = 15.117$
III-V	AlAs	Aluminum arsenide	Z	5.6605
	AlP	Aluminum phosphide	Z	5.4510
	AlSb	Aluminum antimonide	Z	6.1355
	BN	Boron nitride	Z	3.6150
	BP	Boron phosphide	Z	4.5380
	GaAs	Gallium arsenide	Z	5.6533
	GaN	Gallium nitride	W	$a = 3.189, c = 5.185$
	GaP	Gallium phosphide	Z	5.4512
	GaSb	Gallium antimonide	Z	6.0959
	InAs	Indium arsenide	Z	6.0584
	InP	Indium phosphide	Z	5.8686
	InSb	Indium antimonide	Z	6.4794
II-VI	CdS	Cadmium sulfide	Z	5.8320
	CdS	Cadmium sulfide	W	$a = 4.16, c = 6.756$
	CdSe	Cadmium selenide	Z	6.050
	CdTe	Cadmium telluride	Z	6.482
	ZnO	Zinc oxide	R	4.580
	ZnS	Zinc sulfide	Z	5.420
	ZnS	Zinc sulfide	W	$a = 3.82, c = 6.26$
IV-VI	PbS	Lead sulfide	R	5.9362
	PbTe	Lead telluride	R	6.4620

\*D = Diamond, W = Wurtzite, Z = Zincblende, R = Rock salt.

## Properties of Ge, Si, and GaAs at 300 K

Properties	Ge	Si	GaAs
Atoms/cm <sup>3</sup>	$4.42 \times 10^{22}$	$5.0 \times 10^{22}$	$4.42 \times 10^{22}$
Atomic weight	72.60	28.09	144.63
Breakdown field(V/cm)	$\sim 10^5$	$\sim 3 \times 10^5$	$\sim 4 \times 10^5$
Crystal structure	Diamond	Diamond	Zincblende
Density (g/cm <sup>3</sup> )	5.3267	2.328	5.32
Dielectric constant	16.0	11.9	13.1
Effective density of states in conduction band, $N_C$ (cm <sup>-3</sup> )	$1.04 \times 10^{19}$	$2.8 \times 10^{19}$	$4.7 \times 10^{17}$
Effective density of states in valence band, $N_V$ (cm <sup>-3</sup> )	$6.0 \times 10^{18}$	$1.04 \times 10^{19}$	$7.0 \times 10^{18}$
Effective Mass, $m^*/m_0$			
Electrons	$m_{\uparrow}^* = 1.64$ $m_{\downarrow}^* = 0.082$	$m_{\uparrow}^* = 0.98$ $m_{\downarrow}^* = 0.19$	0.067
Holes	$m_{\uparrow_h}^* = 0.044$ $m_{\downarrow_h}^* = 0.28$	$m_{\uparrow_h}^* = 0.16$ $m_{\downarrow_h}^* = 0.49$	$m_{\uparrow_h}^* = 0.082$ $m_{\downarrow_h}^* = 0.45$
Electron affinity, $\chi$ (V)	4.0	4.05	4.07
Energy gap (eV) at 300 K	0.66	1.12	1.424
Intrinsic carrier concentration (cm <sup>-3</sup> )	$2.4 \times 10^{13}$	$1.45 \times 10^{10}$	$1.79 \times 10^6$
Intrinsic Debye length ( $\mu\text{m}$ )	0.68	24	2250
Intrinsic resistivity ( $\Omega\text{-cm}$ )	47	$2.3 \times 10^5$	$10^9$
Lattice constant ( $\text{\AA}$ )	5.64613	5.43095	5.6533
Linear coefficient of thermal expansion, $\Delta L/L\Delta T$ ( $^{\circ}\text{C}^{-1}$ )	$5.8 \times 10^{-6}$	$2.6 \times 10^{-6}$	$6.86 \times 10^{-6}$
Melting point ( $^{\circ}\text{C}$ )	937	1415	1238
Minority carrier lifetime (s)	$10^{-3}$	$2.5 \times 10^{-3}$	$\sim 10^{-8}$
Mobility (drift) (cm <sup>2</sup> /V-s)	3900 1900	1500 450	8500 400
Optical-phonon energy (eV)	0.037	0.063	0.035
Phonon mean free path $\lambda_p$ ( $\text{\AA}$ )	105	76 (electron) 55 (hole)	58
Specific heat (J/g- $^{\circ}\text{C}$ )	0.31	0.7	0.35
Thermal conductivity at 300 K (W/cm- $^{\circ}\text{C}$ )	0.6	1.5	0.46
Thermal diffusivity (cm <sup>2</sup> /s)	0.36	0.9	0.24
Vapor pressure (Pa)	1 at 1330 $^{\circ}\text{C}$ $10^{-6}$ at 760 $^{\circ}\text{C}$	1 at 1650 $^{\circ}\text{C}$ $10^{-6}$ at 900 $^{\circ}\text{C}$	100 at 1050 $^{\circ}\text{C}$ 1 at 900 $^{\circ}\text{C}$

APPENDIX B  
I-V CURVES FOR MULTIPLE CYCLES OF IRRADIATED AND ANNEALED  
GaAs SOLAR CELLS

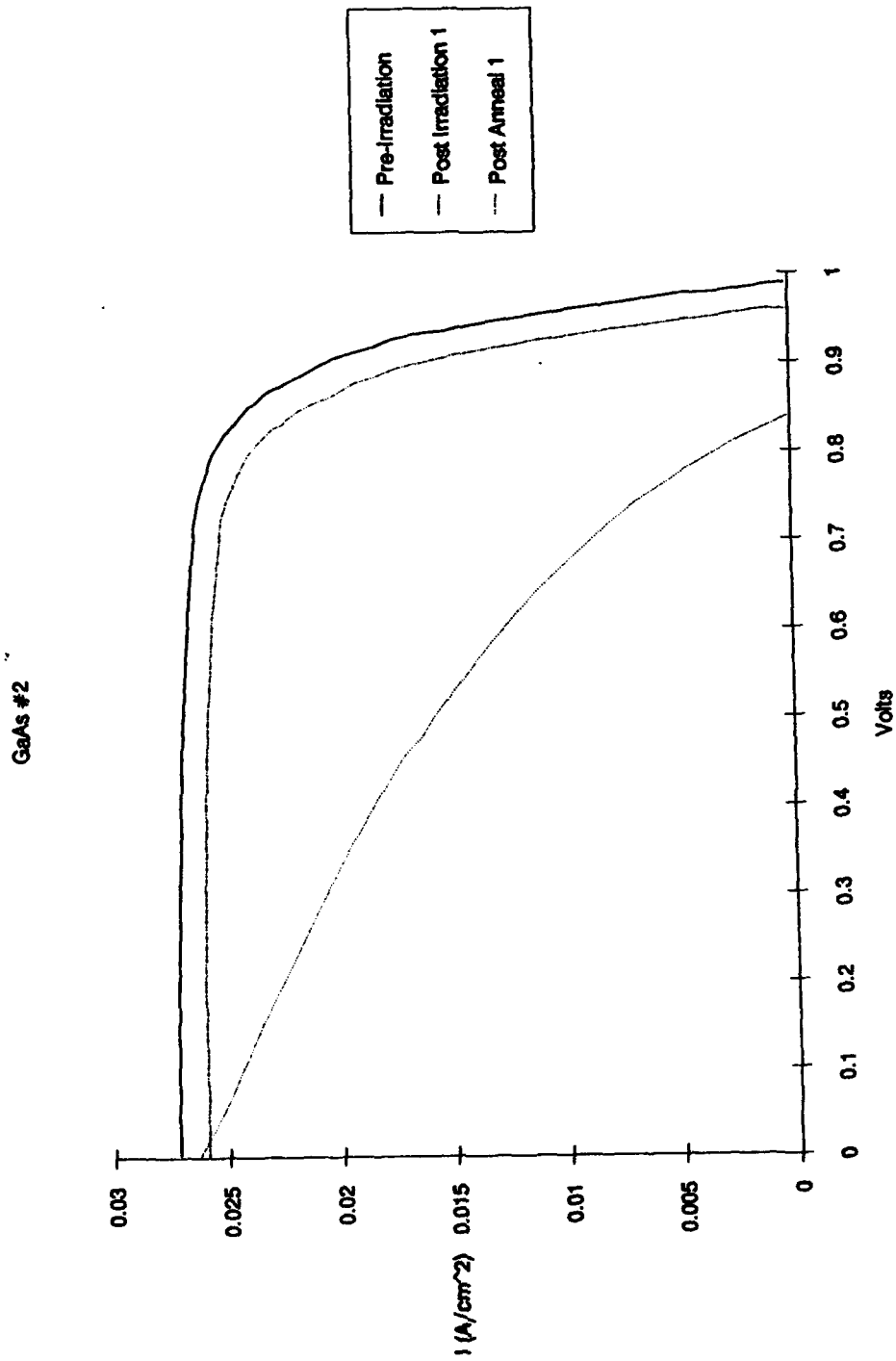


Figure B.1. I-V curves for GaAs cell No. 2

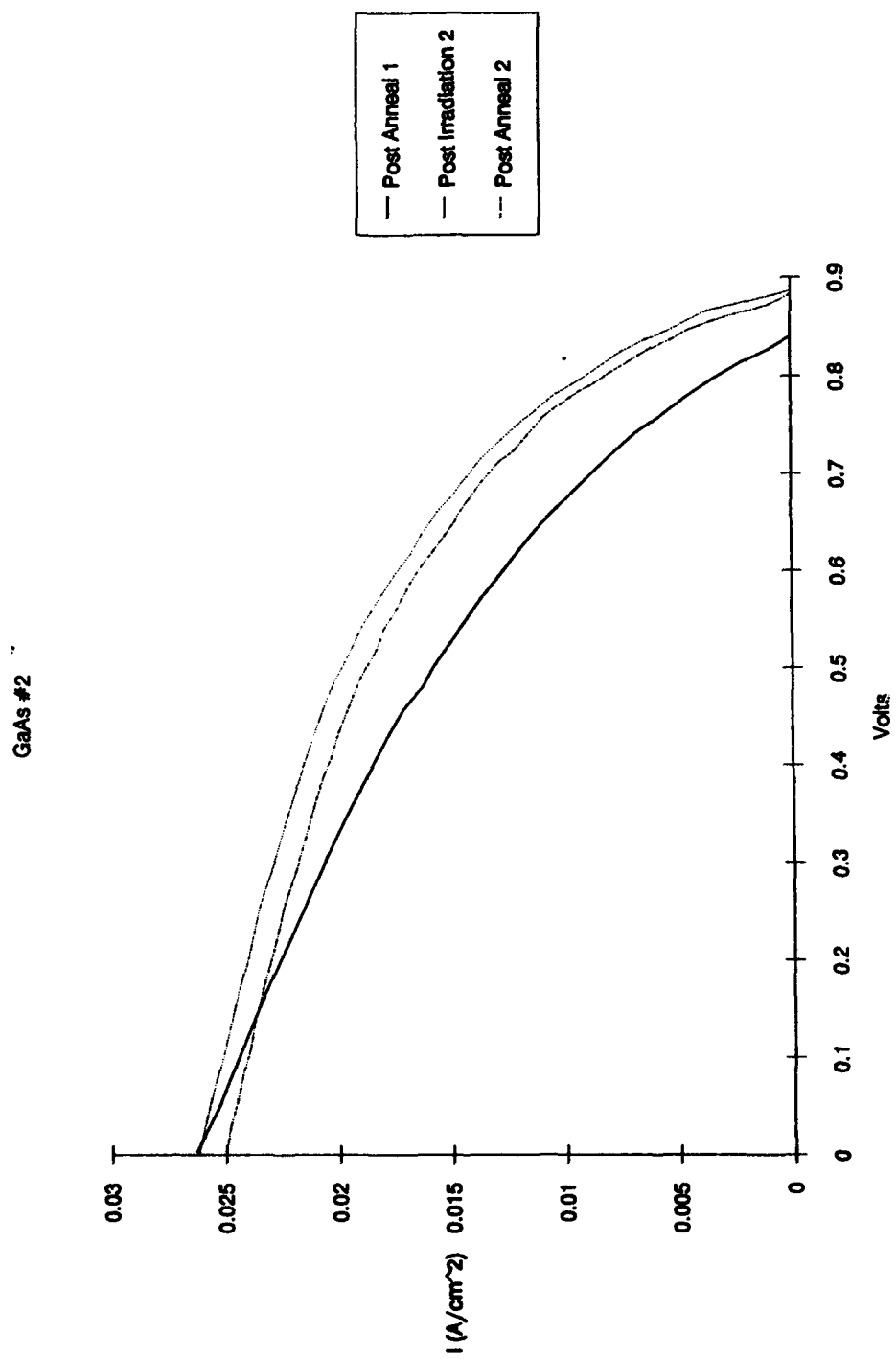


Figure B.2. I-V curves for GaAs cell No. 2

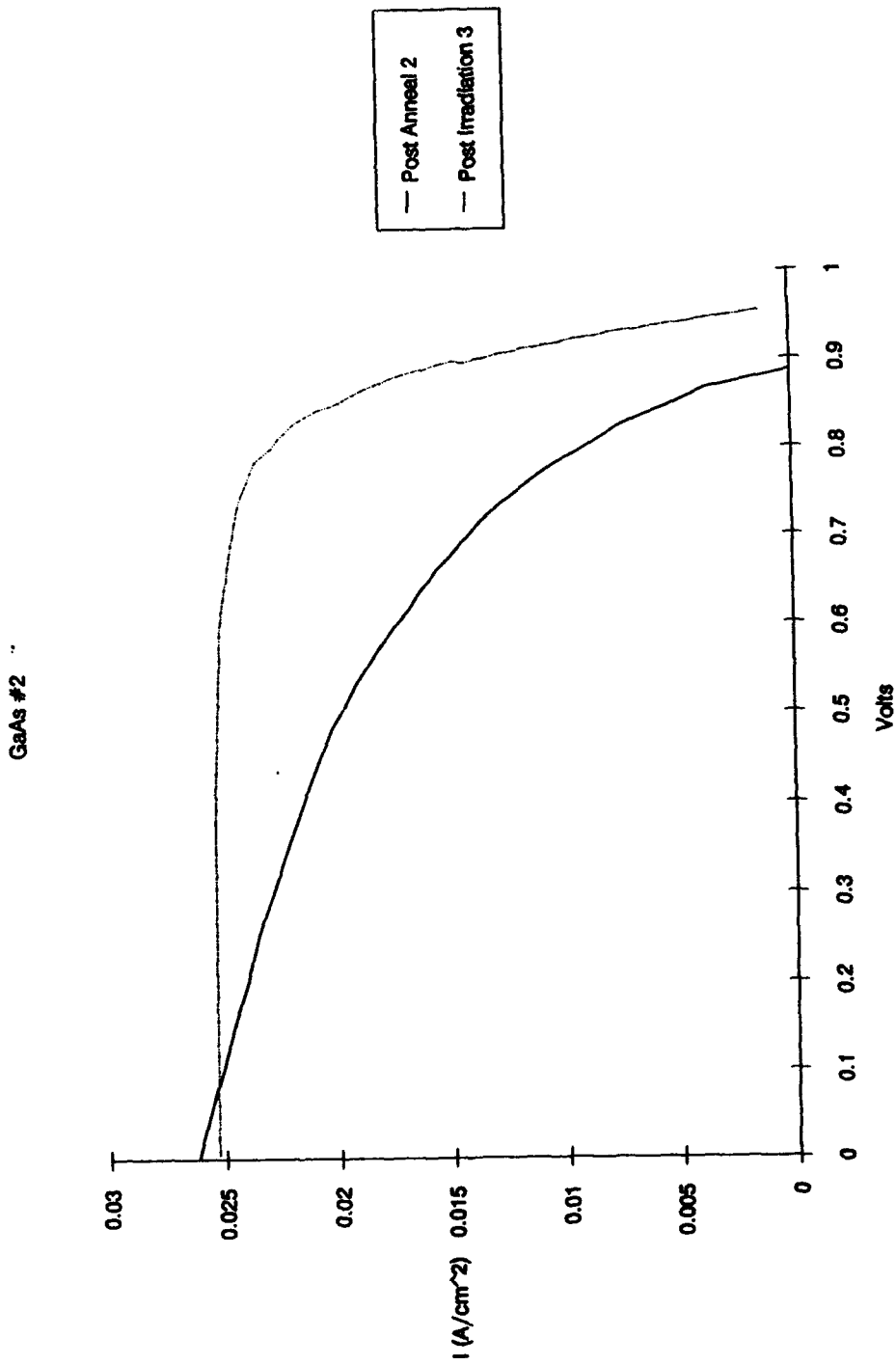


Figure B.3. I-V curves for GaAs cell No. 2

GaAs #6

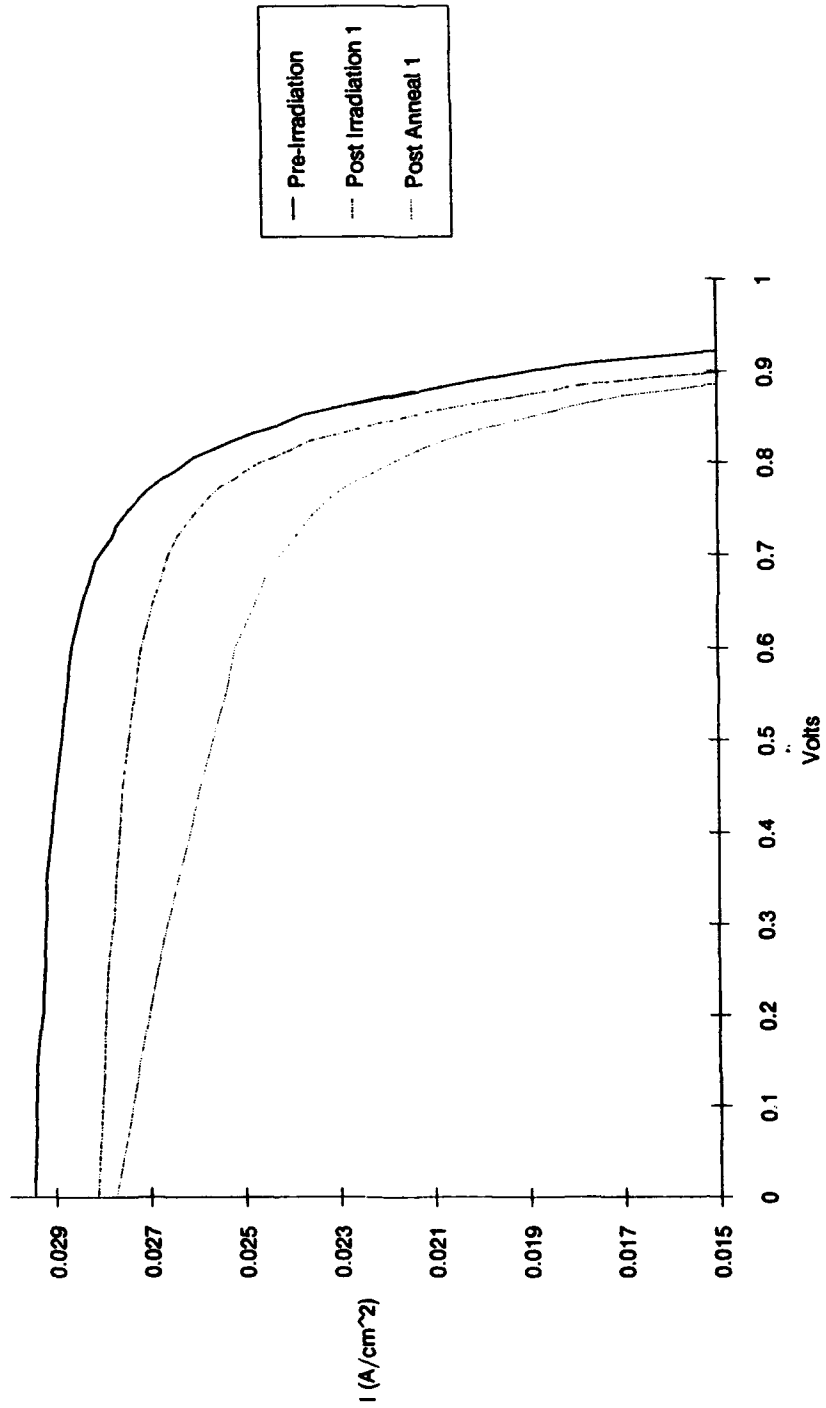


Figure B.4. I-V curves for GaAs cell No. 6



GaAs #6

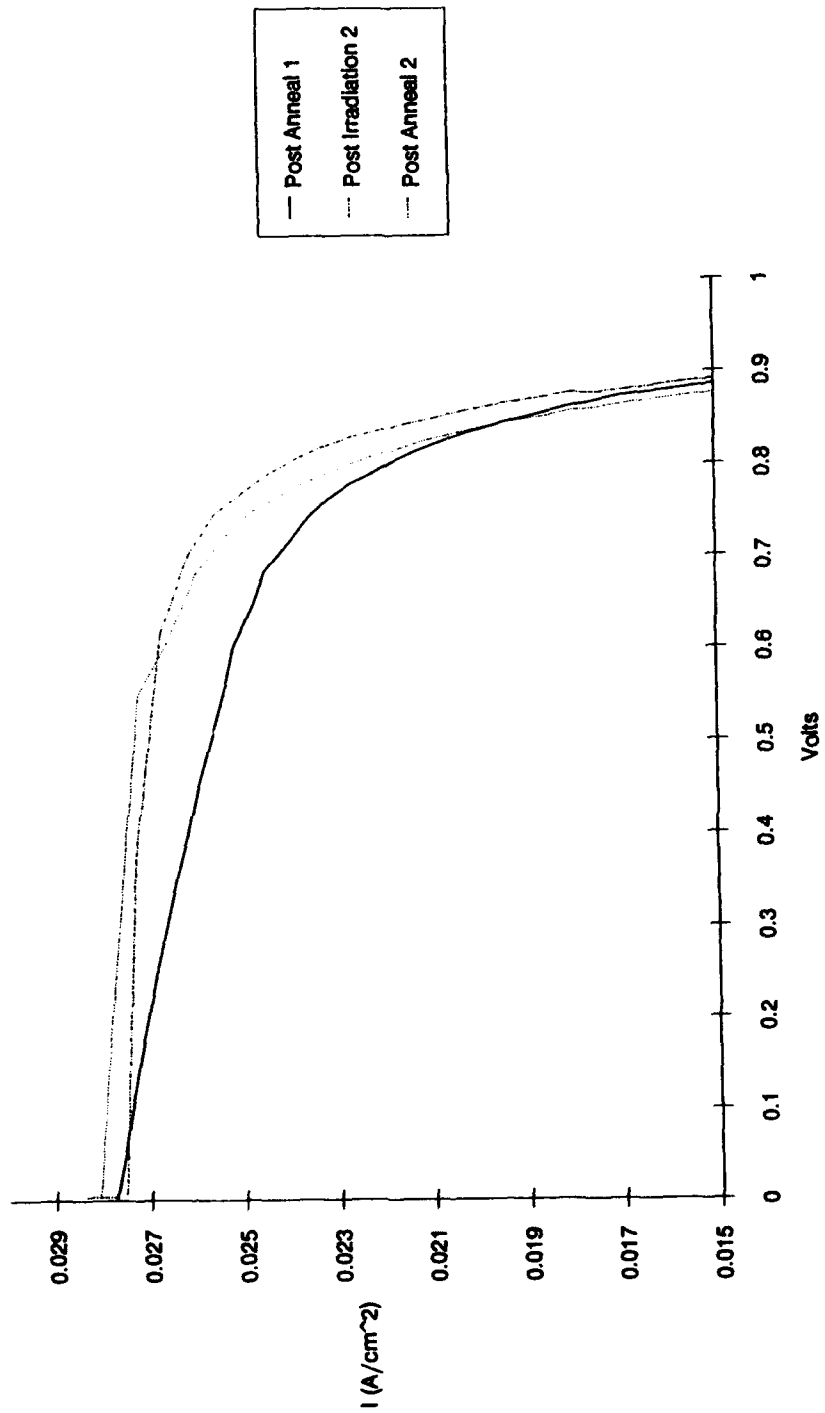


Figure B.5. I-V curves for GaAs cell No. 6

GaAs #6

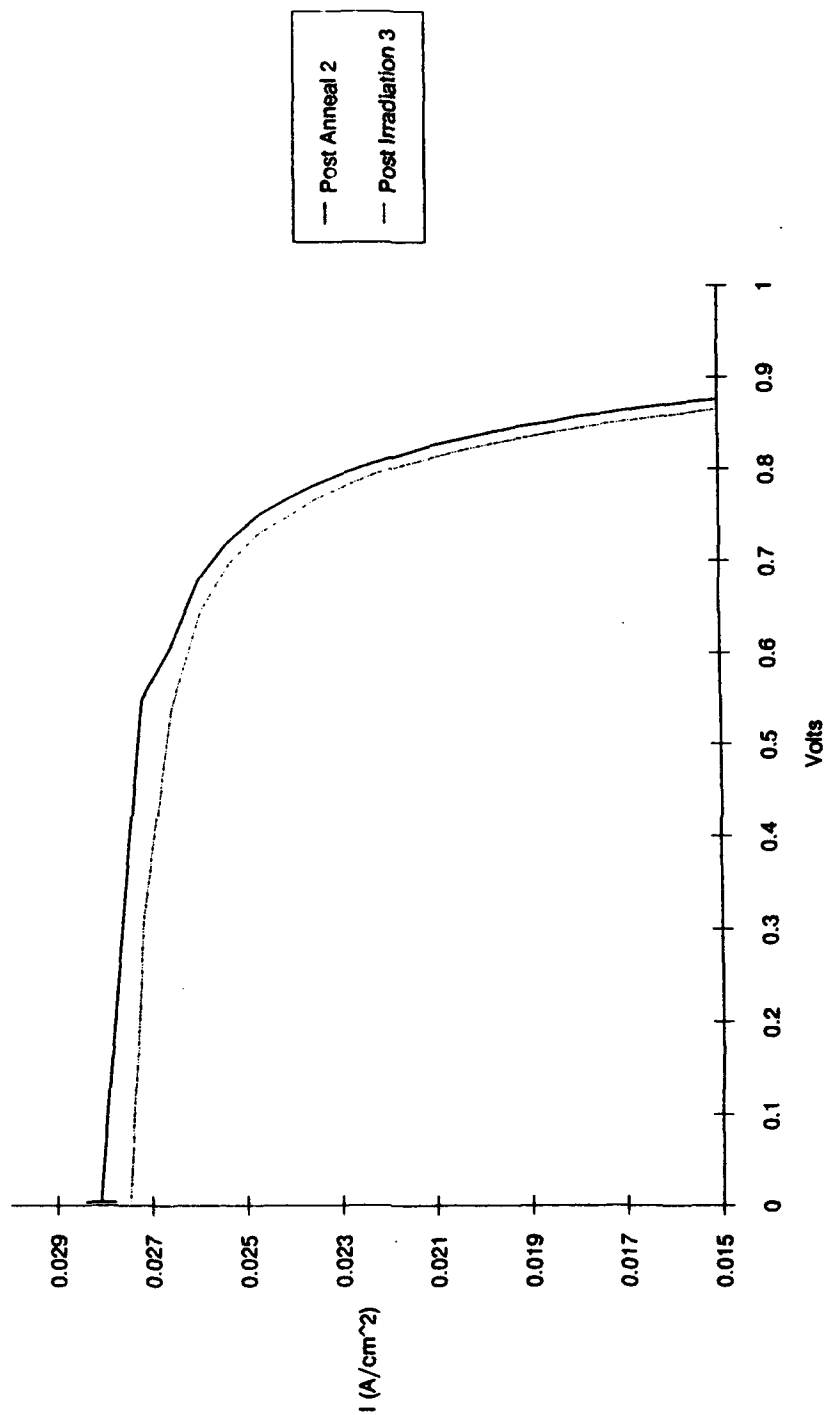


Figure B.6. I-V curves for GaAs cell No. 6

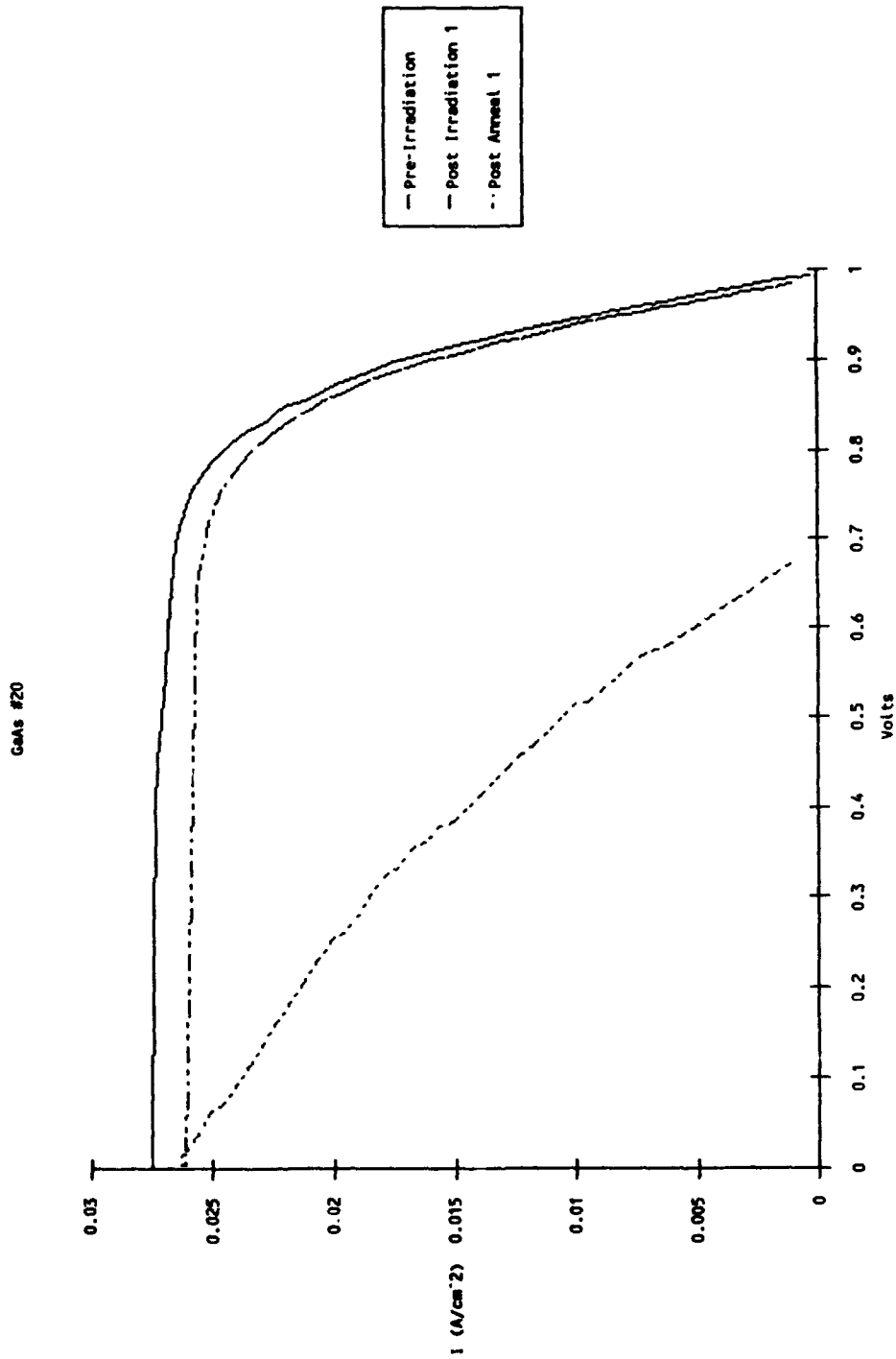


Figure B.7. I-V curves for GaAs cell No. 20

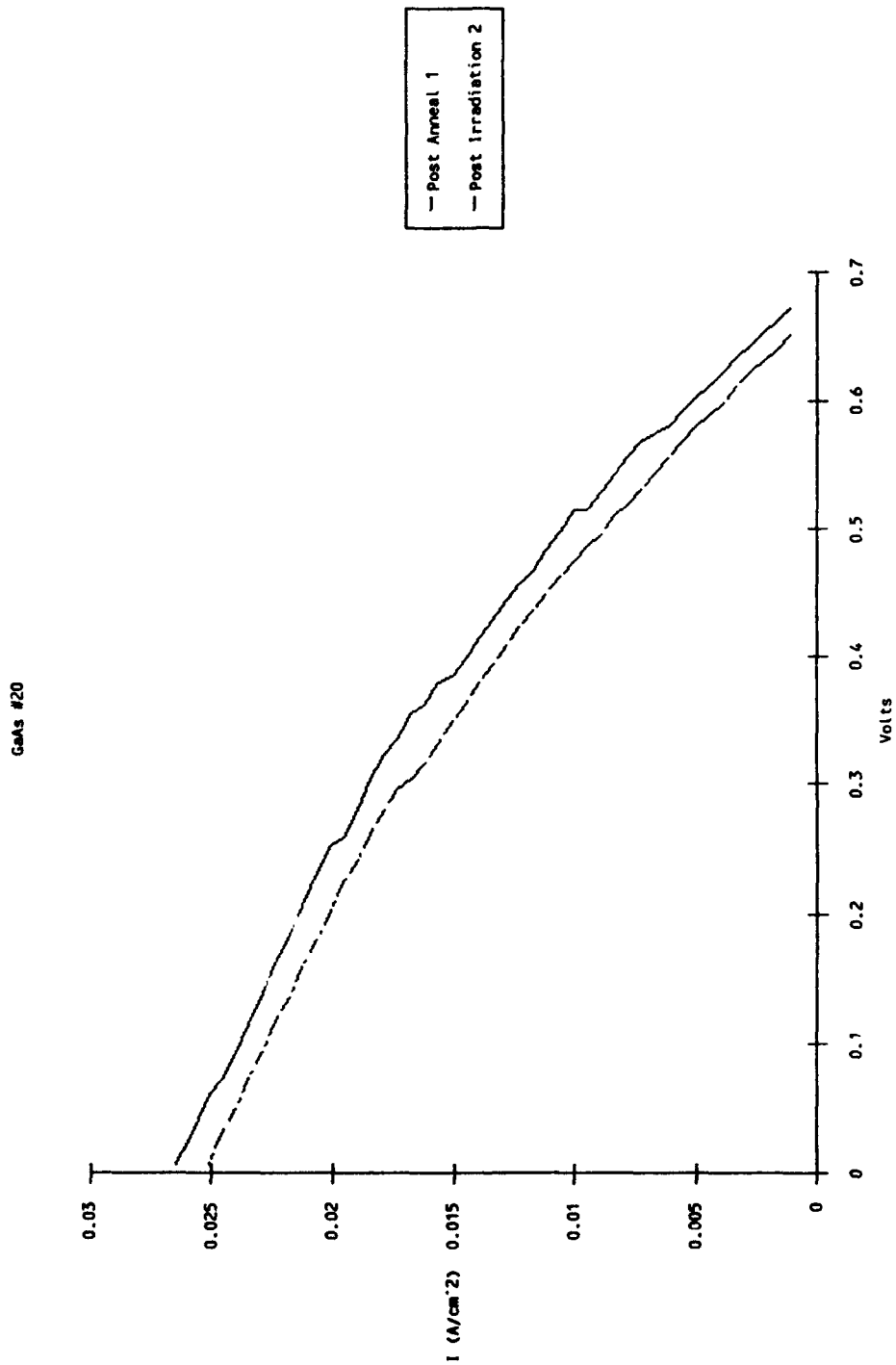


Figure B.8. I-V curves for GaAs cell No. 20

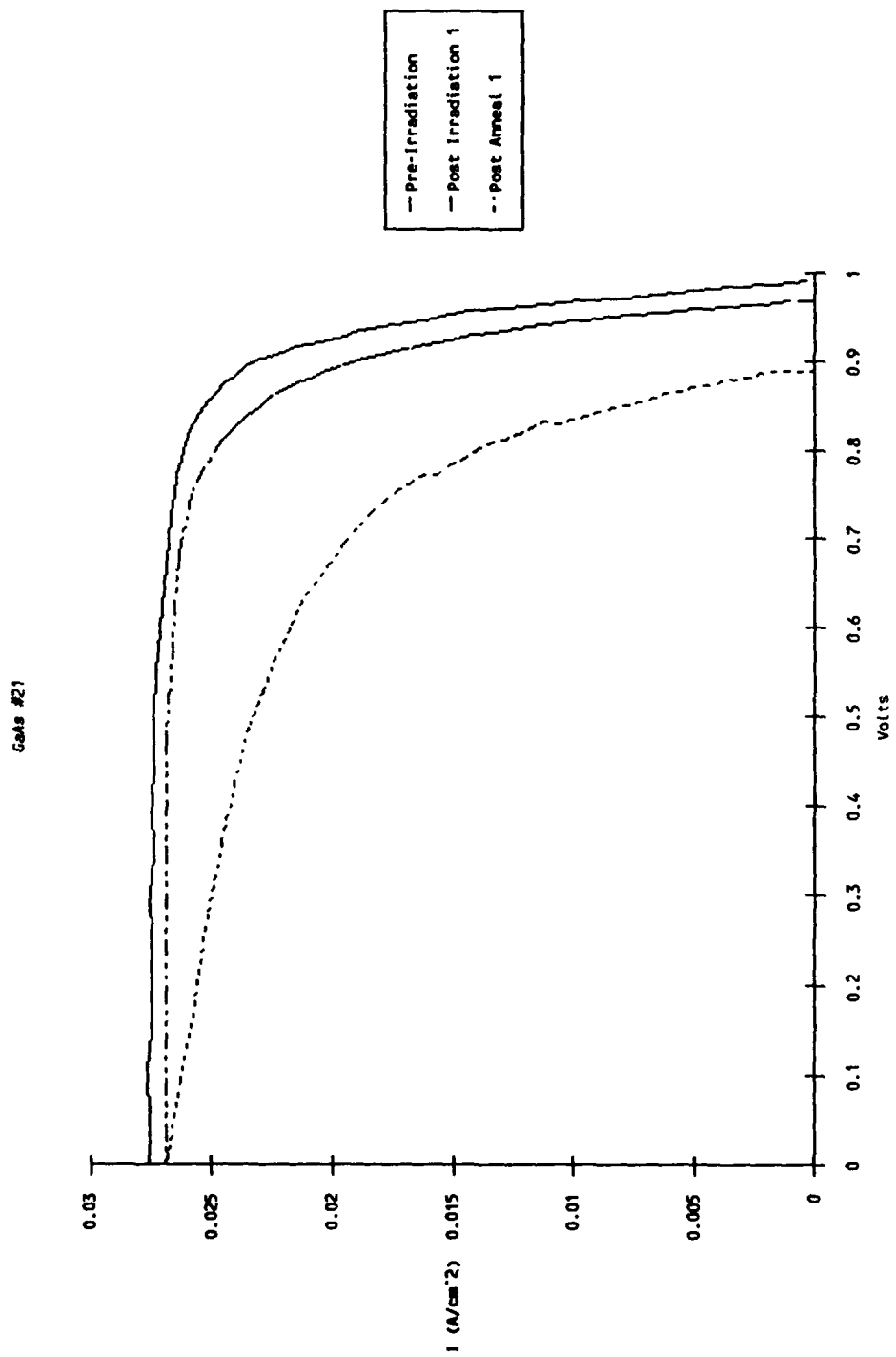


Figure B.9. I-V curves for GaAs cell No. 21

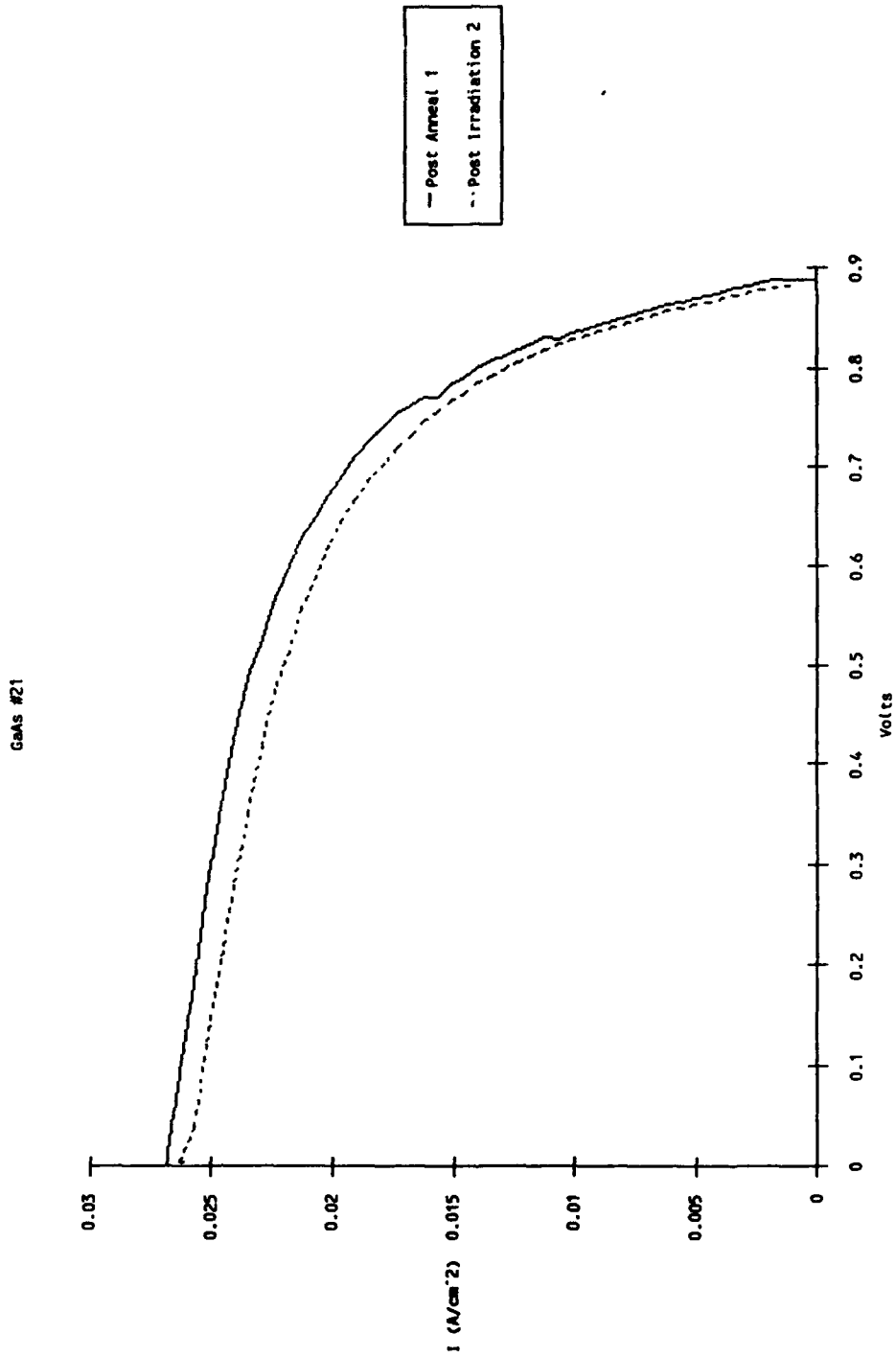


Figure B.10. I-V curves for GaAs cell No. 21

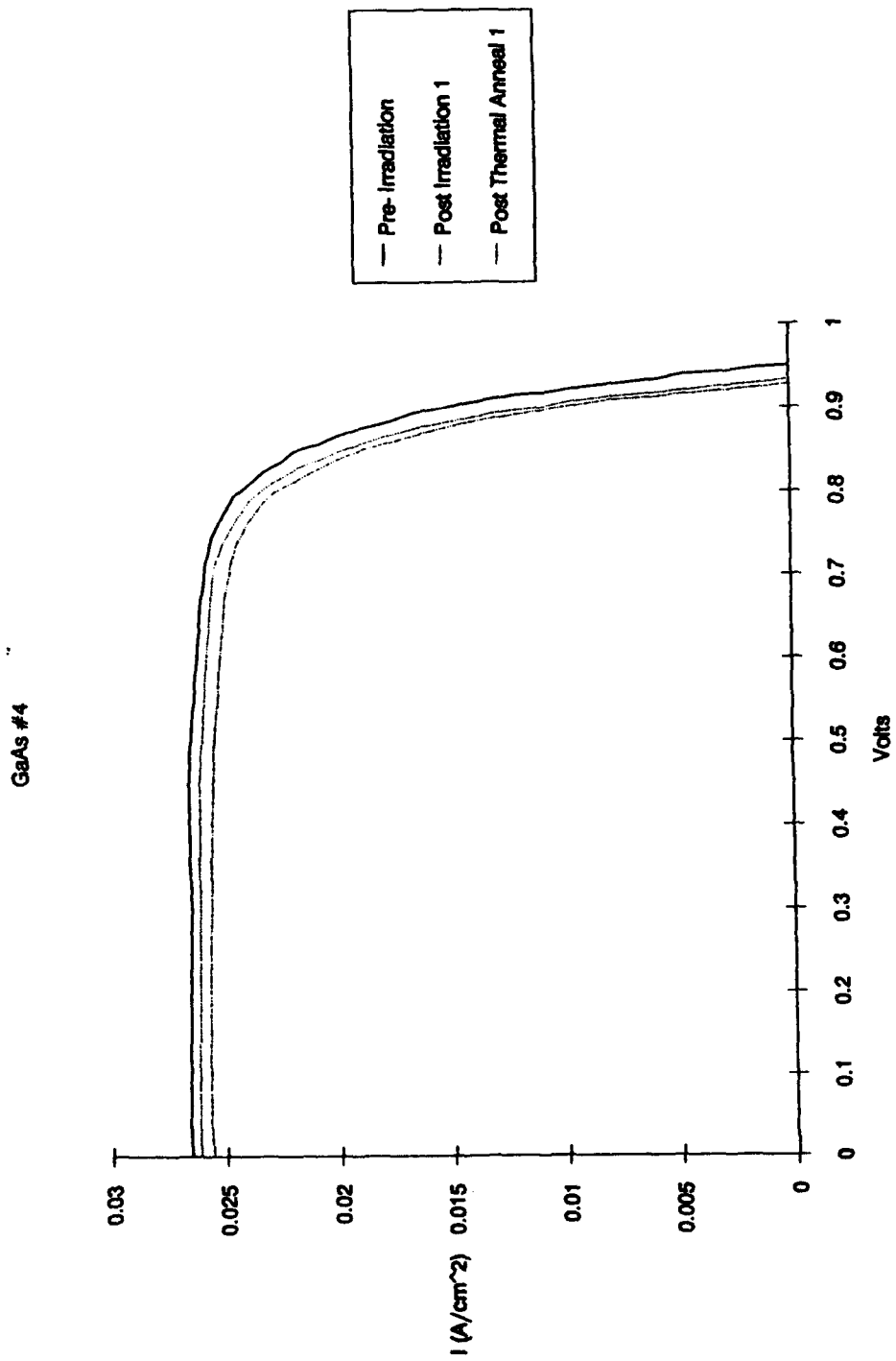


Figure B.11. I-V curves for GaAs cell No.4

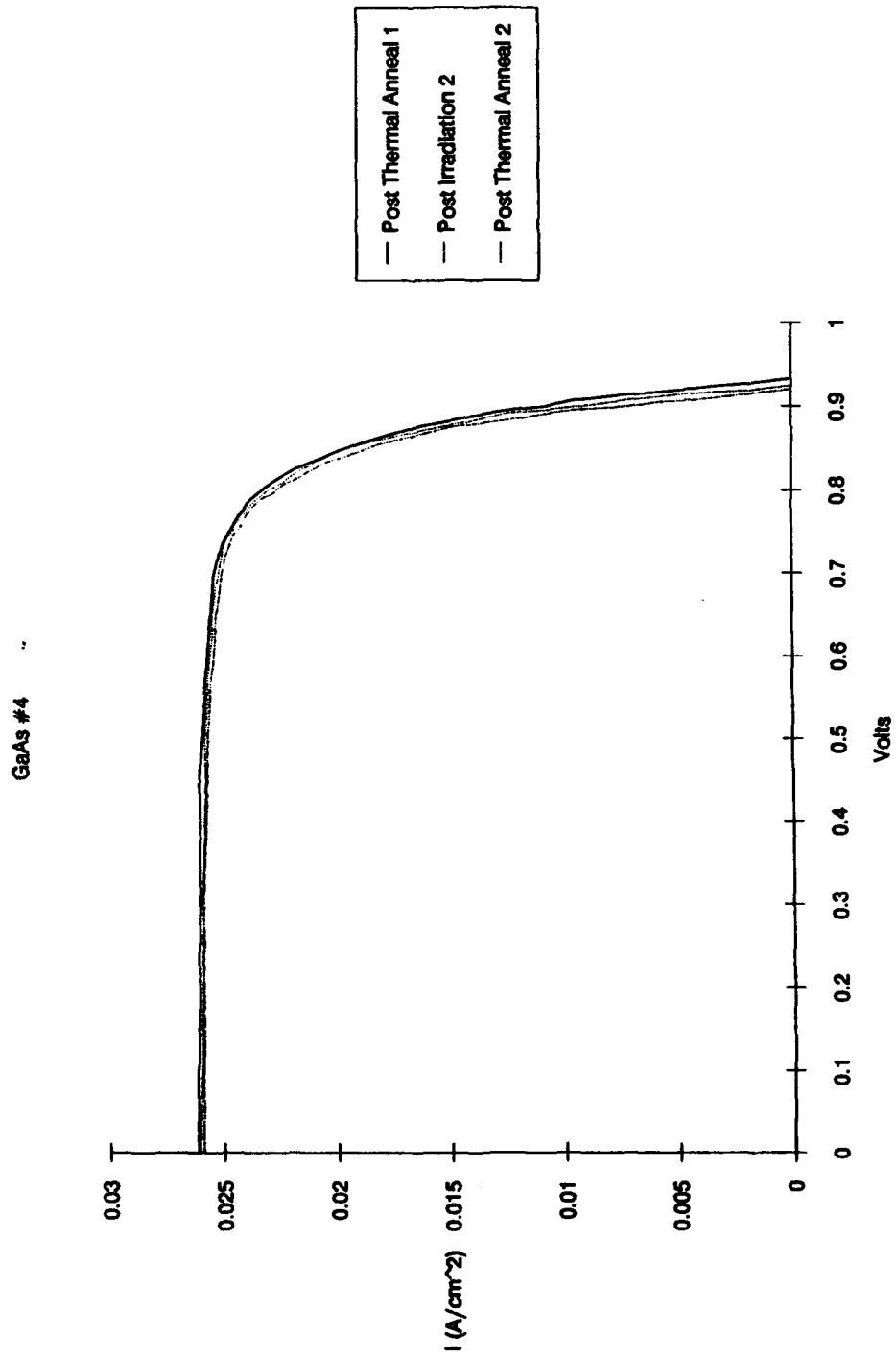


Figure B.12. I-V curves for GaAs cell No. 4



GaAs #4

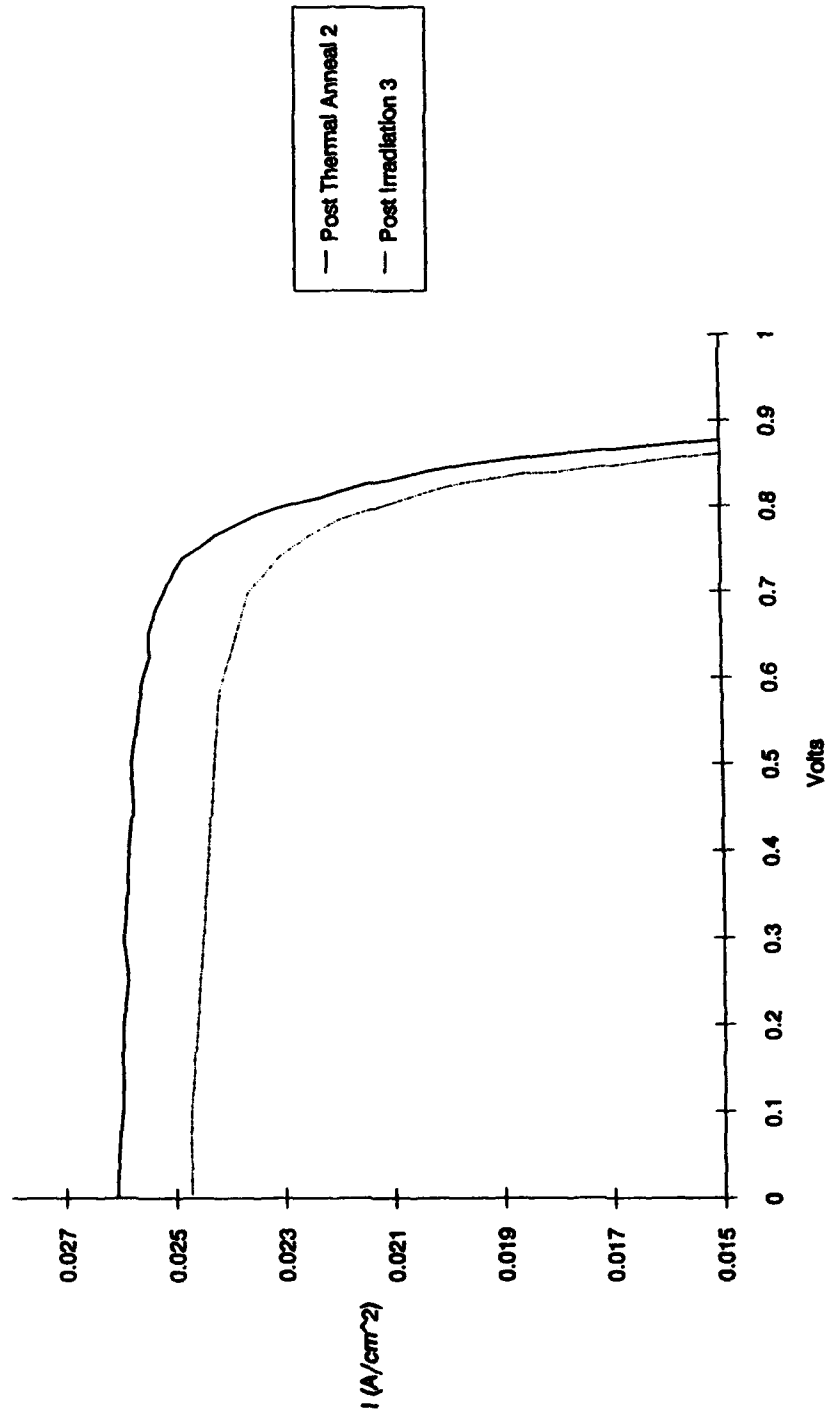


Figure B.13. I-V curves for GaAs cell No. 4

GaAs #5

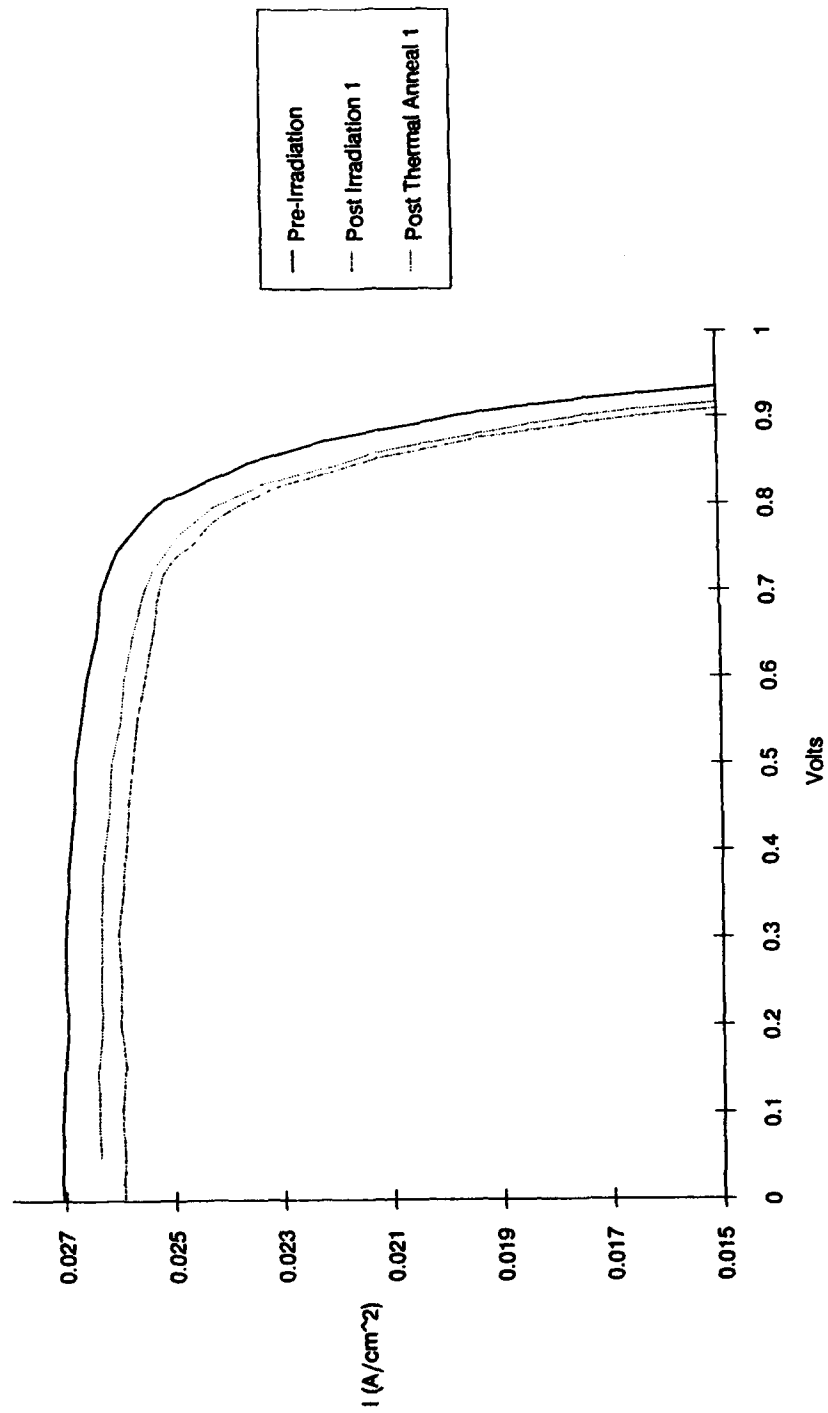


Figure B.14. I-V curves for GaAs cell No. 5

GaAs #5

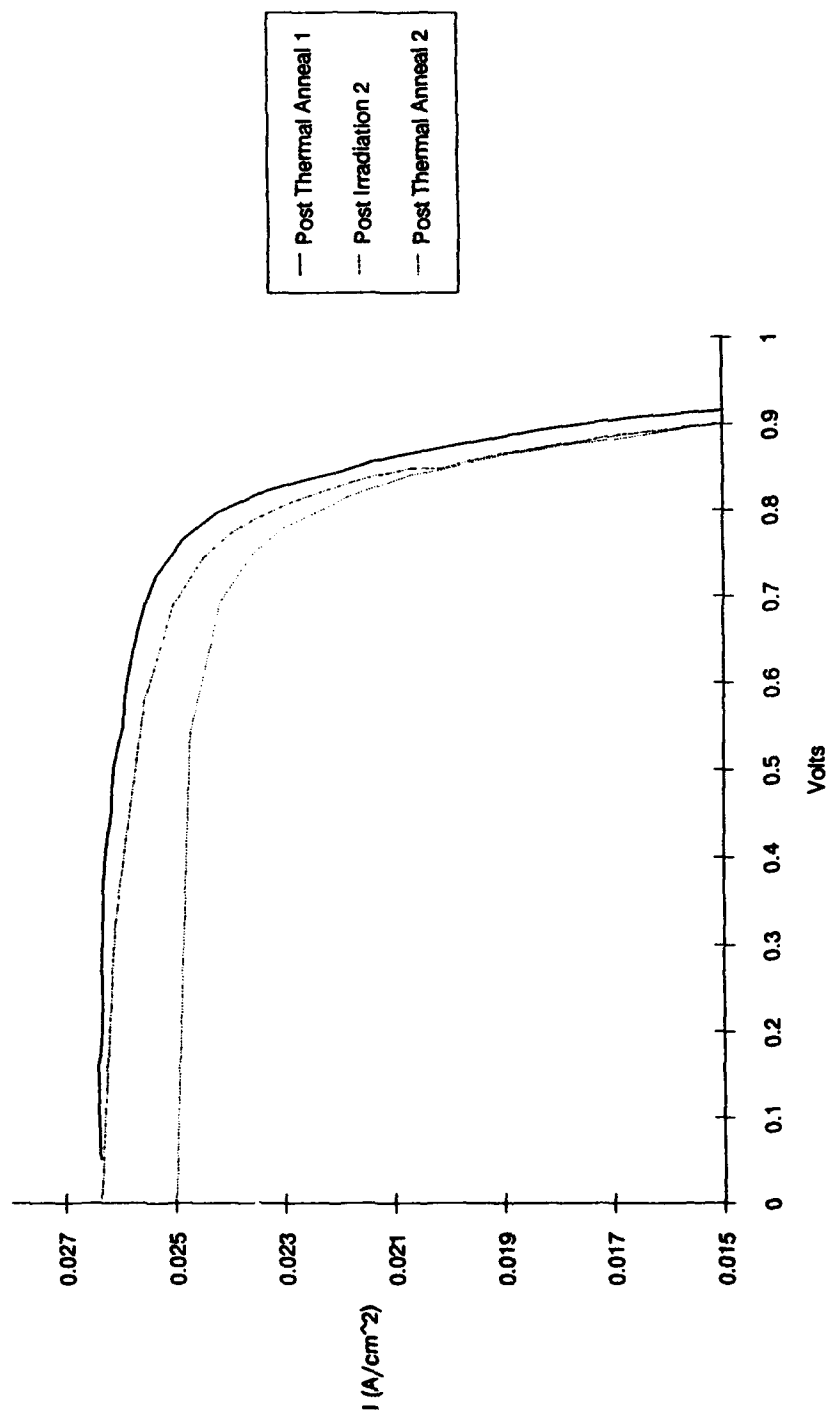


Figure B.15. I-V curves for GaAs cell No. 5

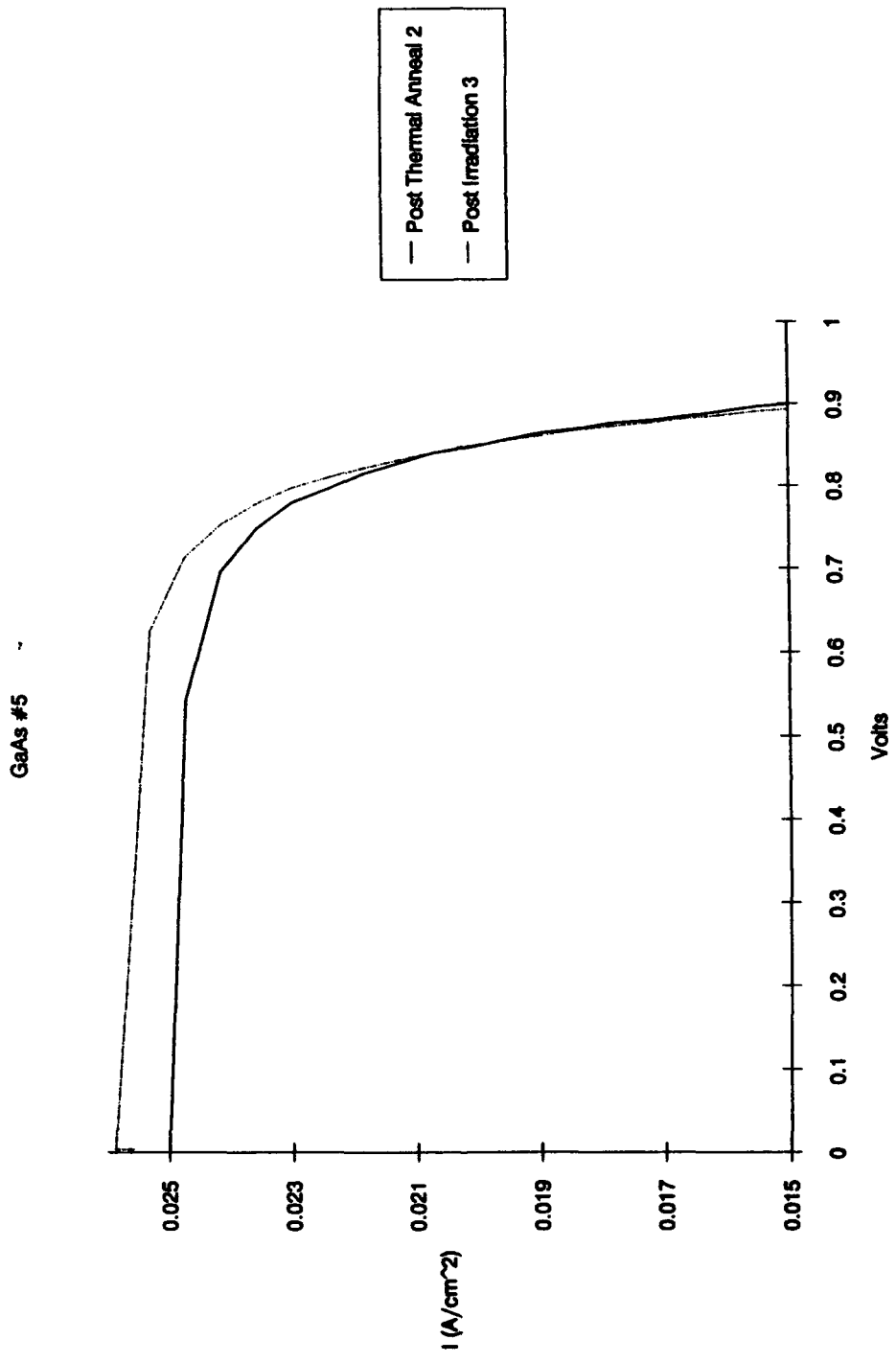


Figure B.16. I-V curves for GaAs cell No. 5

GaAs #8

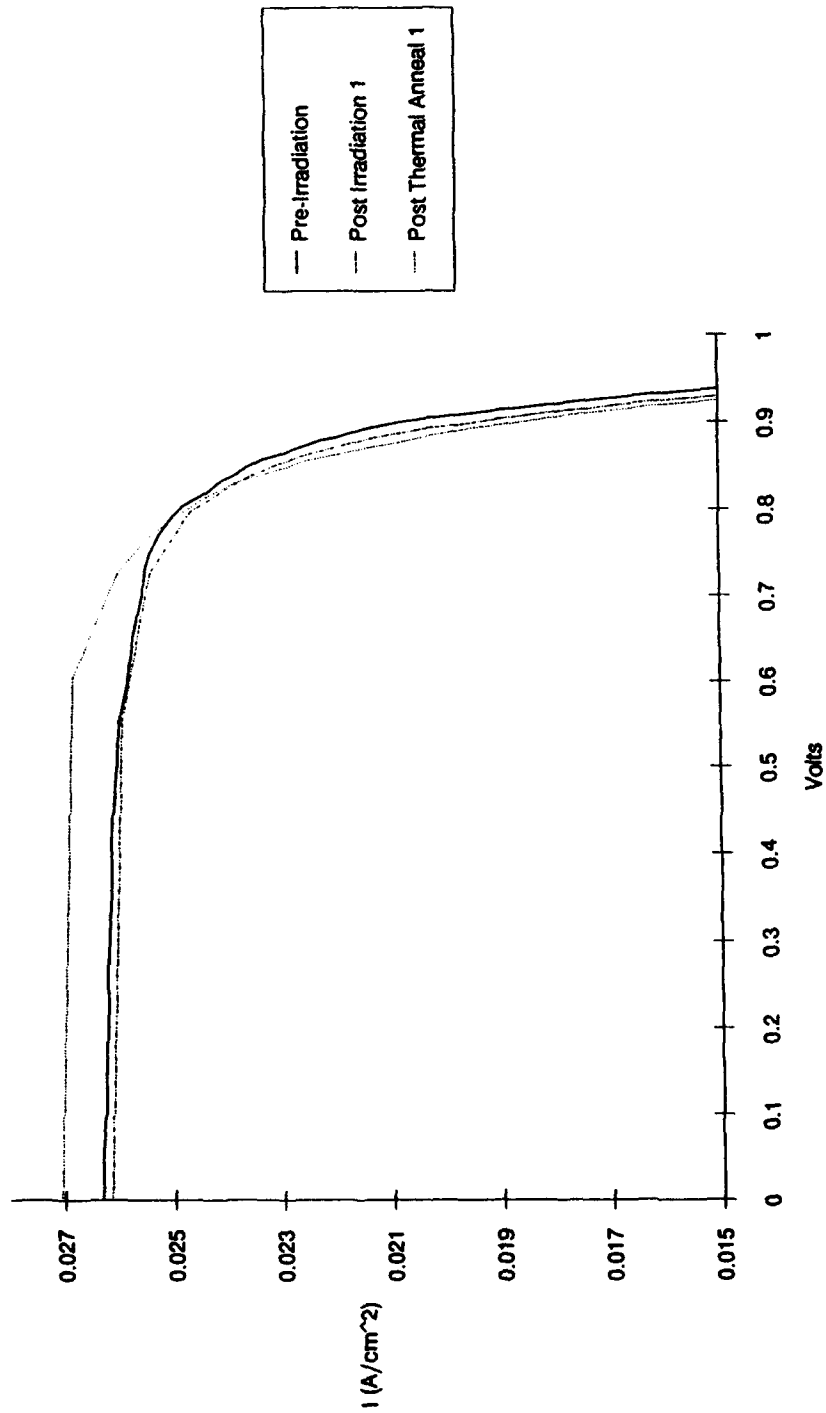


Figure B.17. I-V curves for GaAs cell No. 8

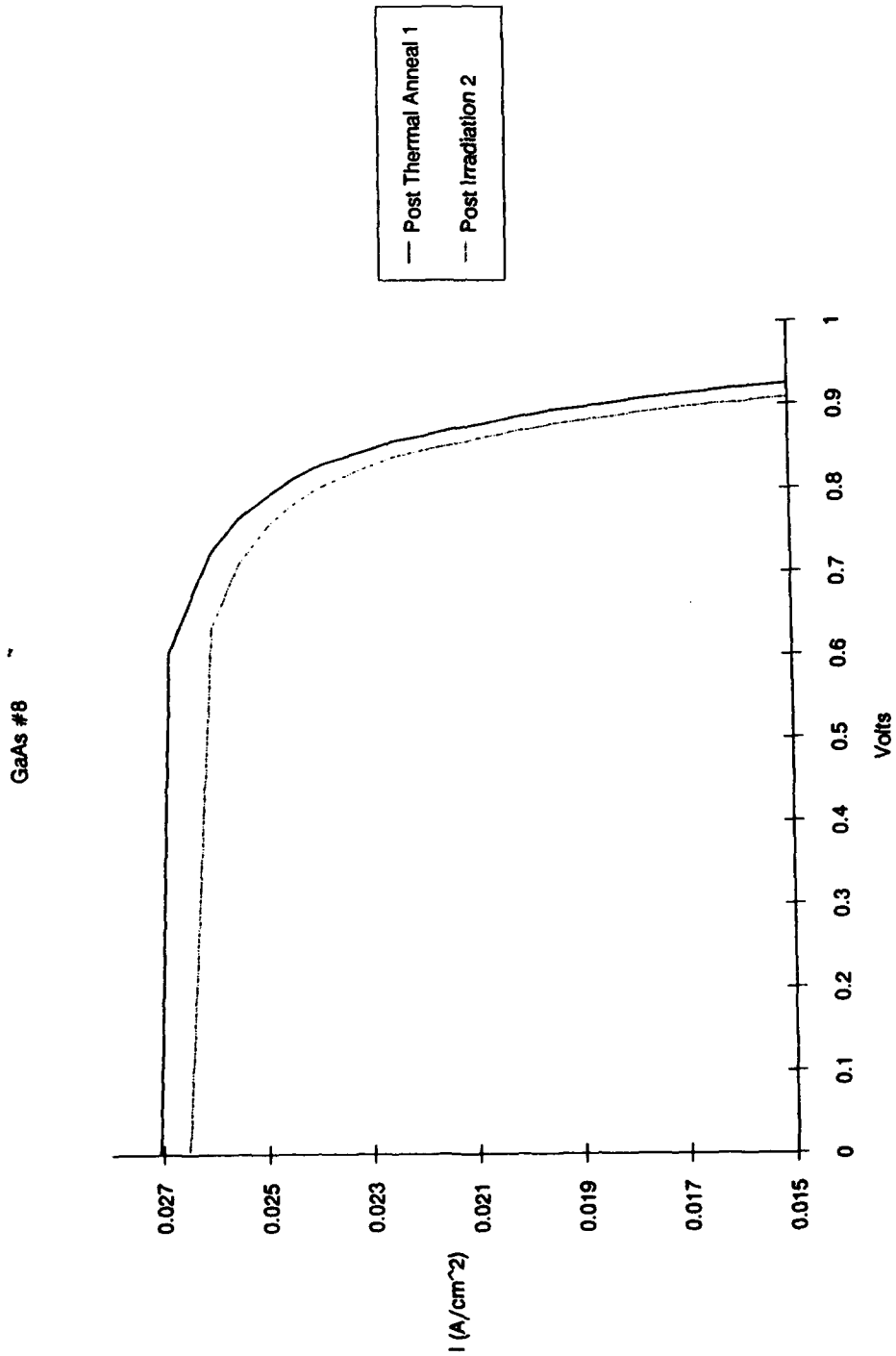


Figure B.18. I-V curves for GaAs cell No. 8

APPENDIX C  
OPEN CIRCUIT VOLTAGE, SHORT CIRCUIT CURRENT AND  
MAXIMUM, POWER NORMALIZED PLOTS FOR GaAs SOLAR CELLS

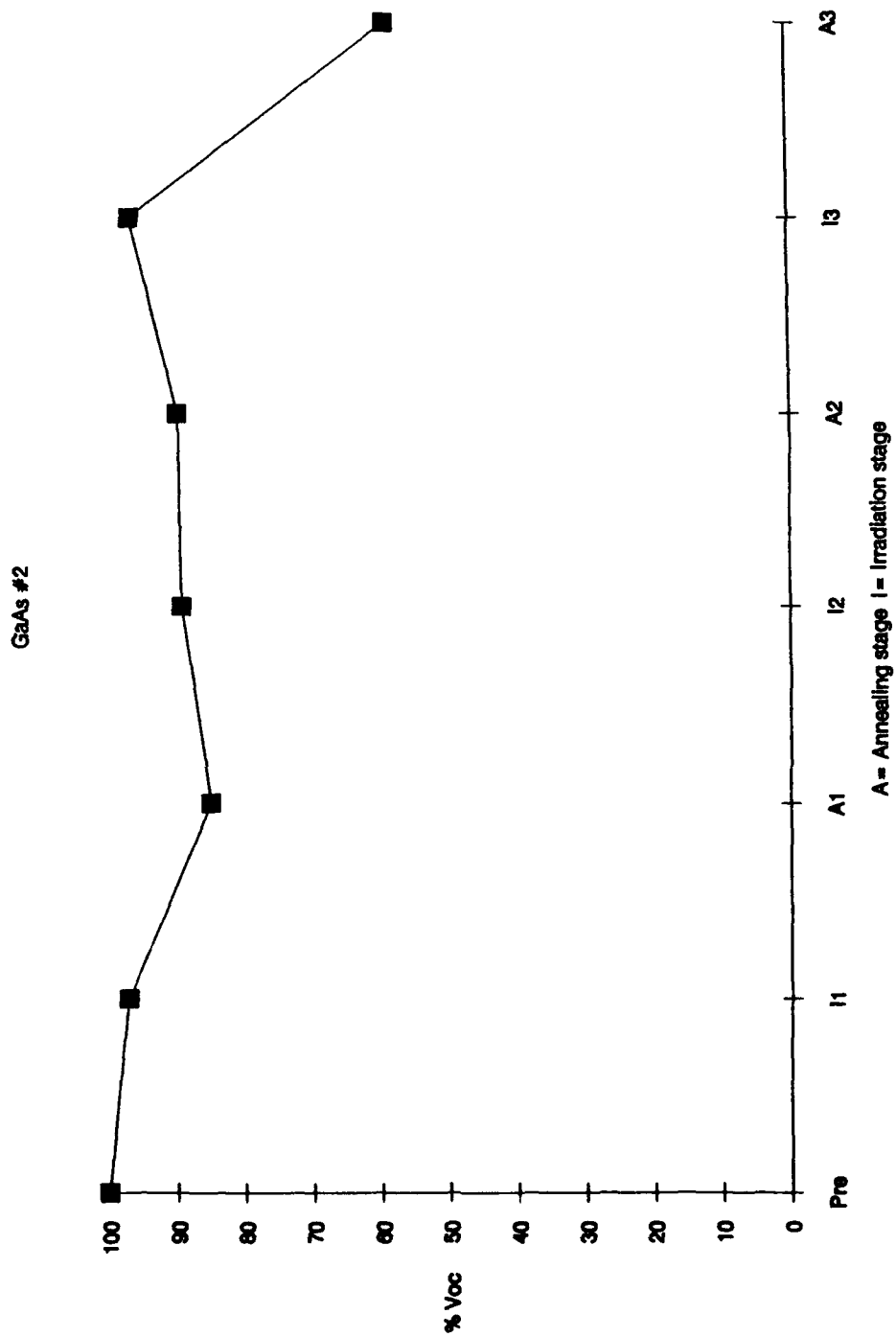


Figure C.1. Normalized  $V_{oc}$  plot for GaAs cell No. 2



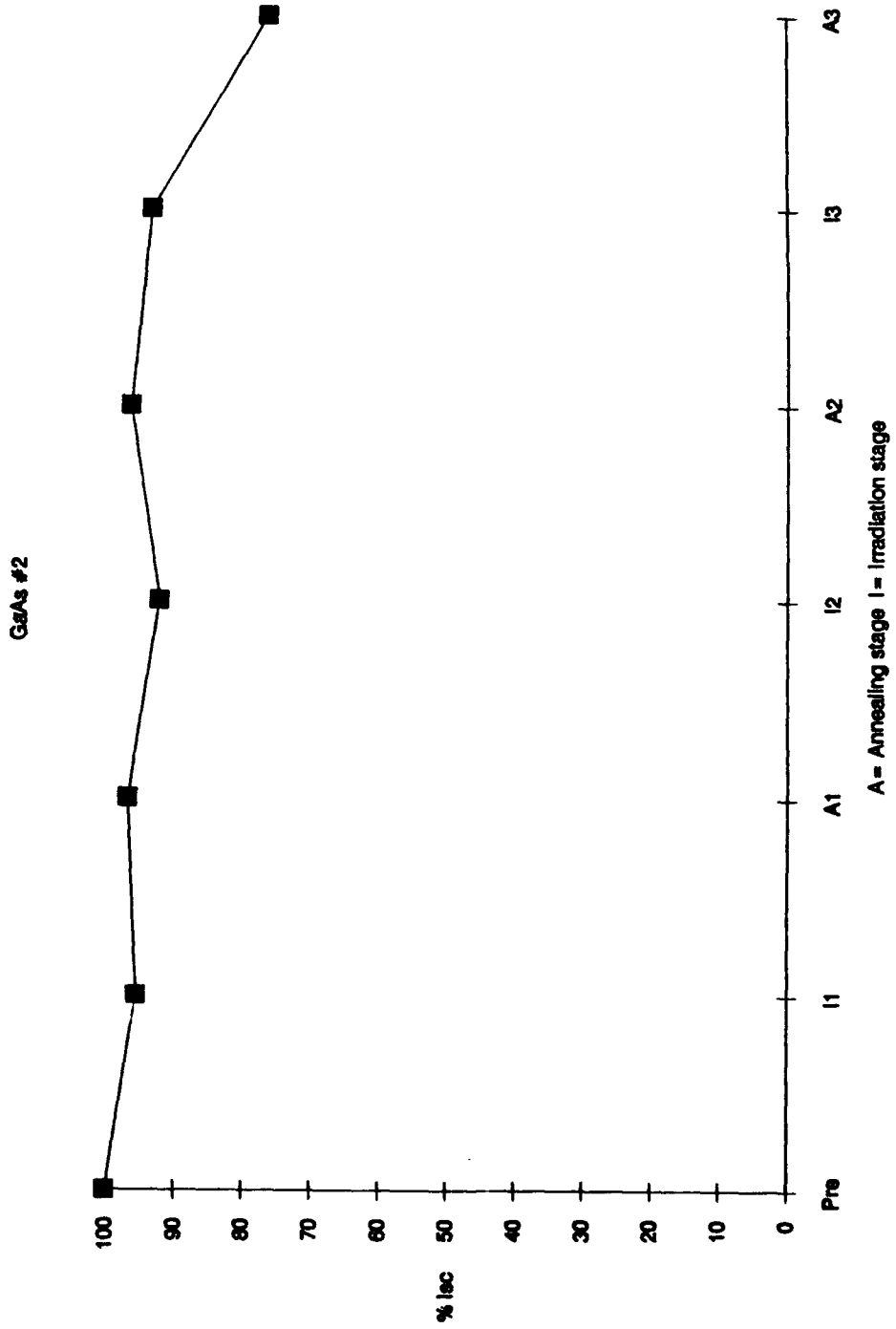


Figure C.2. Normalized  $I_{sc}$  plot for GaAs cell No. 2

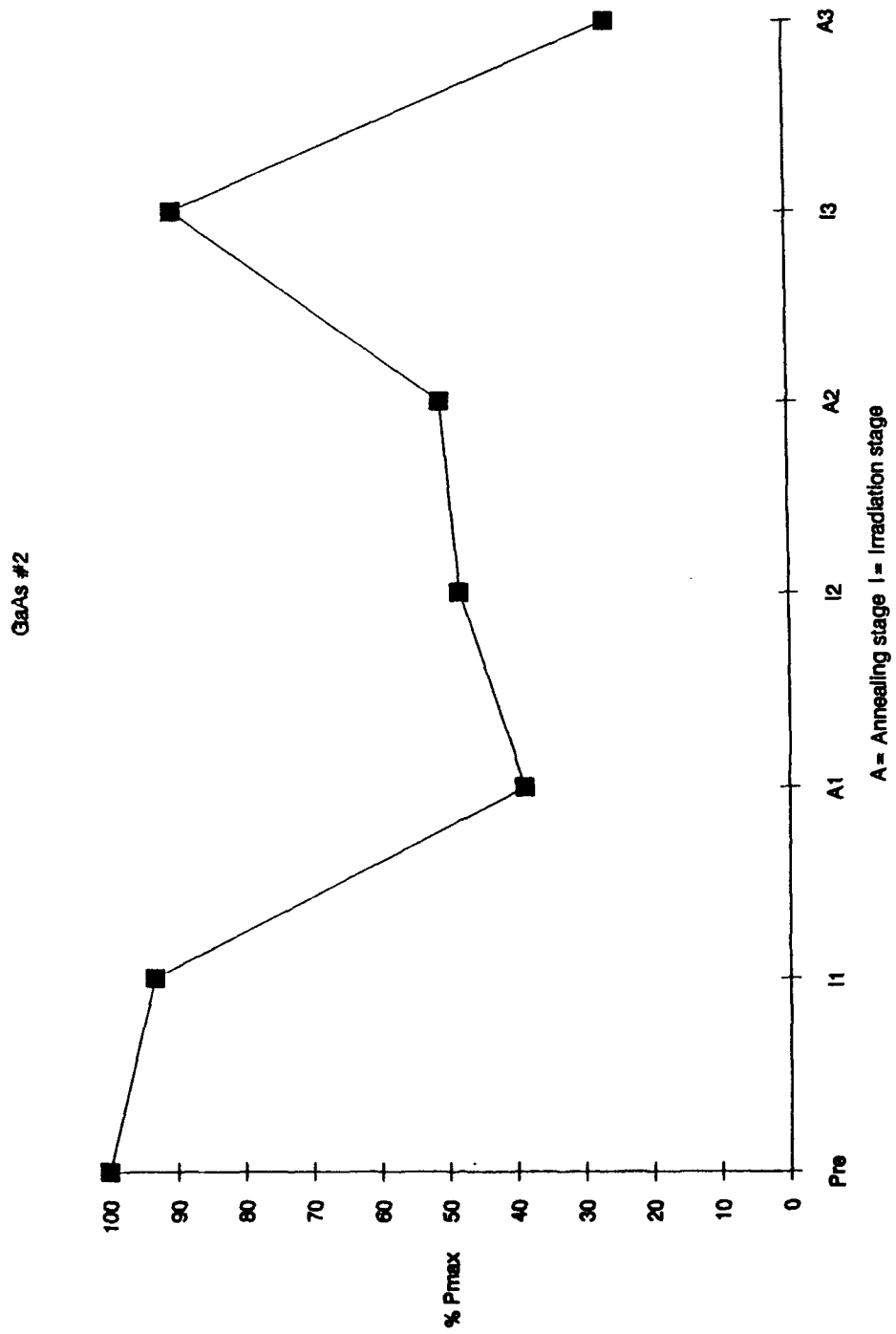


Figure C.3. Normalized  $P_{max}$  plot for GaAs cell No. 2

GaAs #6

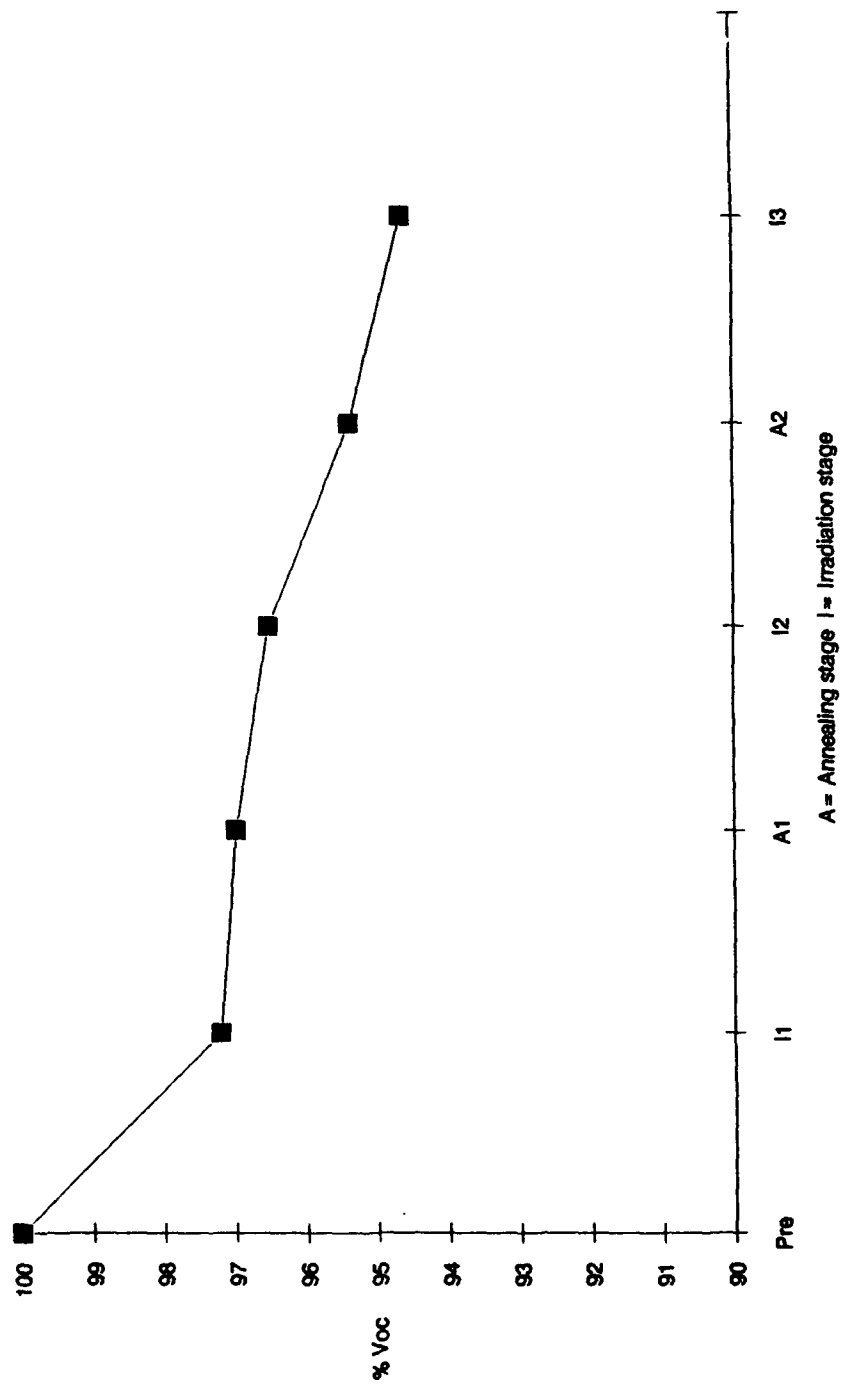


Figure C.4. Normalized  $V_{oc}$  plot for GaAs cell No. 6

GaAs #6

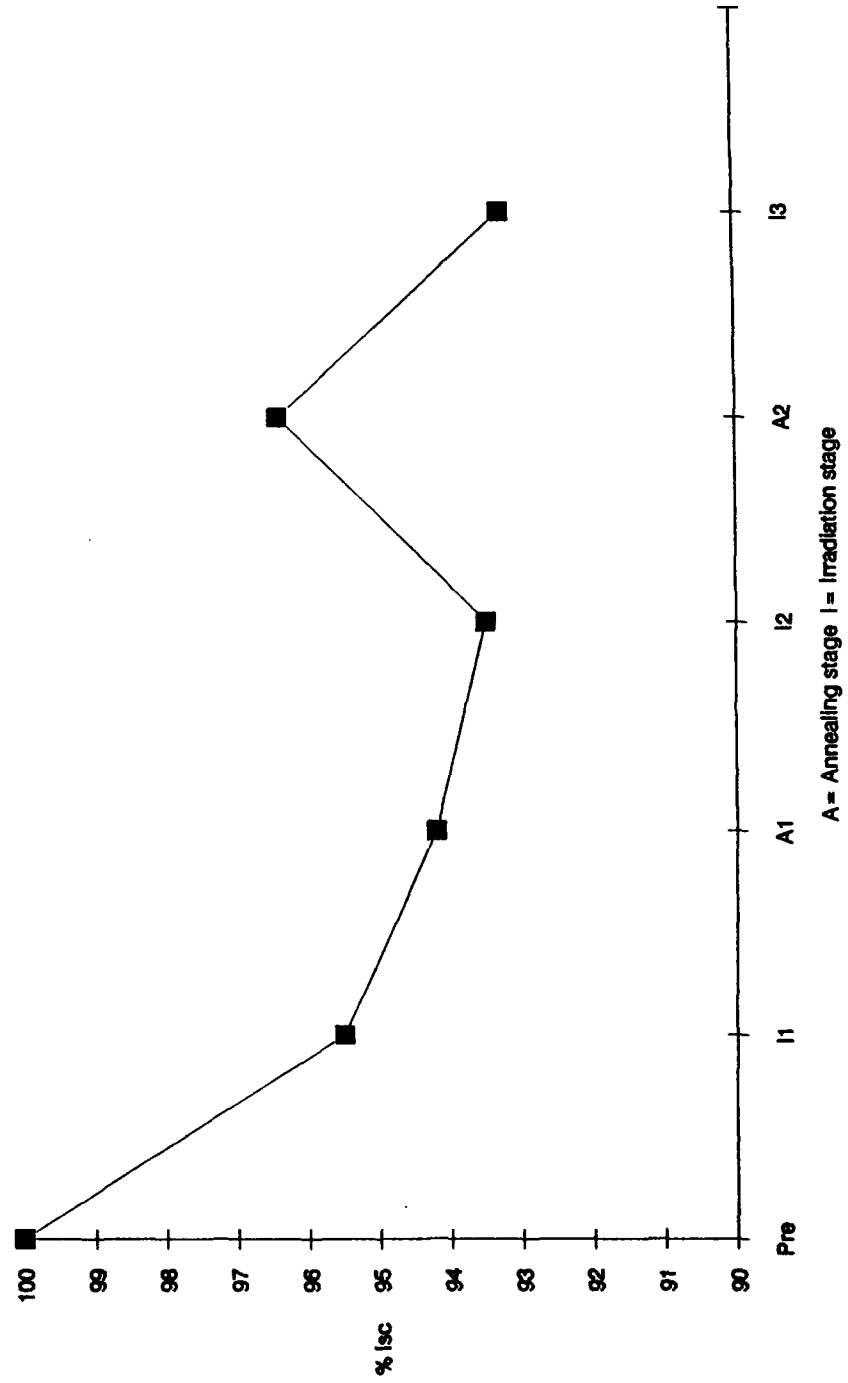


Figure C.5. Normalized  $I_{sc}$  plot for GaAs cell No. 6

GaAs #6

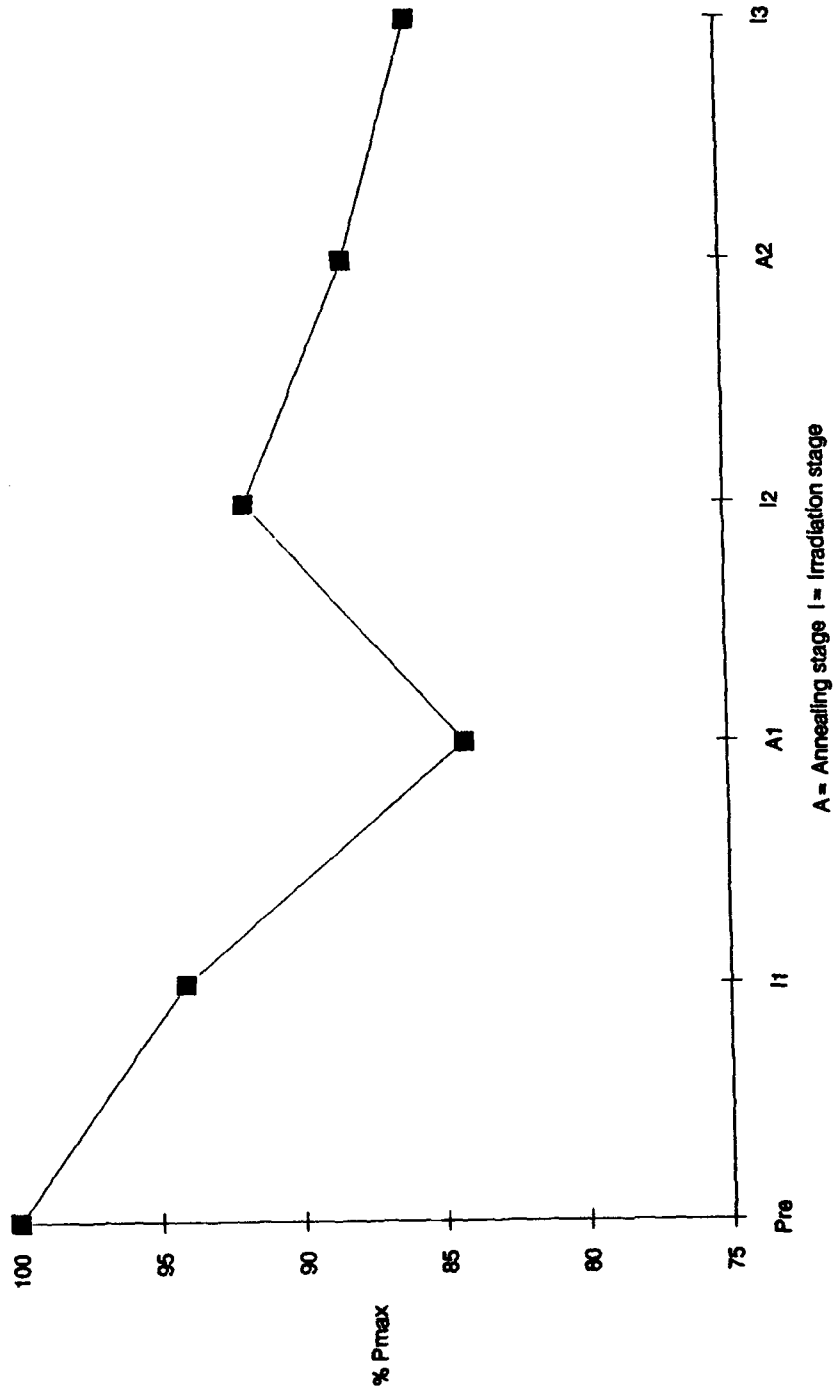
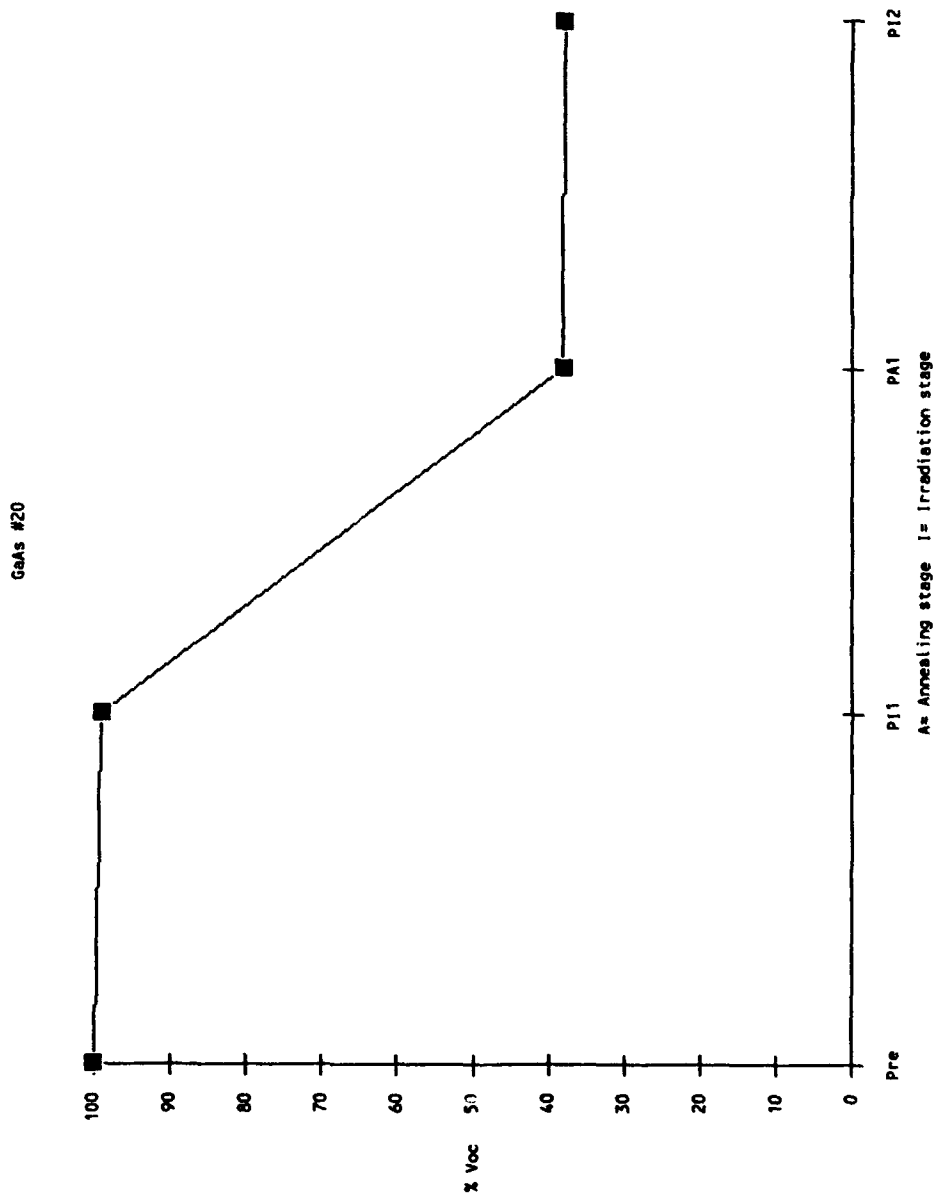


Figure C.6. Normalized  $P_{max}$  plot for GaAs cell No. 6



C.7. Normalized  $V_{OC}$  plot for GaAs cell No. 20

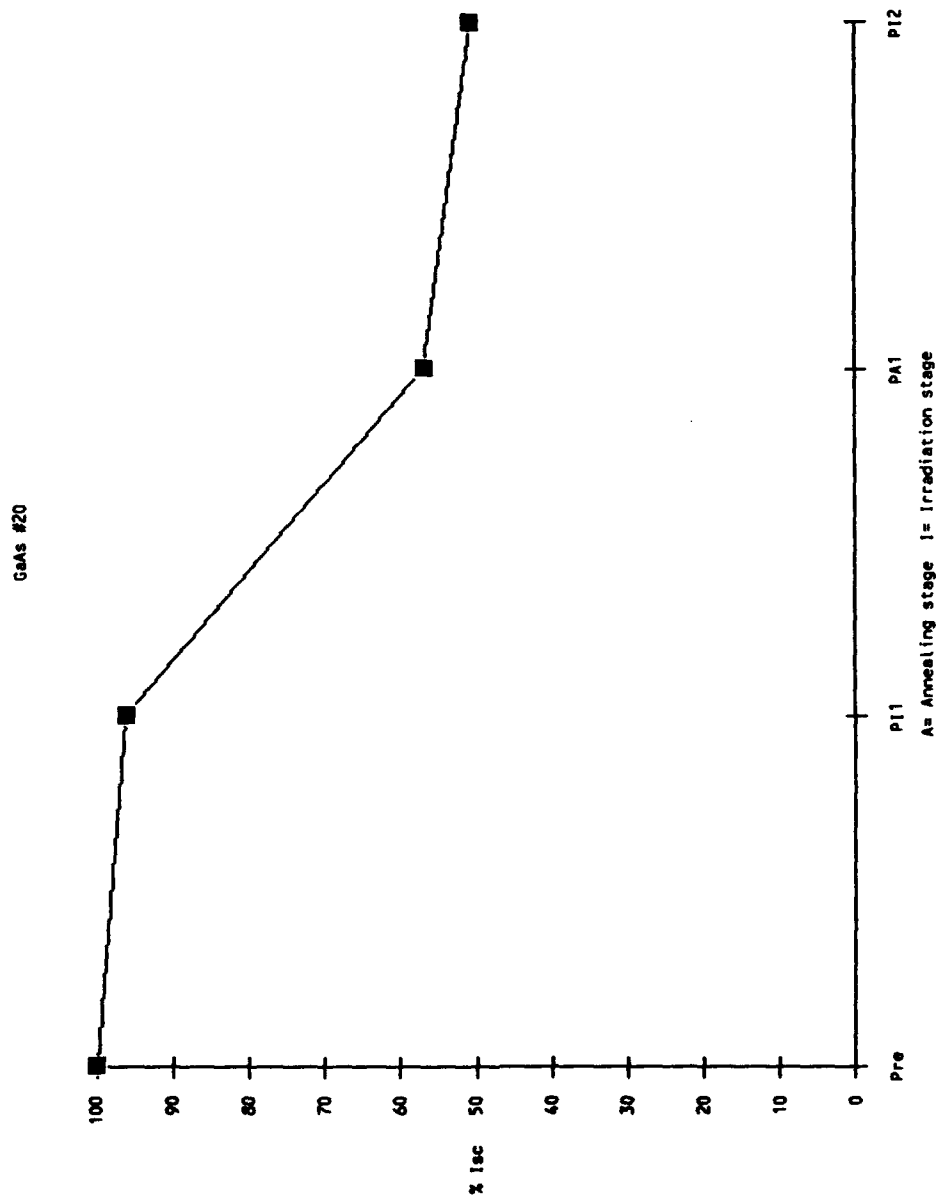


Figure C.8. Normalized  $I_{sc}$  plot for GaAs cell No. 20

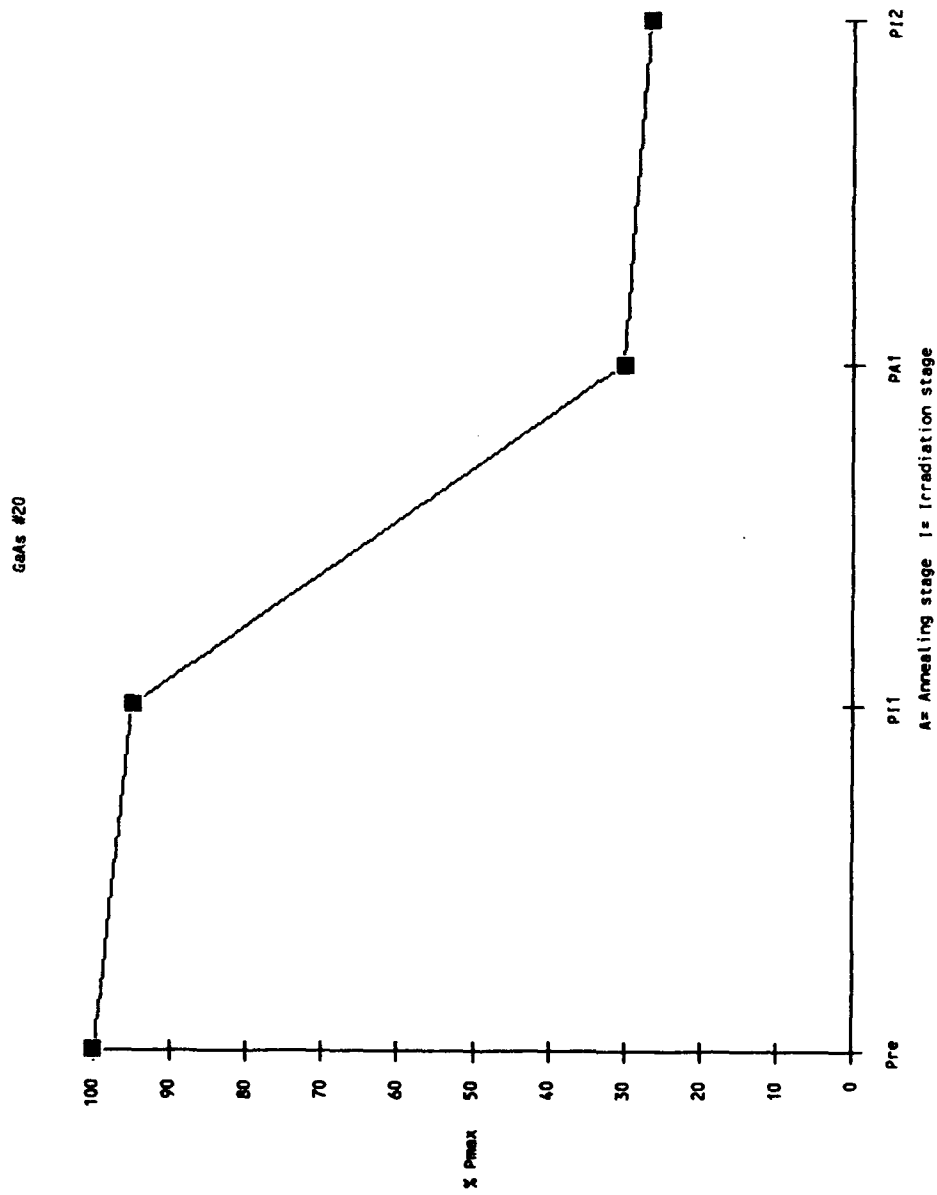


Figure C.9. Normalized  $P_{\max}$  plot for GaAs cell No. 20



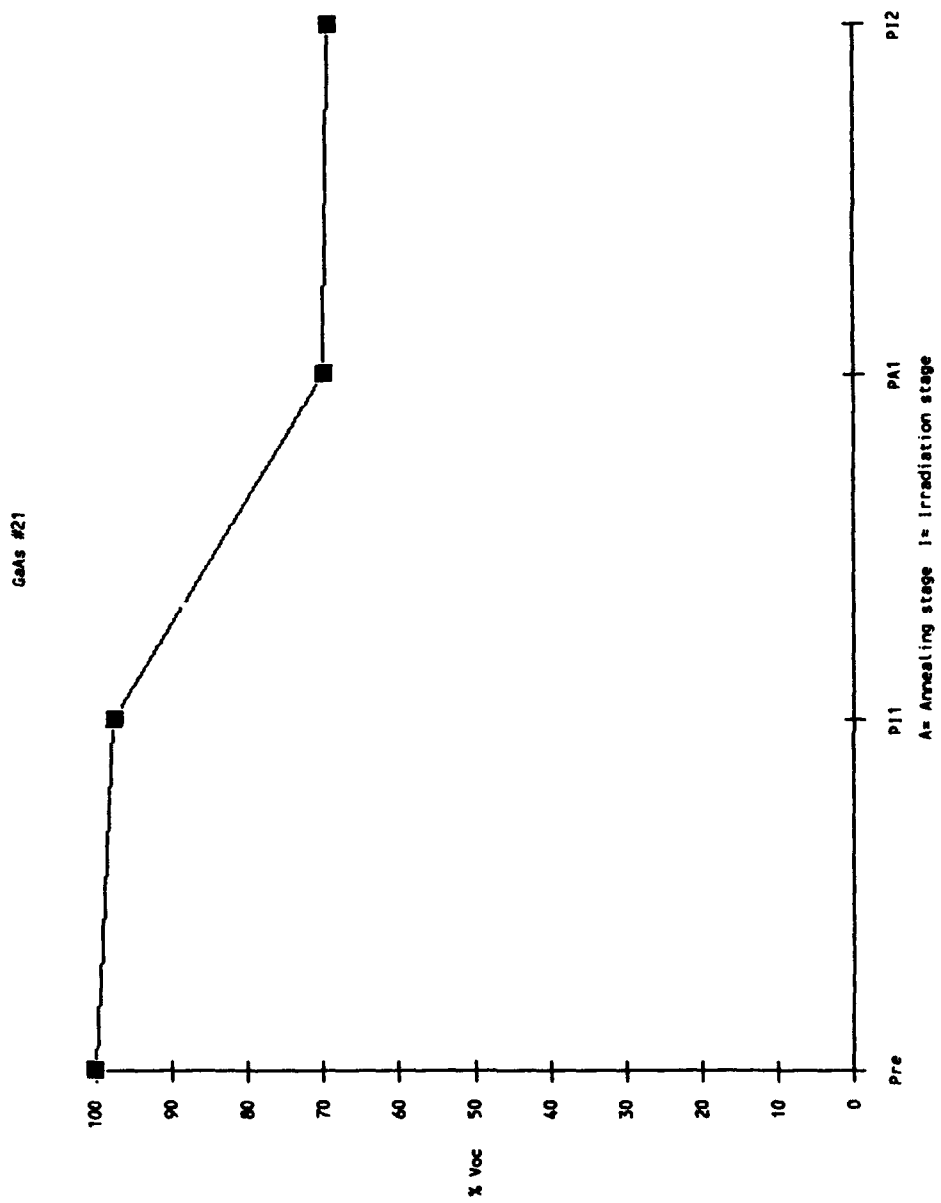


Figure C.10. Normalized  $V_{OC}$  plot for GaAs cell No. 21

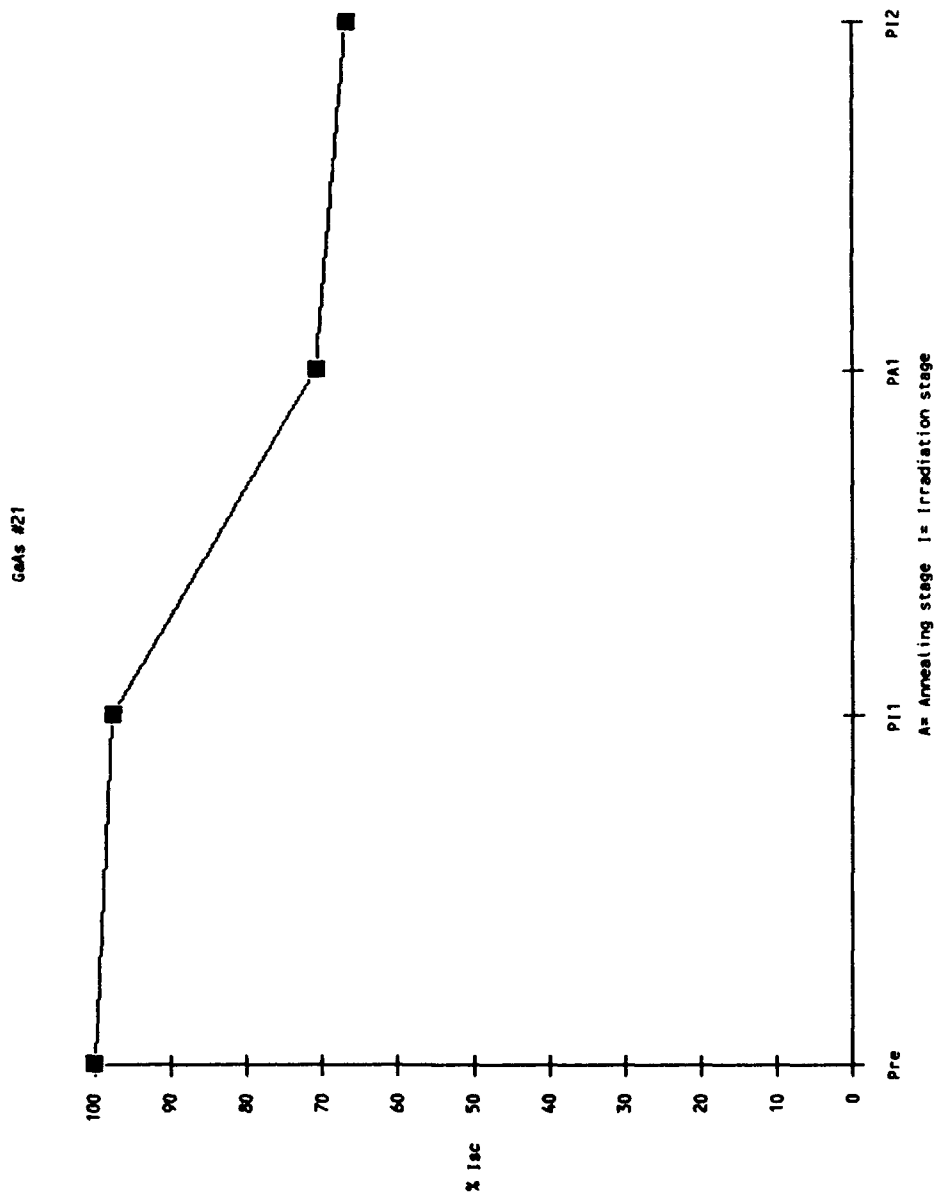


Figure C.11. Normalized  $I_{sc}$  plot for GaAs cell No. 21

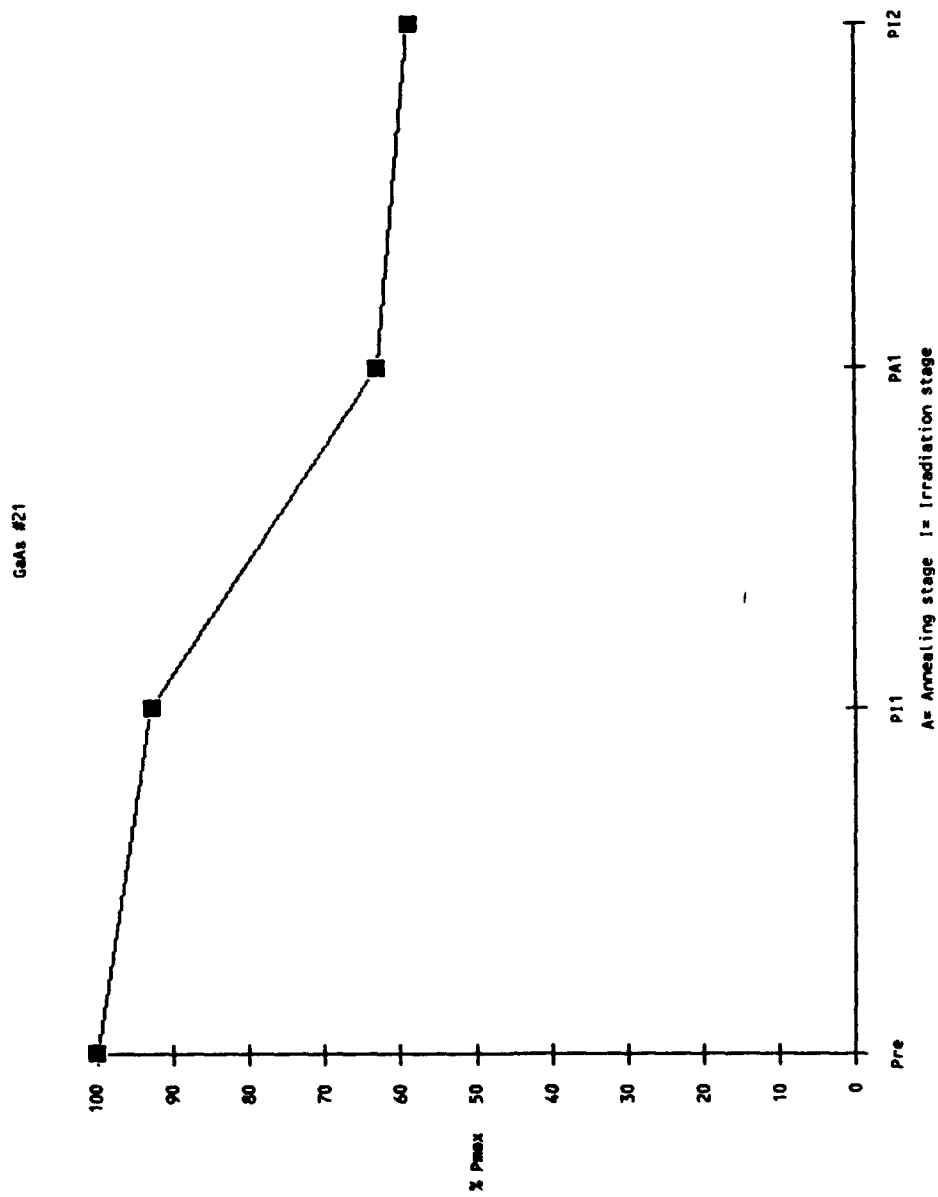


Figure C.12. Normalized  $P_{max}$  plot for GaAs cell No. 21

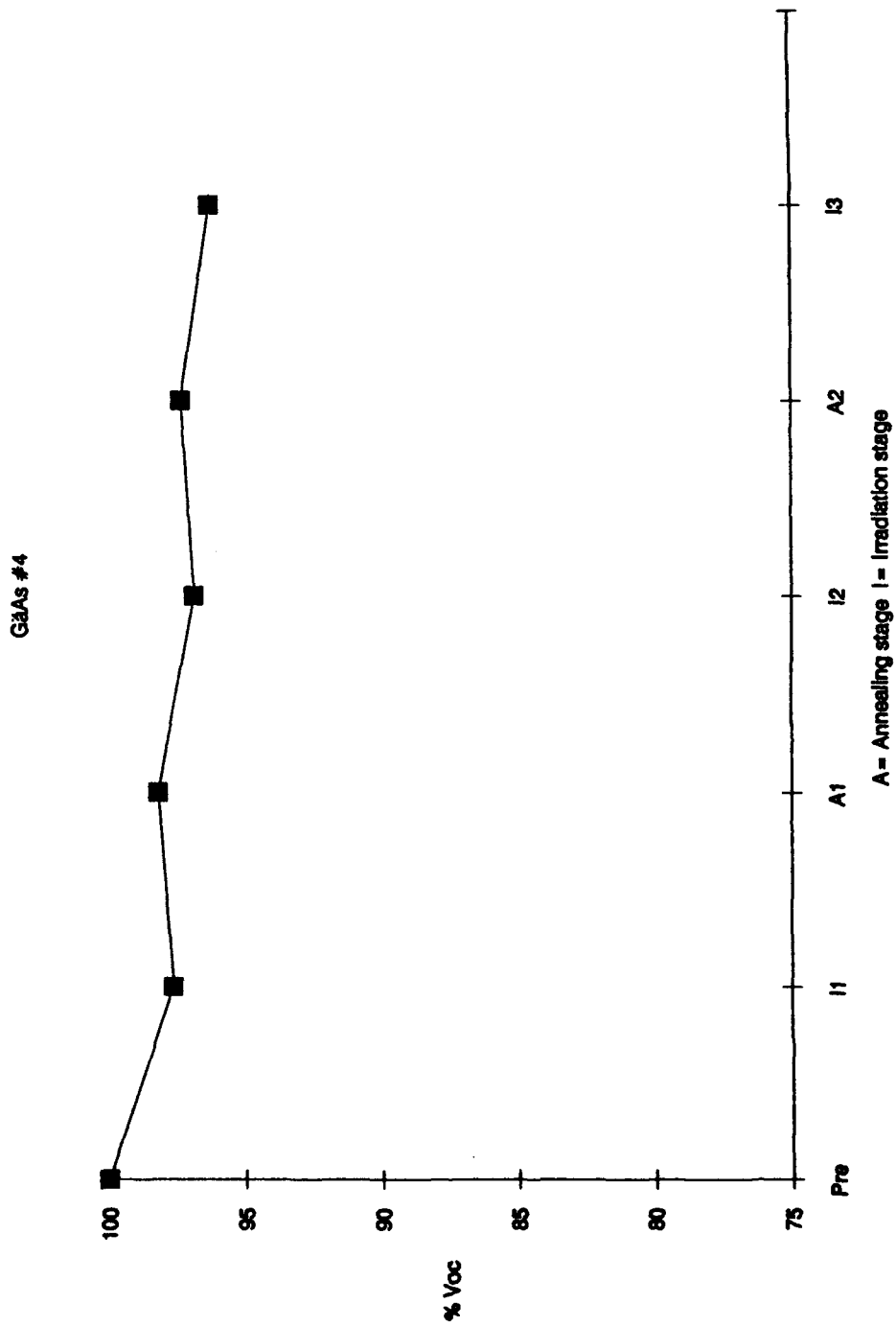


Figure C,13. Normalized  $V_{OC}$  plot for GaAs cell No. 4

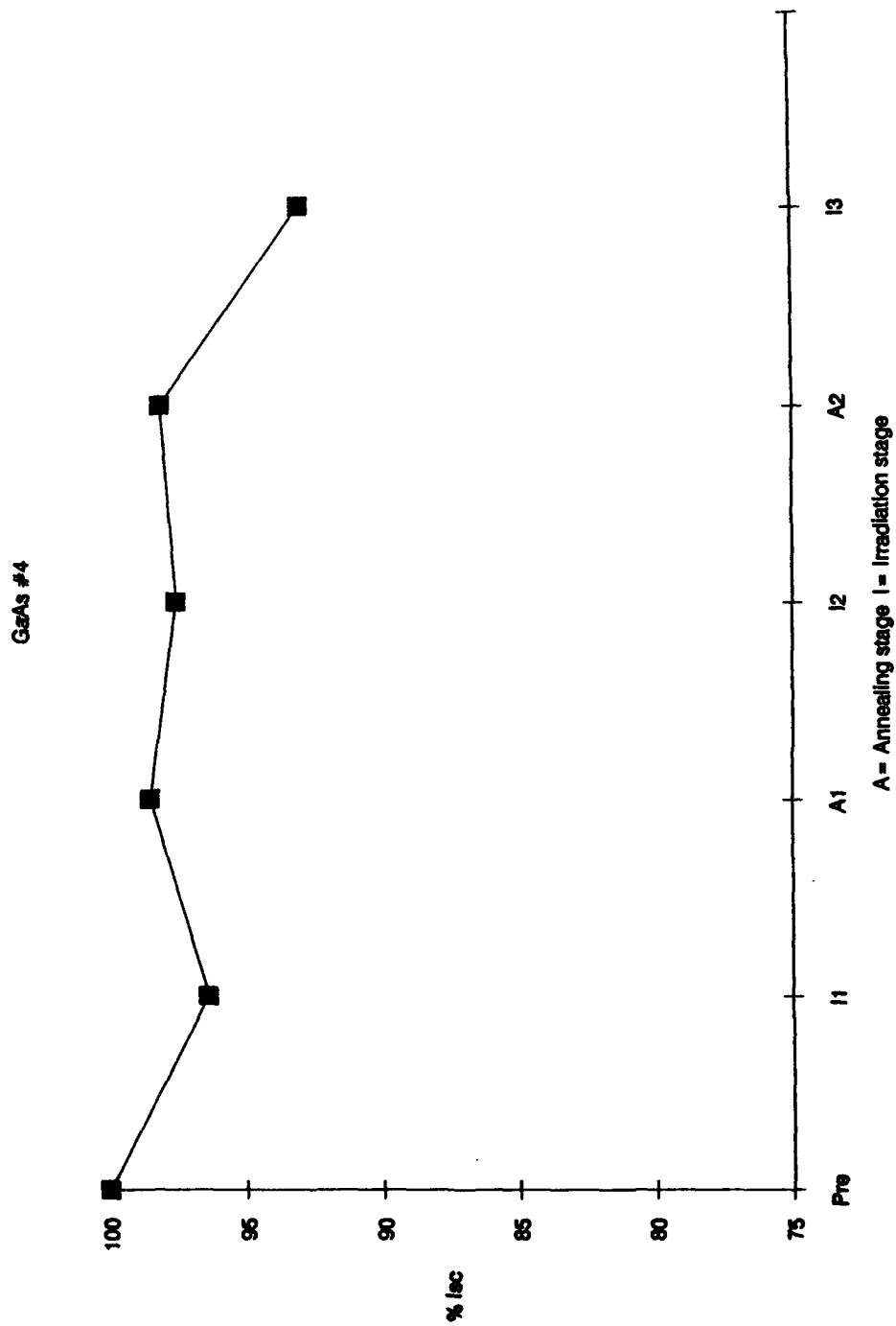


Figure C,14. Normalized  $I_{sc}$  plot for GaAs cell No. 4

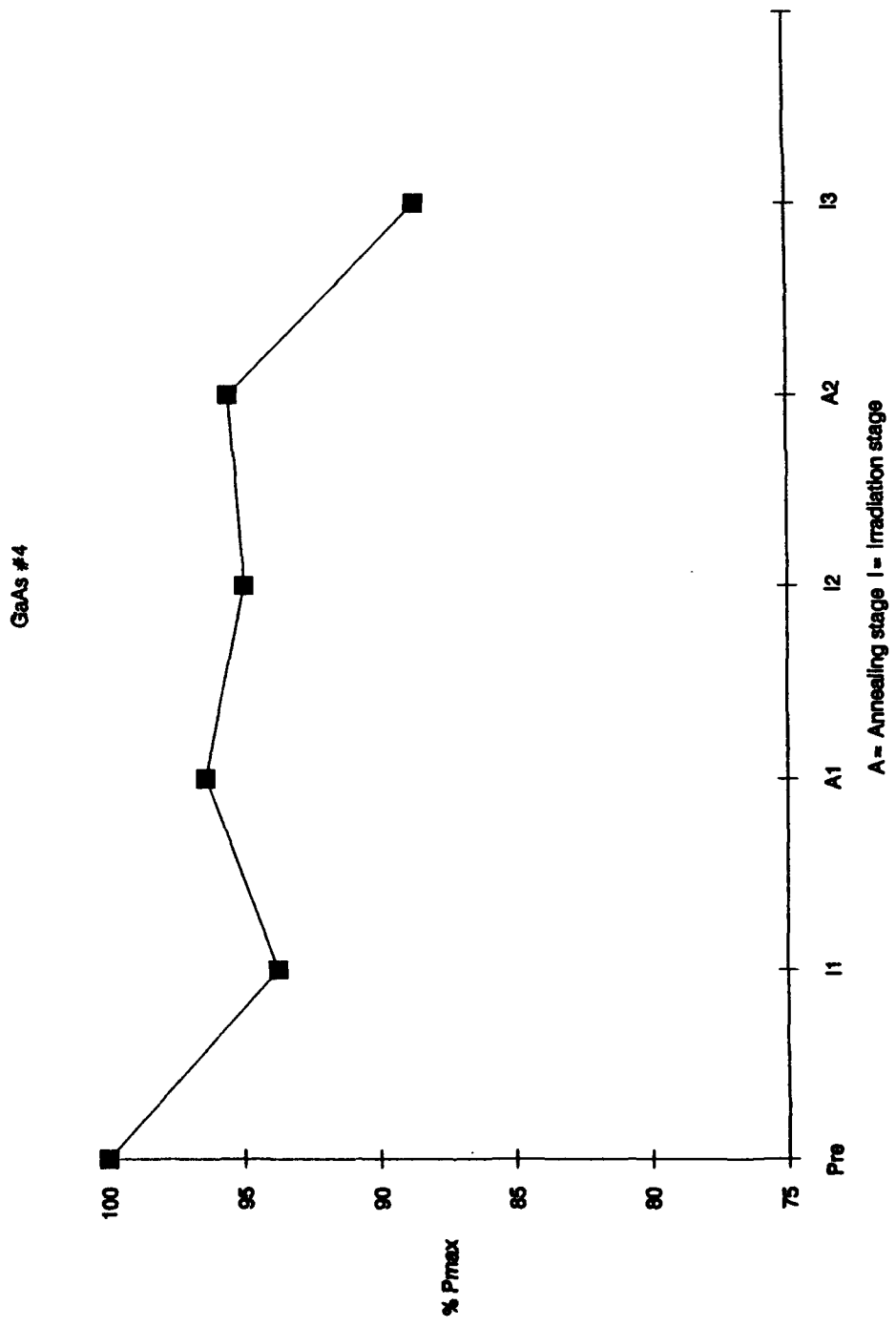


Figure C.15. Normalized P<sub>max</sub> plot for GaAs cell No. 4

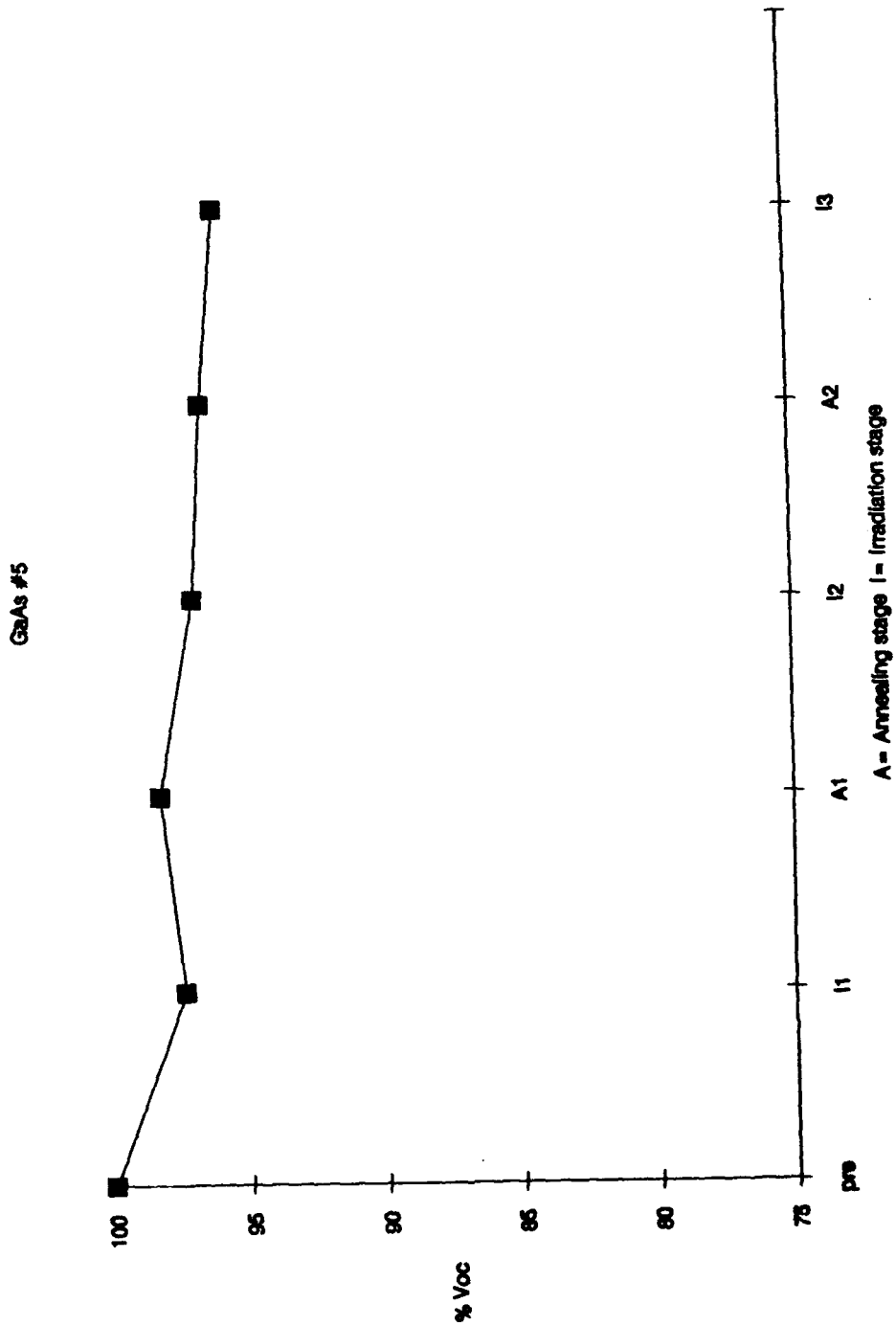


Figure C,16. Normalized  $V_{OC}$  plot for GaAs cell No. 5

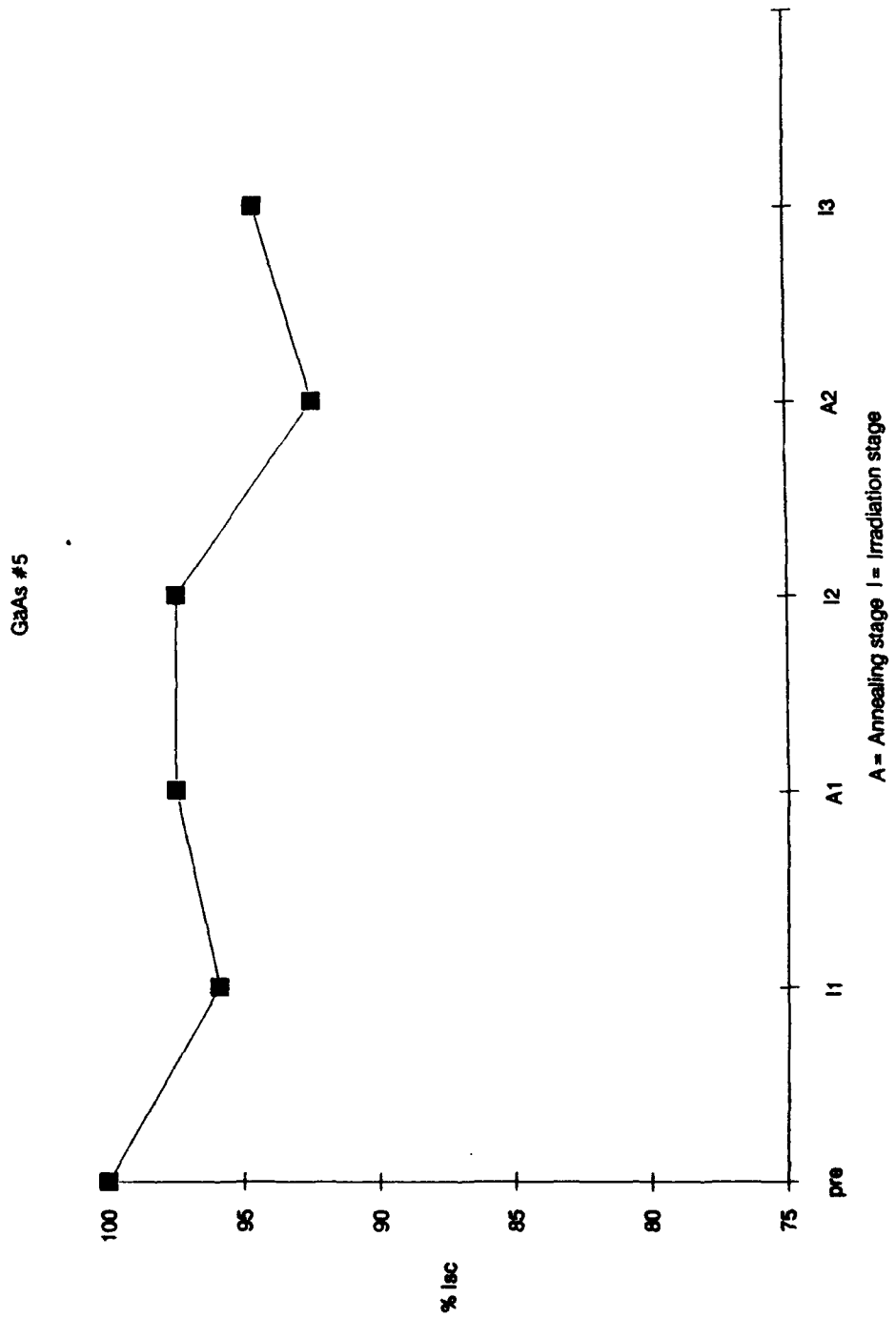


Figure C.17. Normalized  $I_{sc}$  plot for GaAs cell No. 5



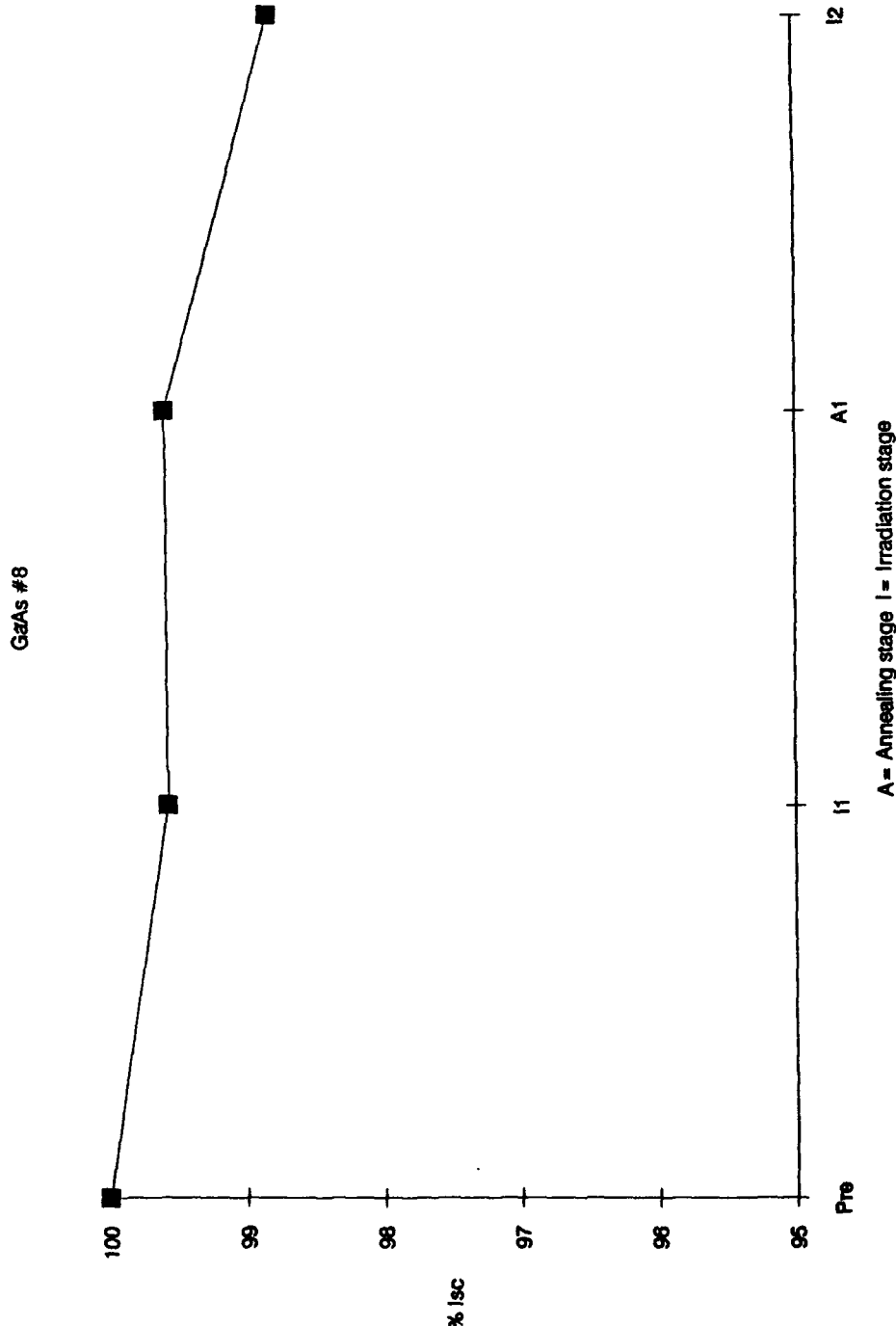


Figure C.20. Normalized I<sub>sc</sub> plot for GaAs cell No. 8

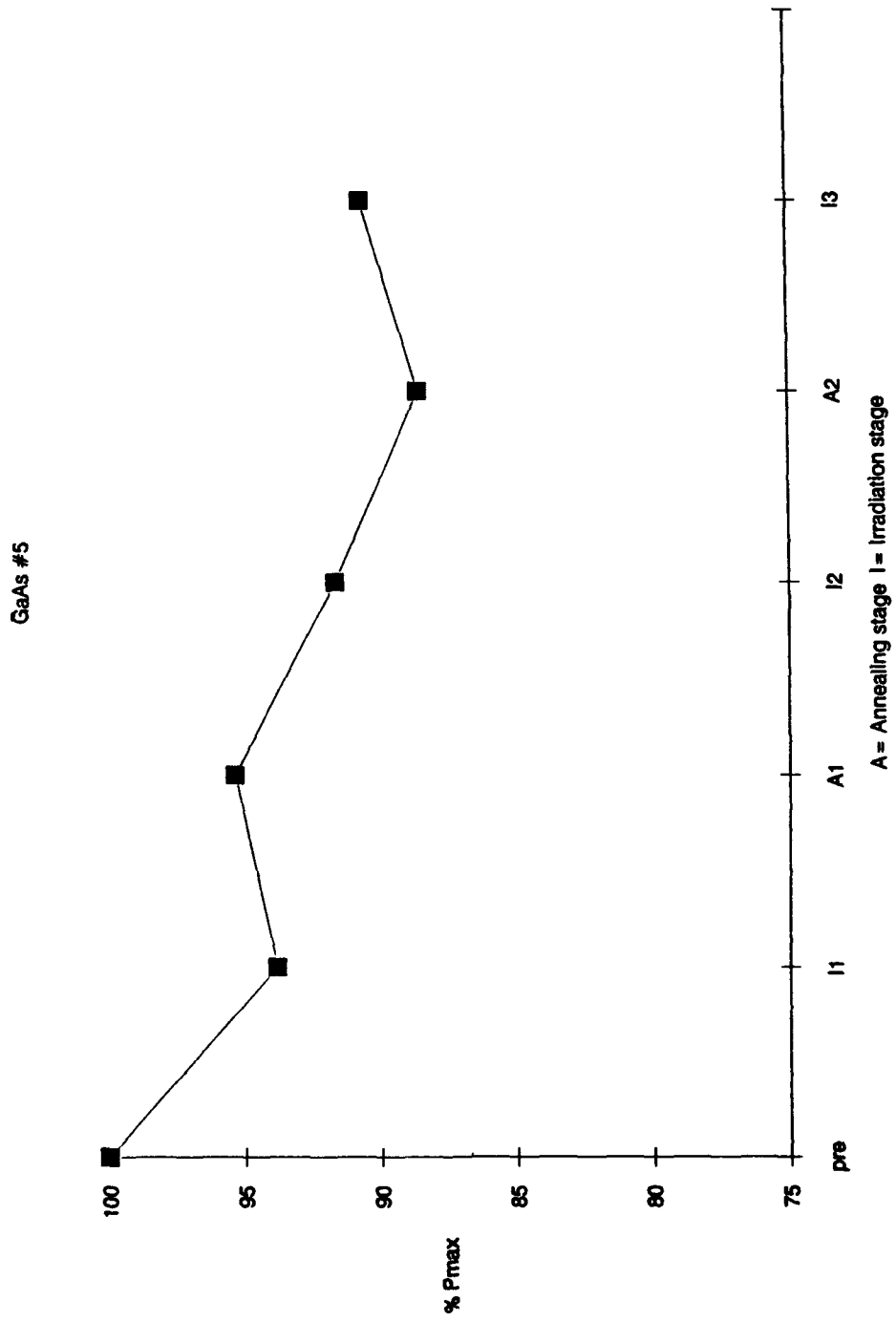


Figure C.18. Normalized P<sub>max</sub> plot for GaAs cell No. 5

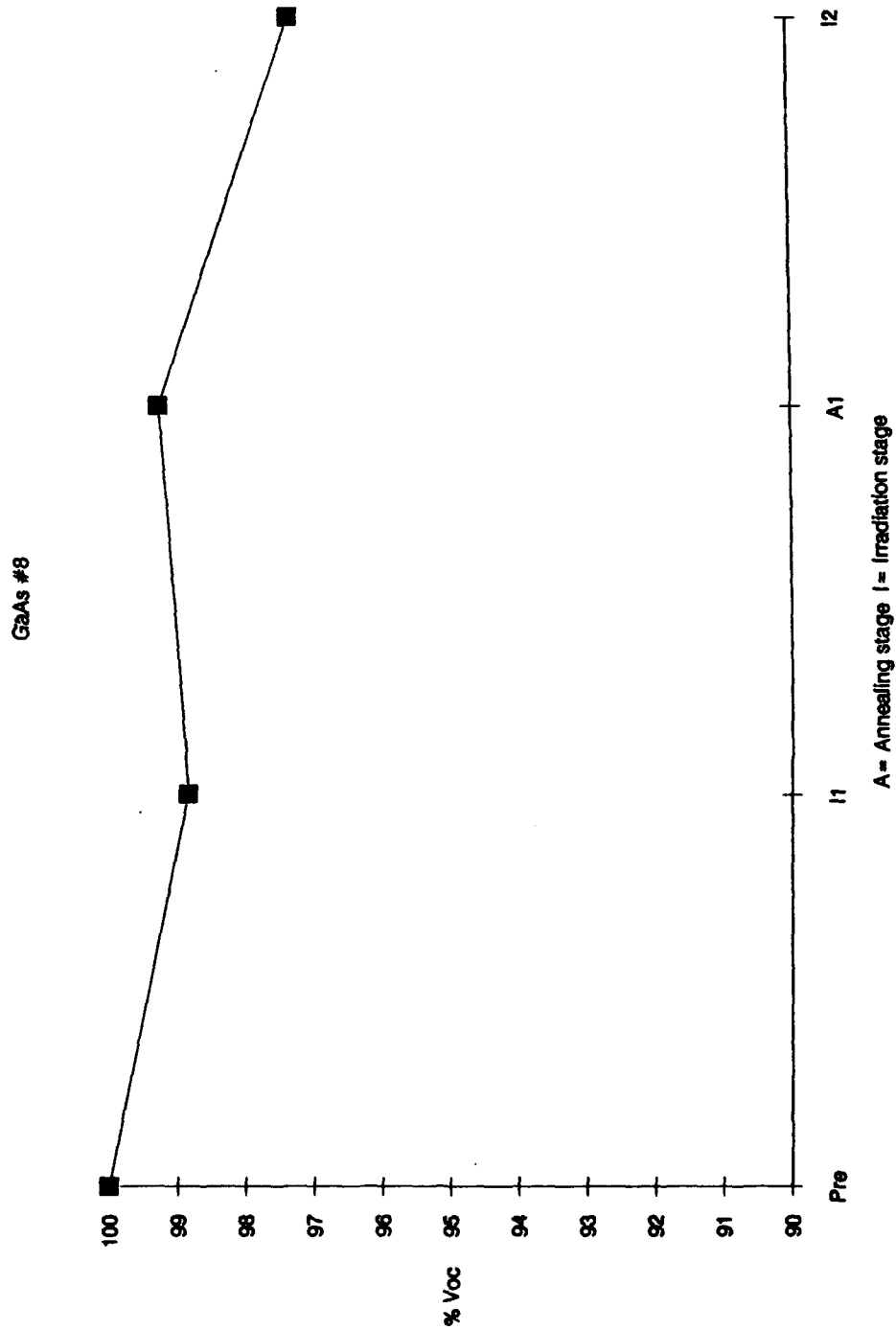


Figure C.19. Normalized  $V_{oc}$  plot for GaAs cell No. 8

GaAs #8

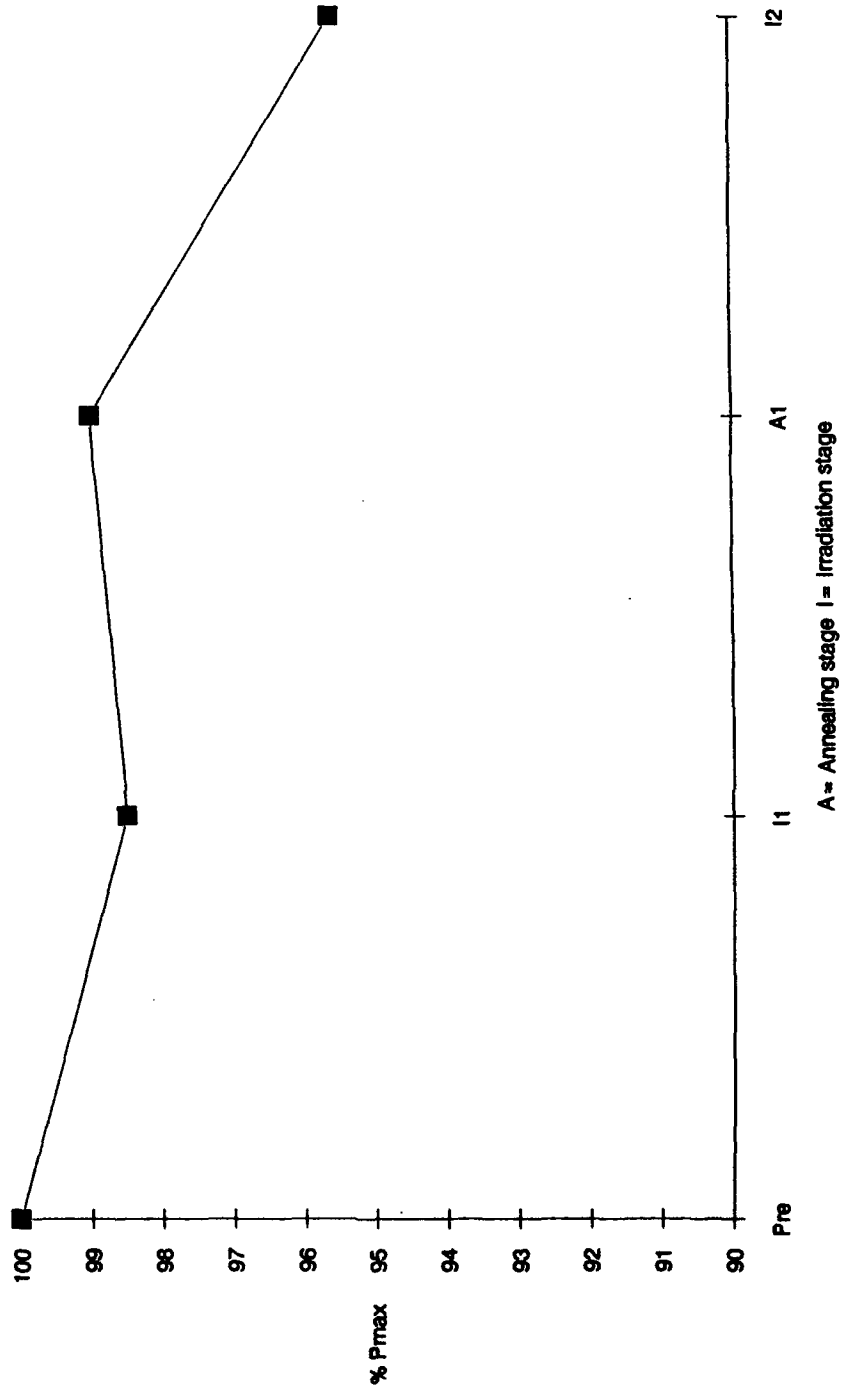


Figure C.21. Normalized P<sub>max</sub> plot for GaAs cell No. 8

APPENDIX D  
I-V CURVES FOR MULTIPLE CYCLES OF IRRADIATED  
AND ANNEALED InP SOLAR CELLS

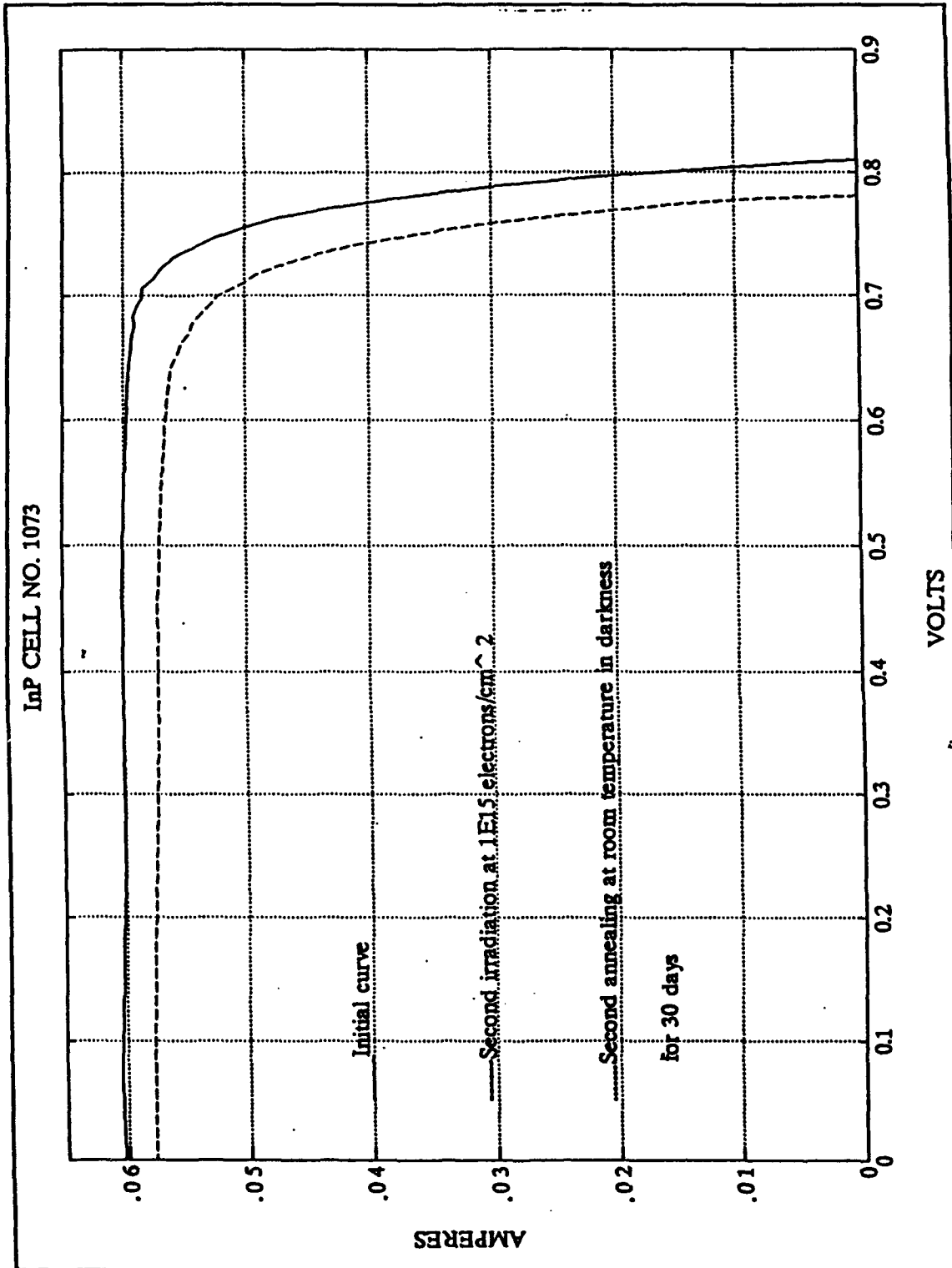


Figure D.2. I-V curves for InP cell No. 1073  
[from Ref. 2]

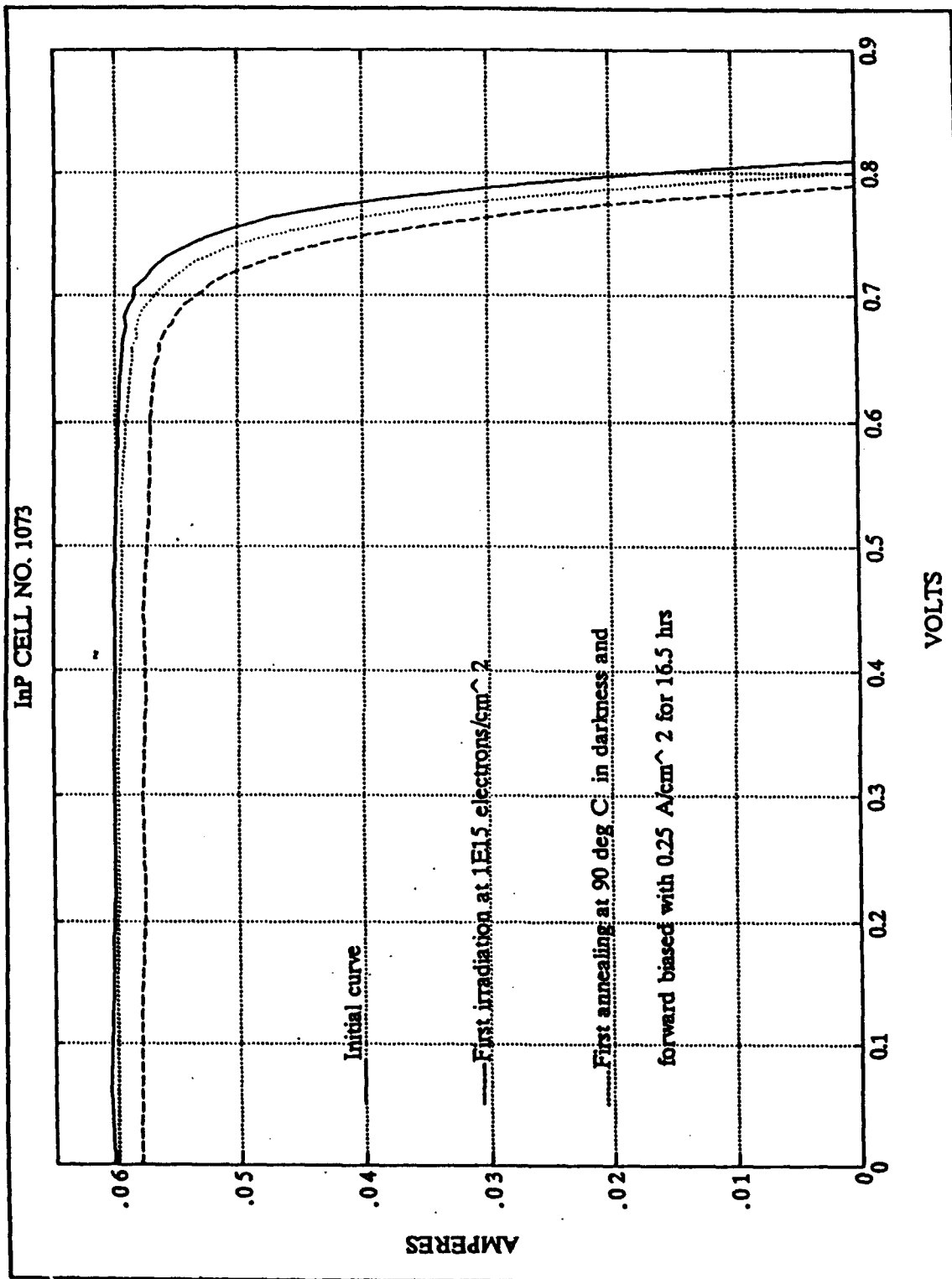


Figure D.1. I-V curves for InP cell No. 1073 [from Ref. 2]

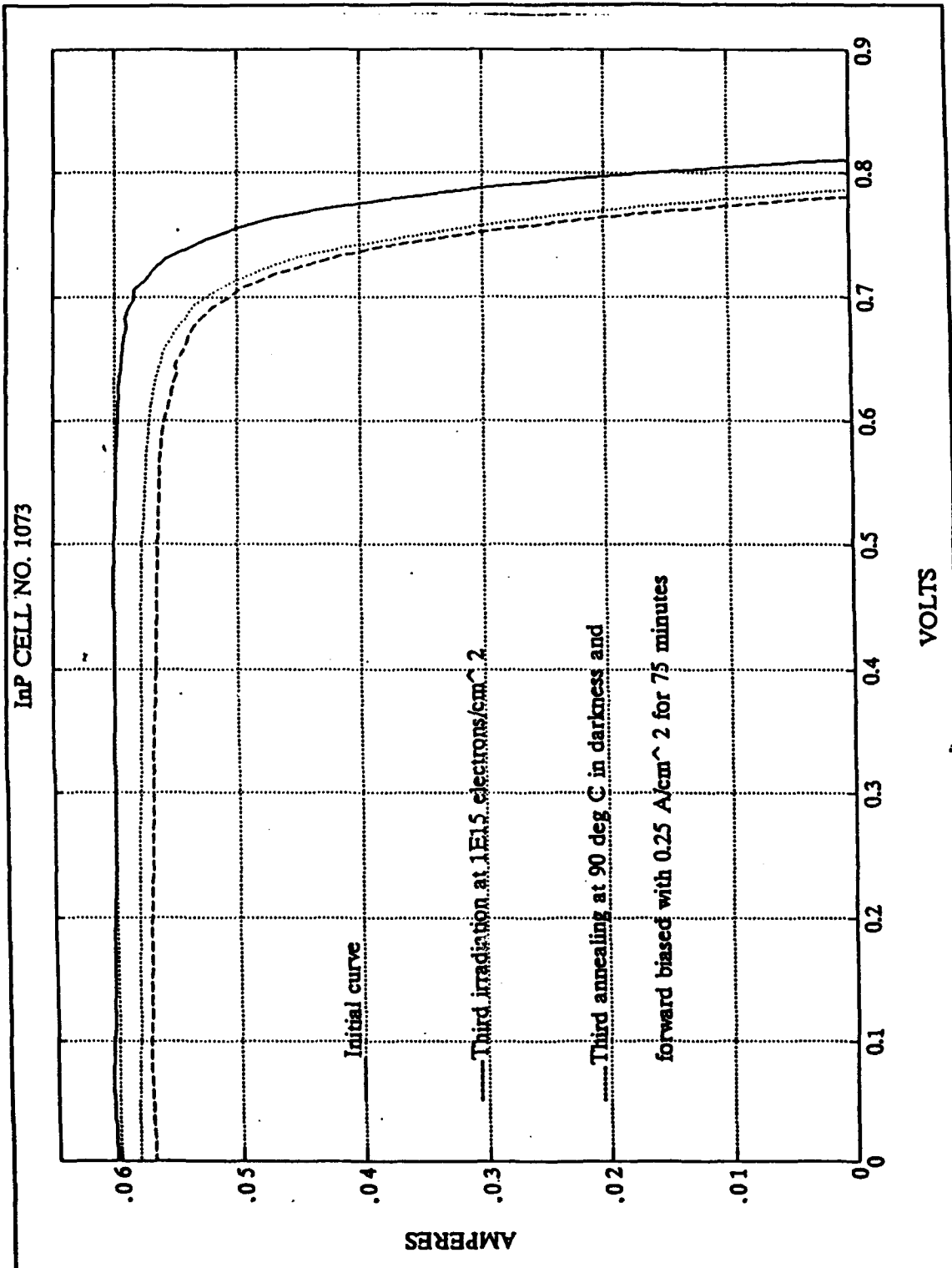


Figure D.3. I-V curves for InP cell No. 1073  
 [from Ref. 2]



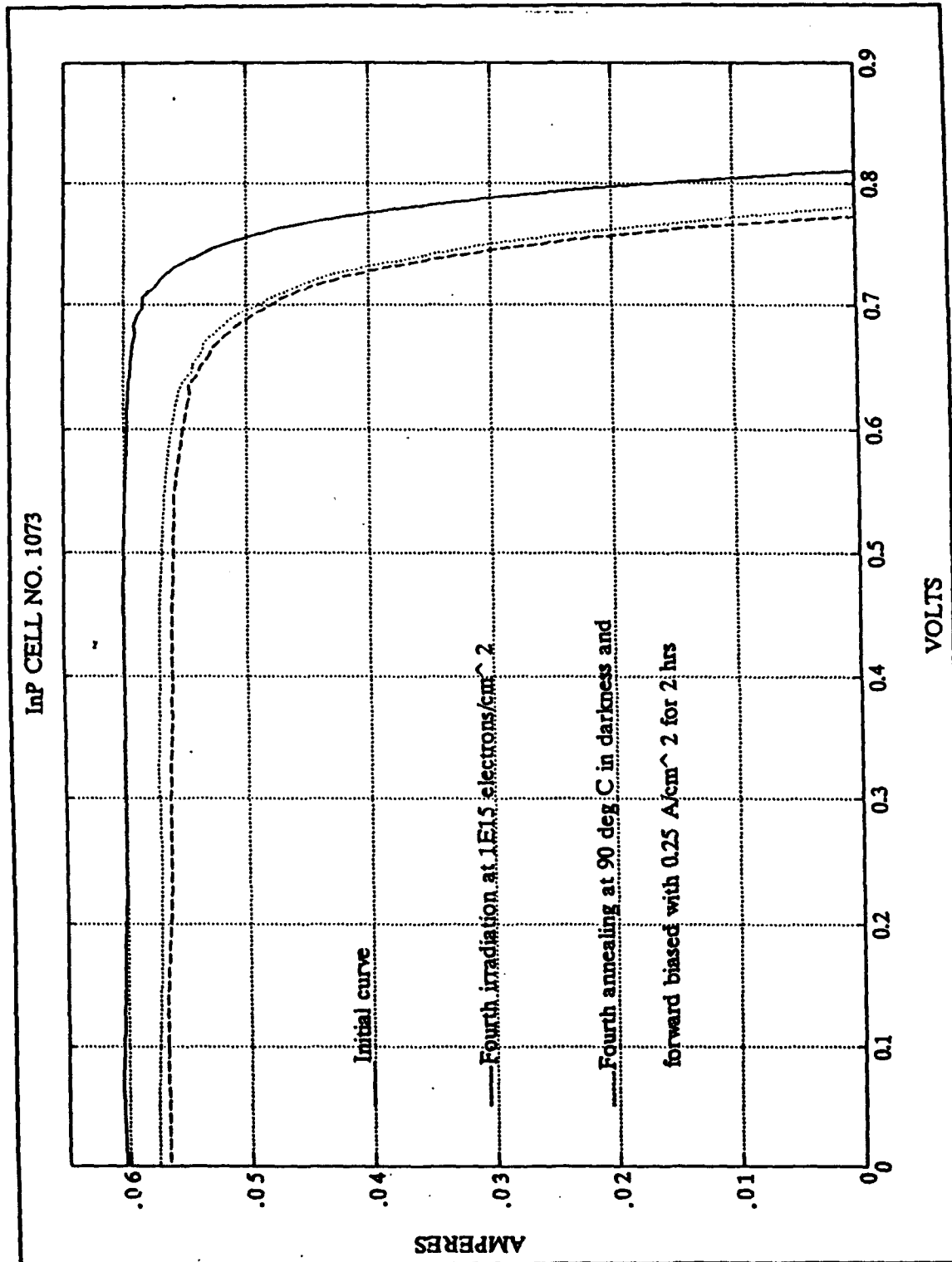


Figure D.4. I-V curves for InP cell No. 1073  
[from Ref. 2]

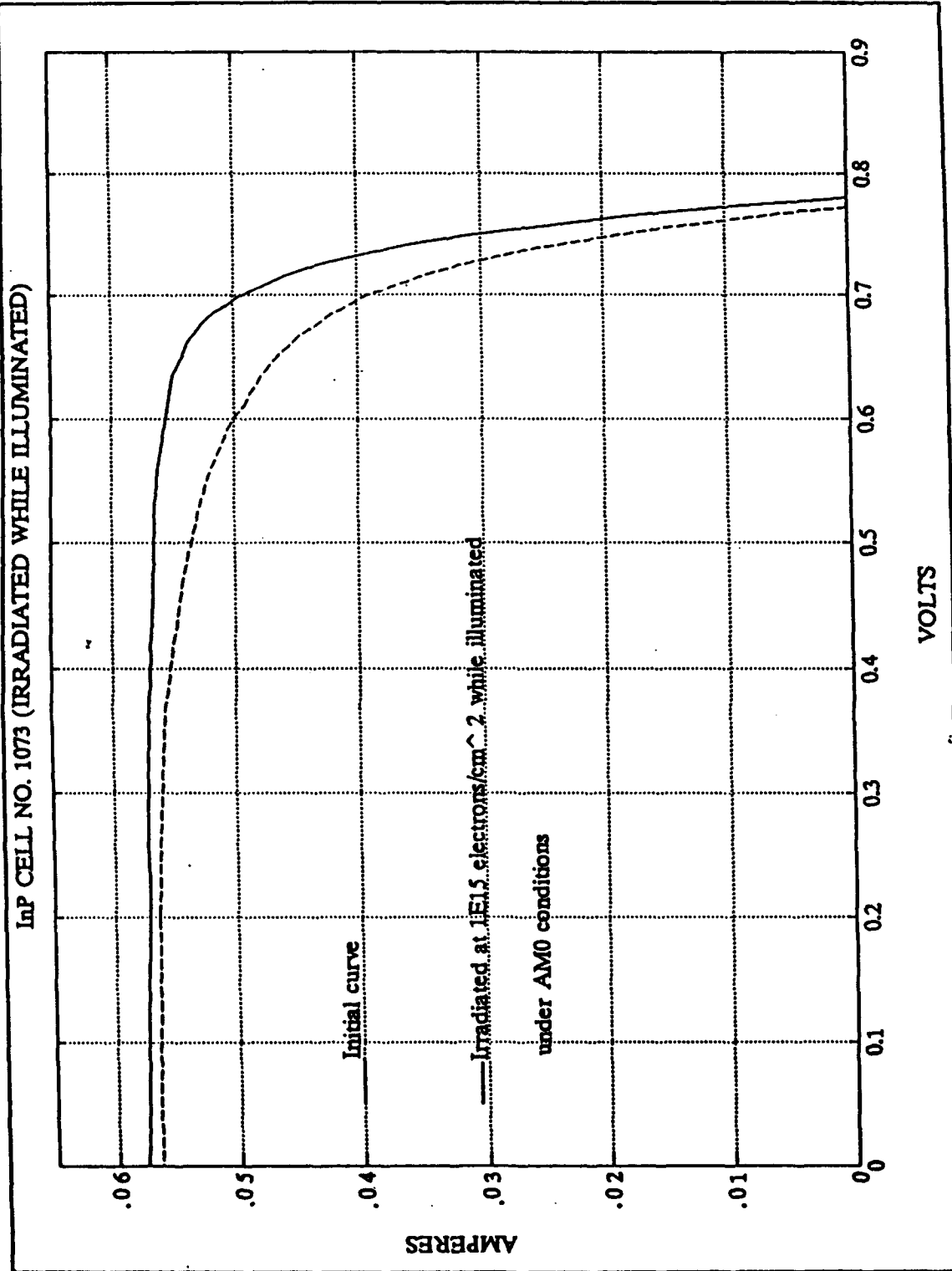


Figure D.5. I-V curves for InP cell No. 1073 [from Ref. 2]

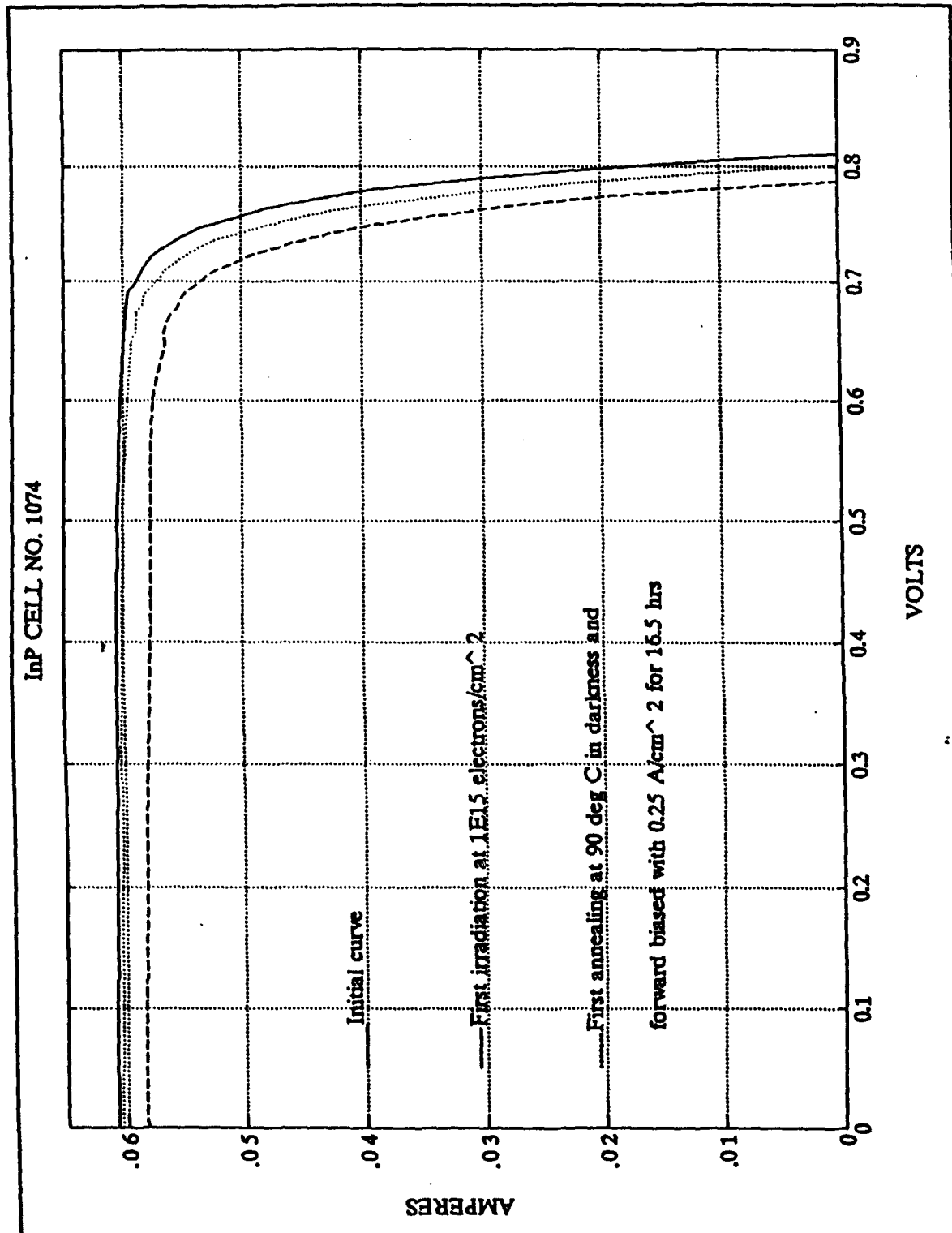


Figure D.6. I-V curves for InP cell No. 1074  
[from Ref. 2]

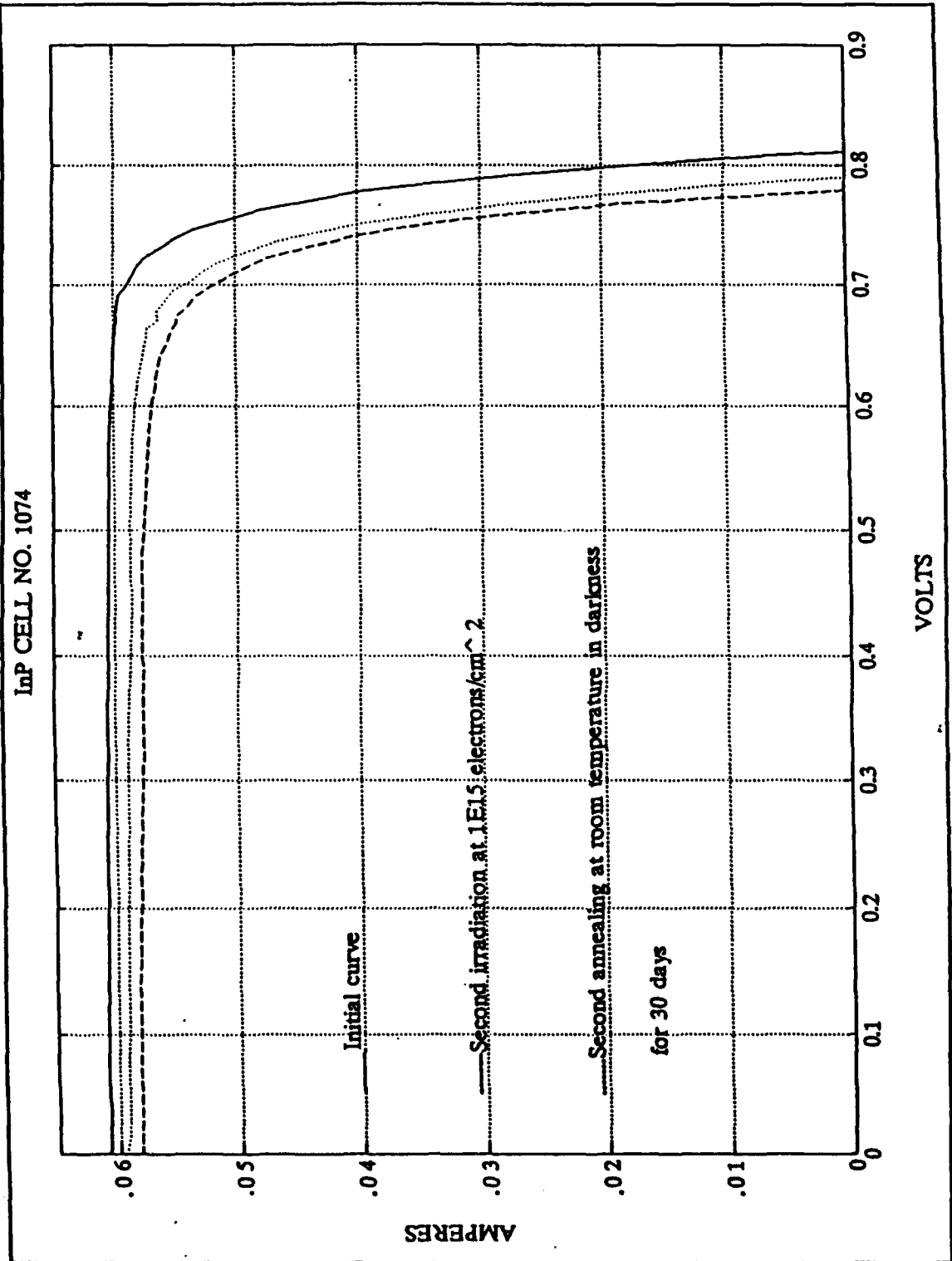


Figure D.7. I-V curves for InP cell No. 1074 [from Ref. 2]

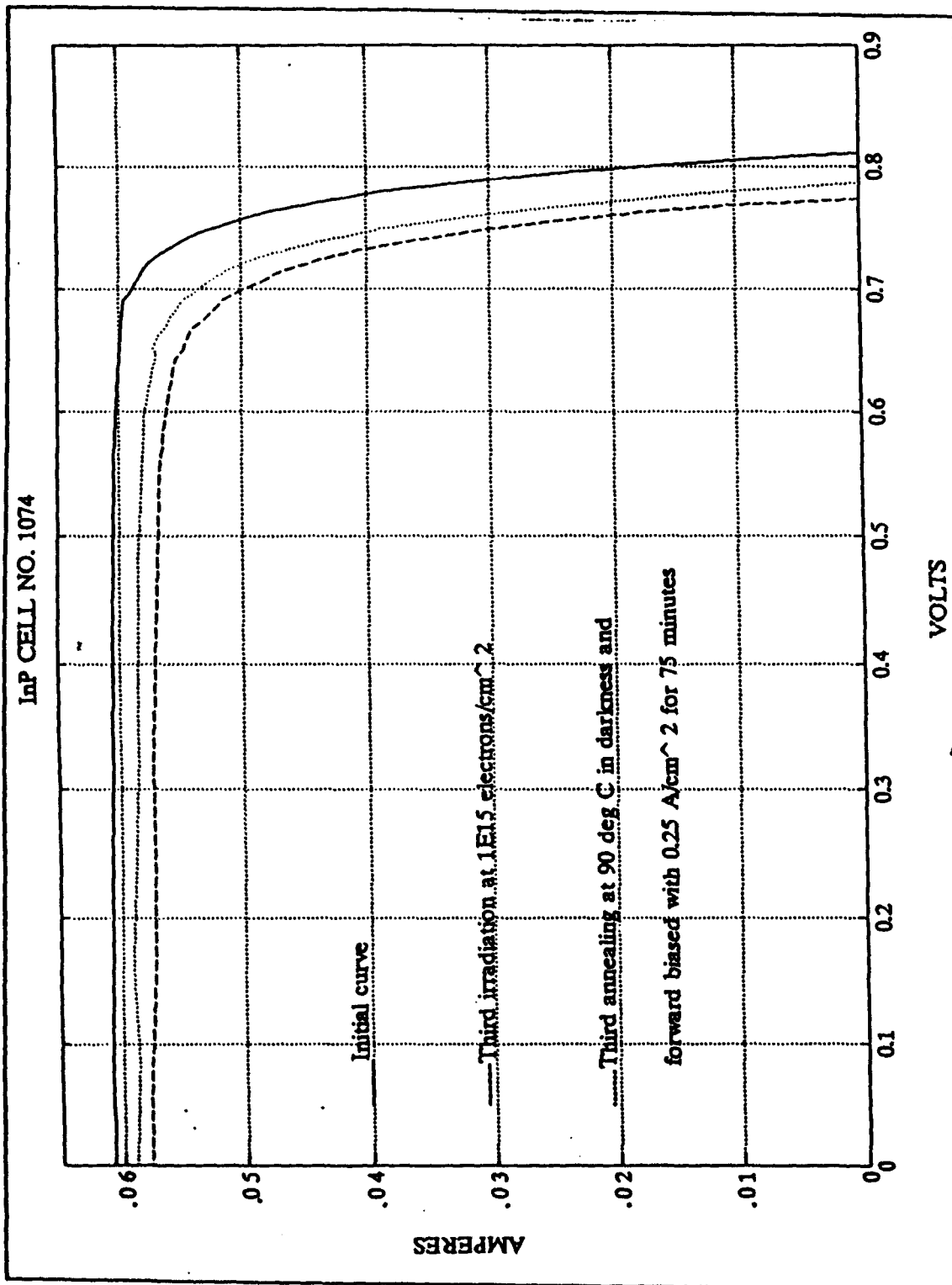


Figure D.8. I-V curves for InP cell No. 1074  
[from Ref. 2]

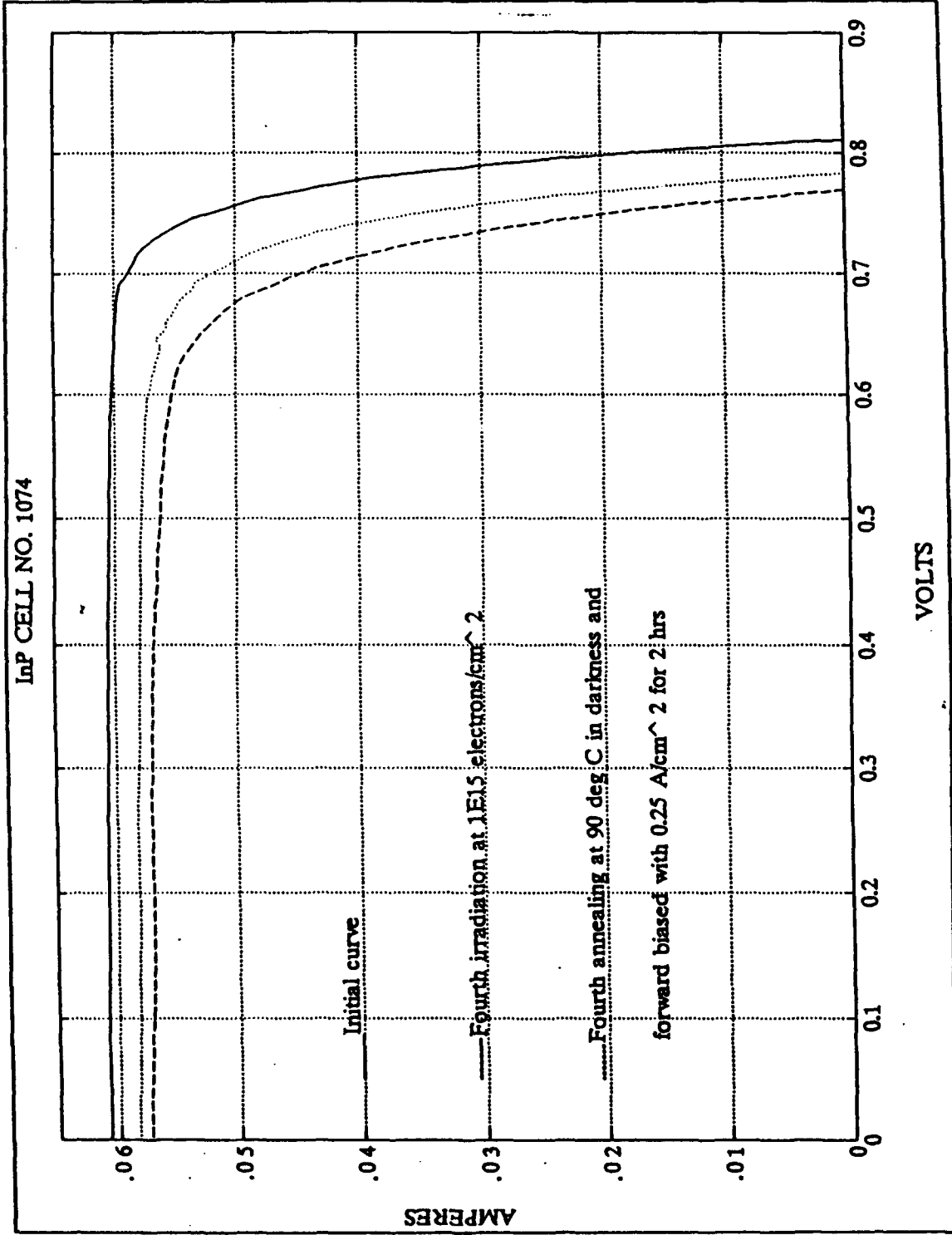


Figure D.9. I-V curves for InP cell No. 1074 [from Ref. 2]

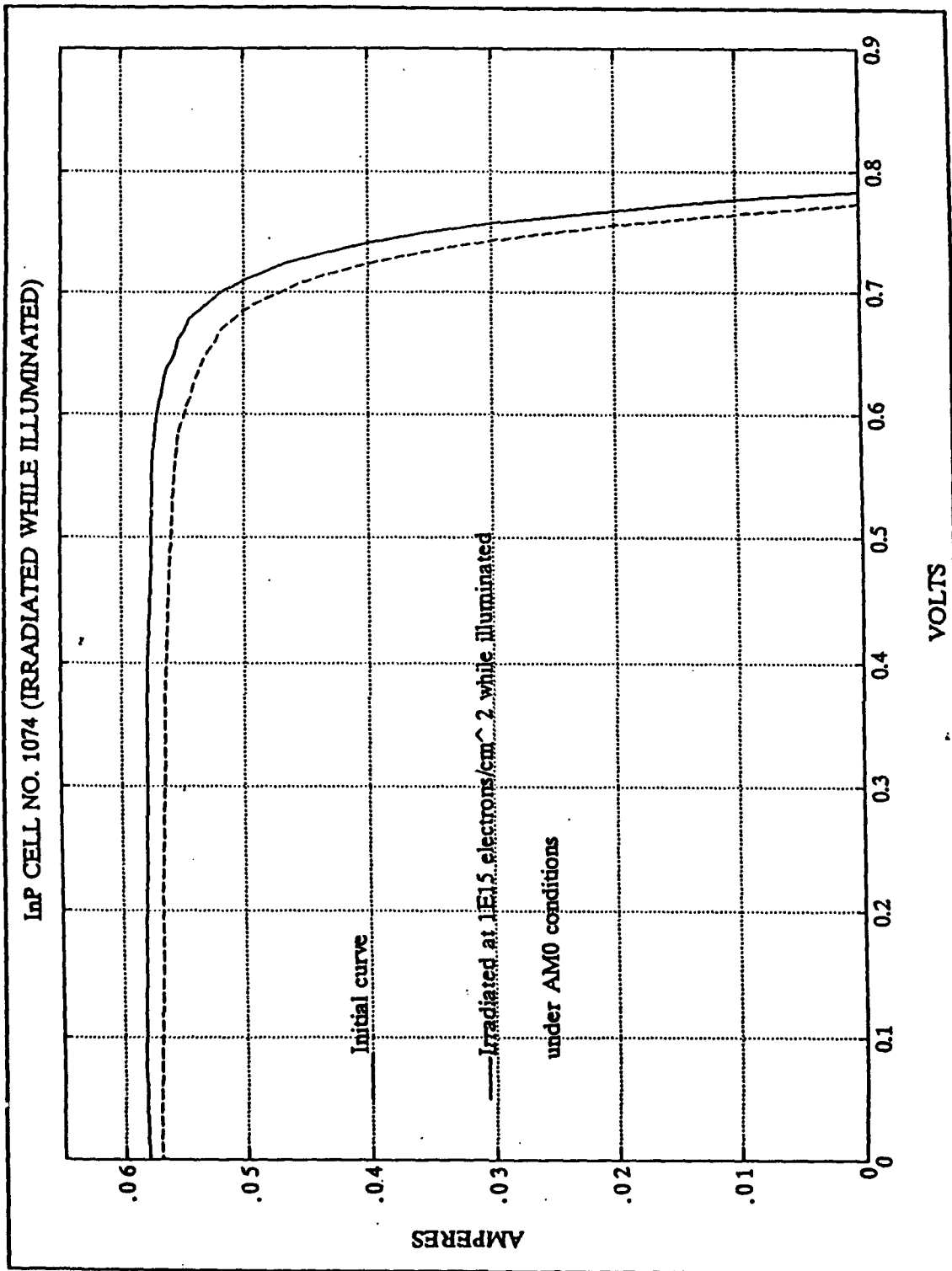


Figure D.10. I-V curves for InP cell No. 1074  
[from Ref. 2]

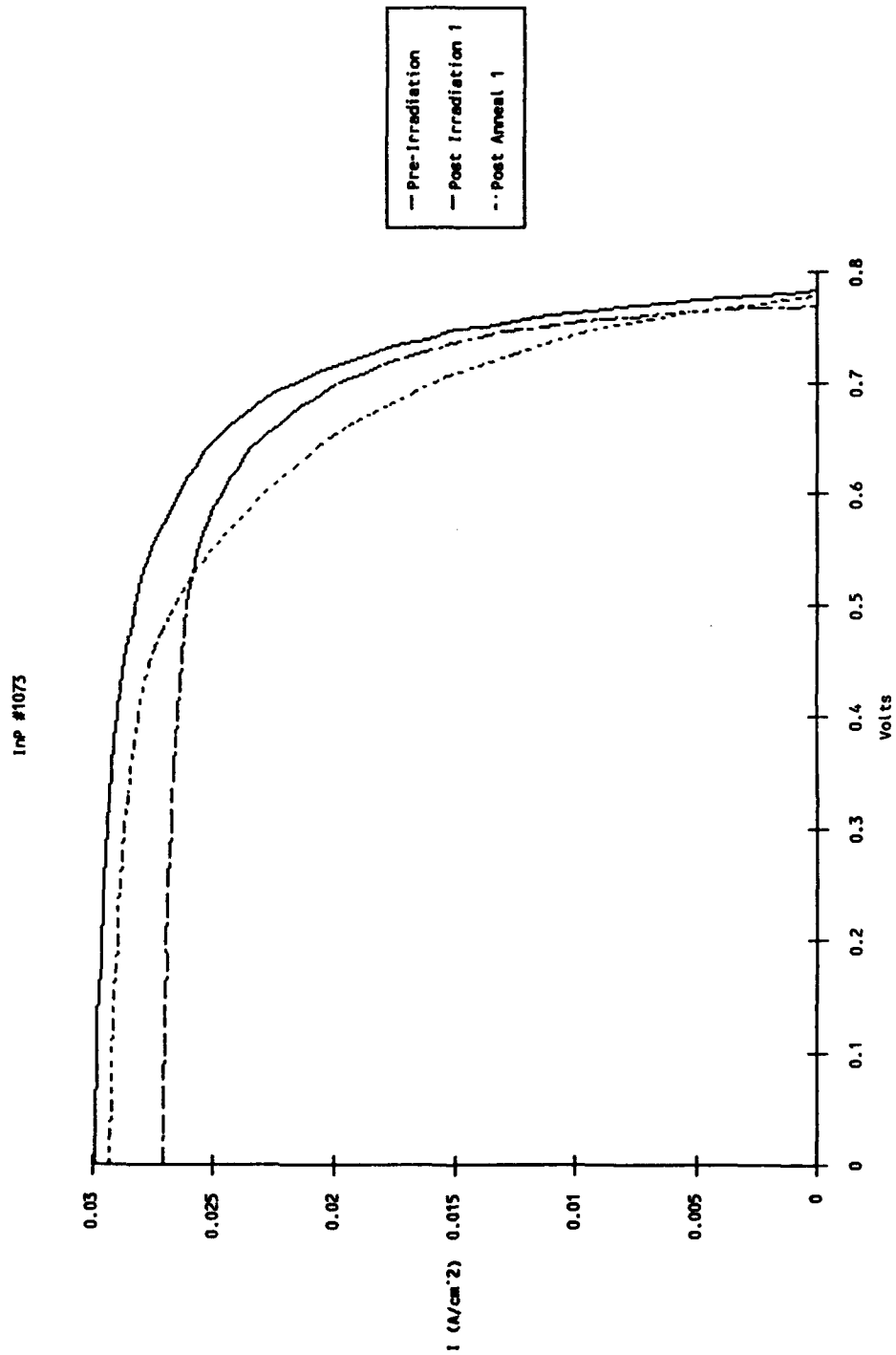


Figure D.11. I-V curves for InP cell No. 1073



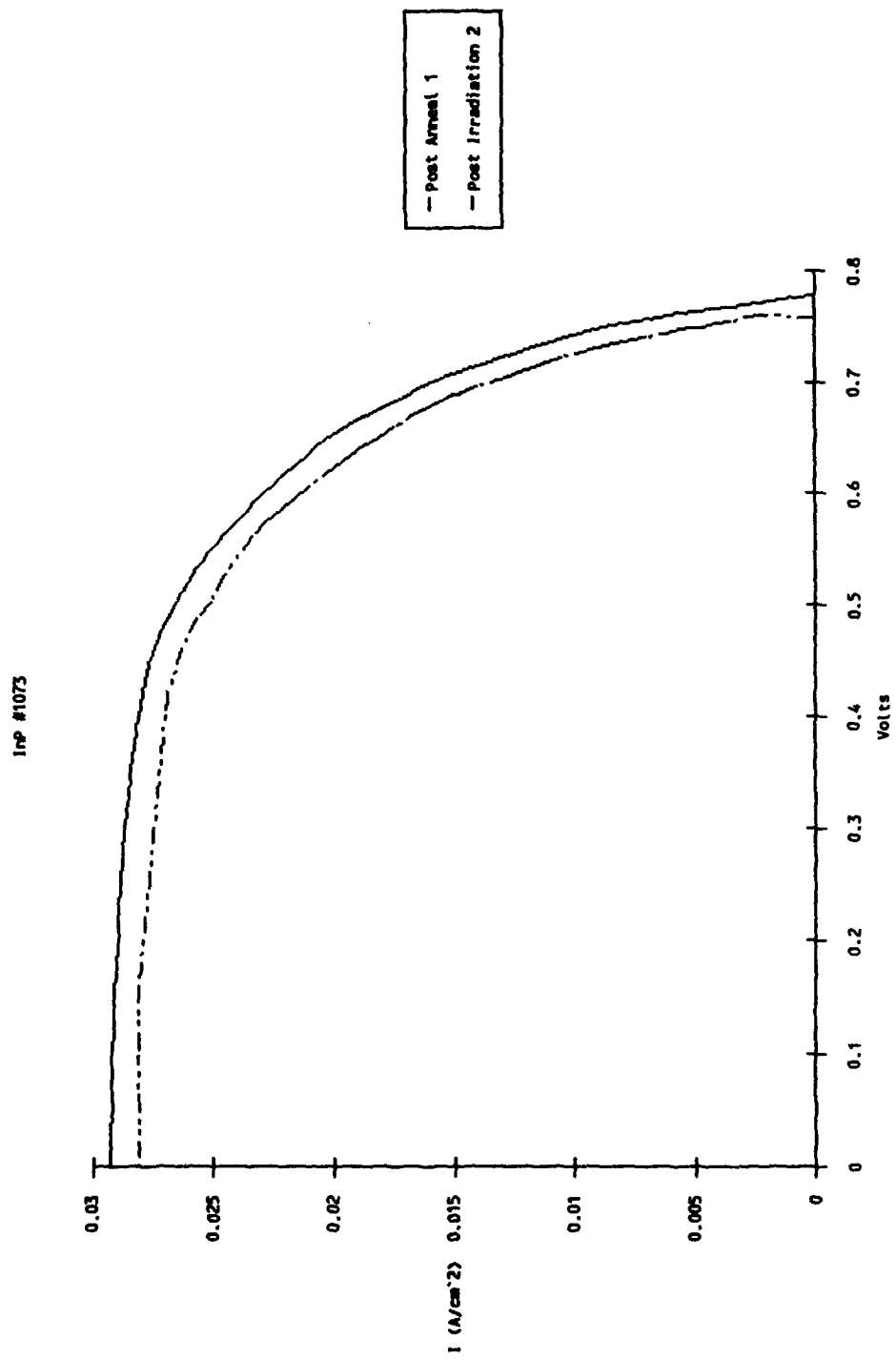


Figure D.12. I-V curves for InP cell No. 1073

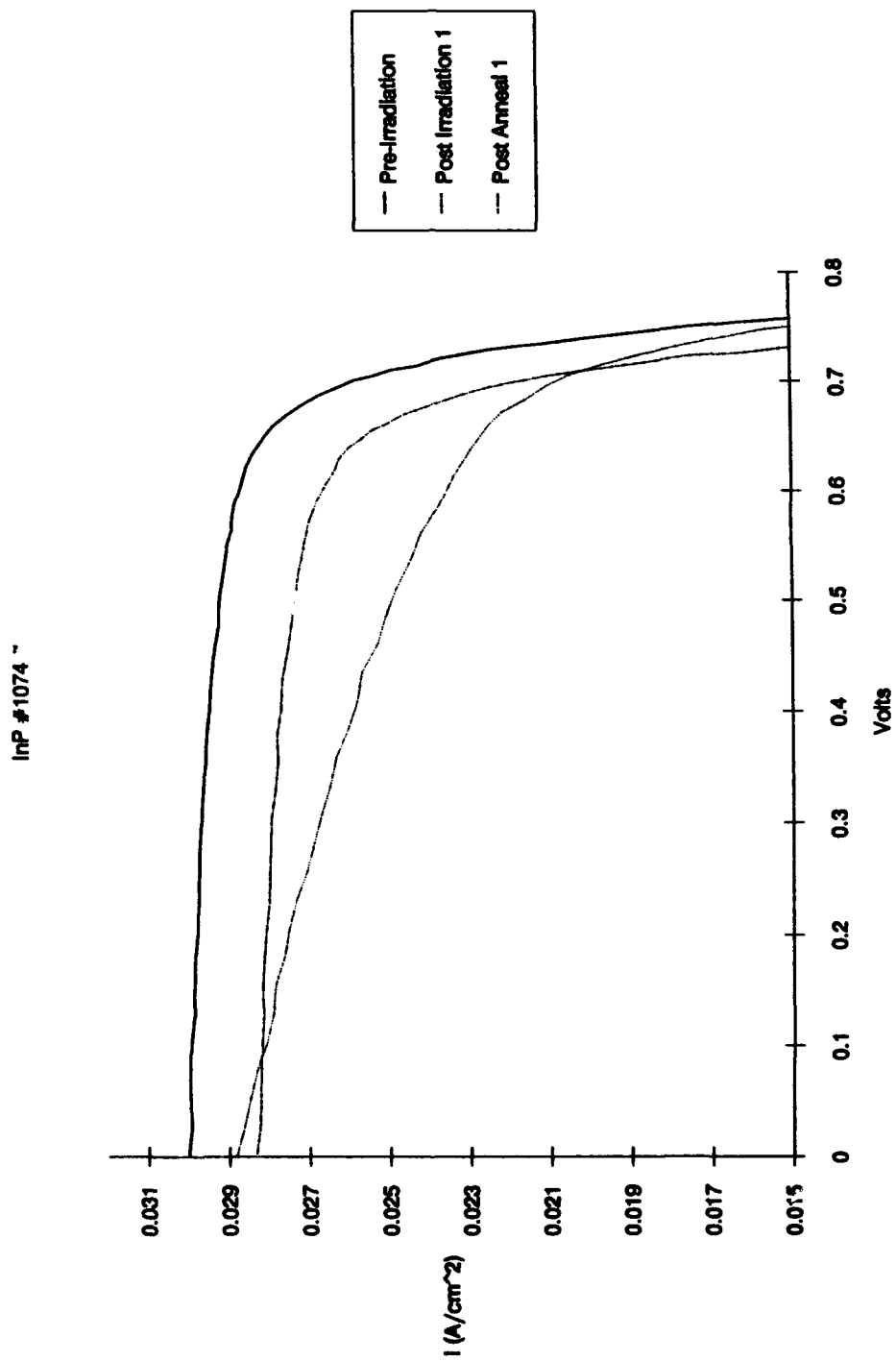


Figure D.13. I-V curves for InP cell No. 1074

InP #1074

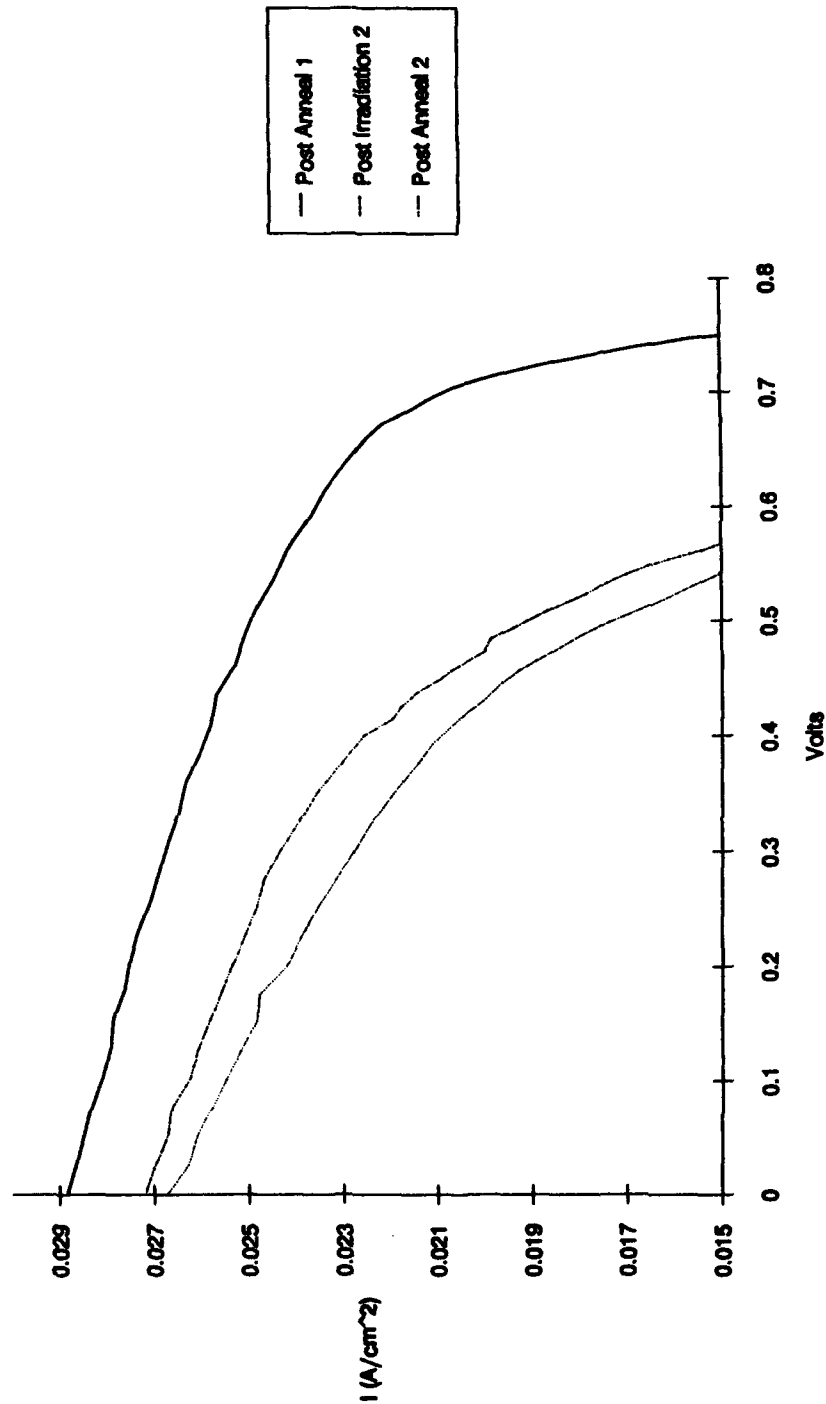


Figure D.14. I-V curves for InP cell No. 1074

InP #1074

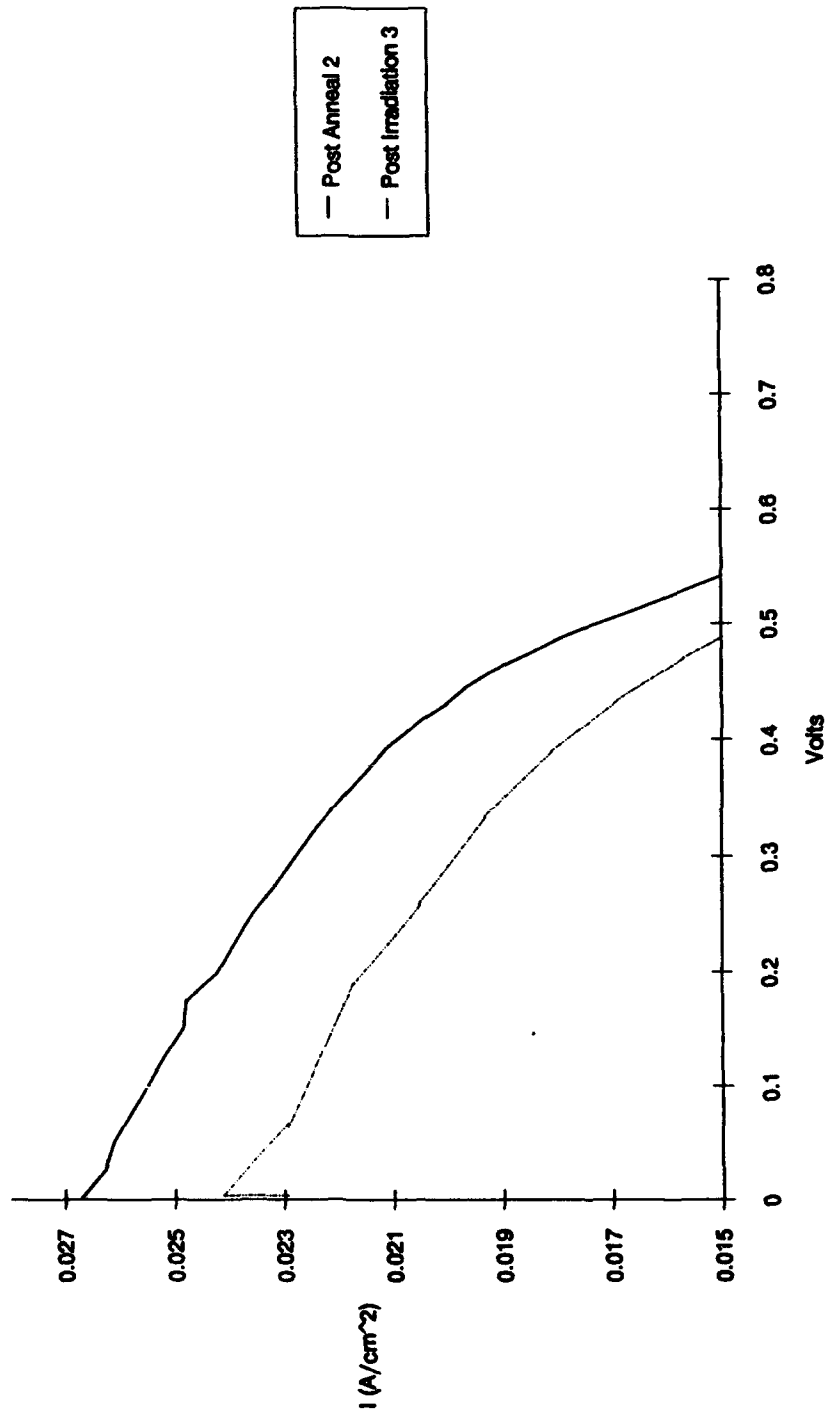


Figure D.15. I-V curves for InP cell No. 1074

APPENDIX E  
OPEN CIRCUIT VOLTAGE, SHORT CIRCUIT CURRENT, AND  
MAXIMUM POWER NORMALIZED PLOTS FOR InP SOLAR CELLS

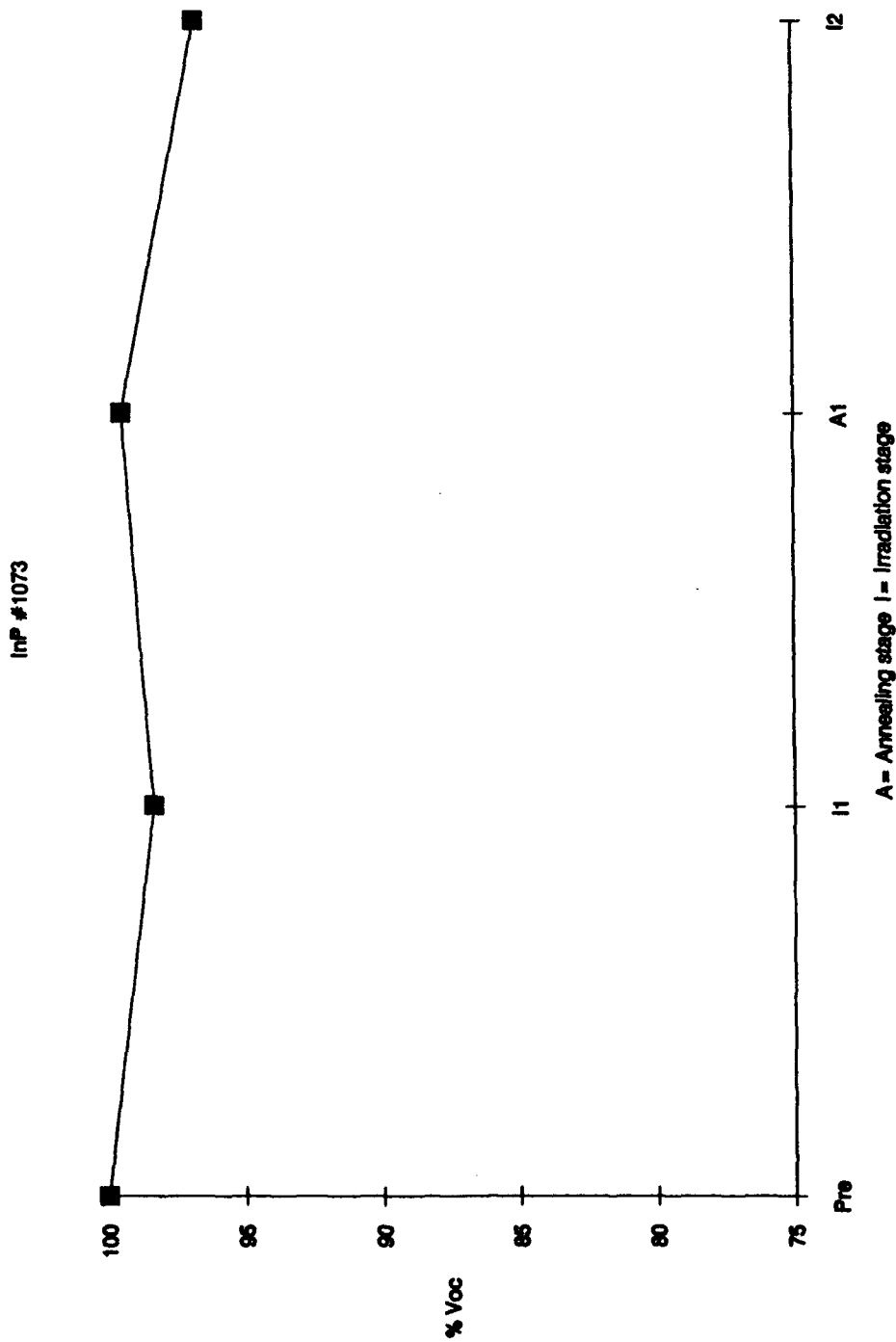


Figure E.1. Normalized Voc plot for InP cell No. 1073

InP #1073

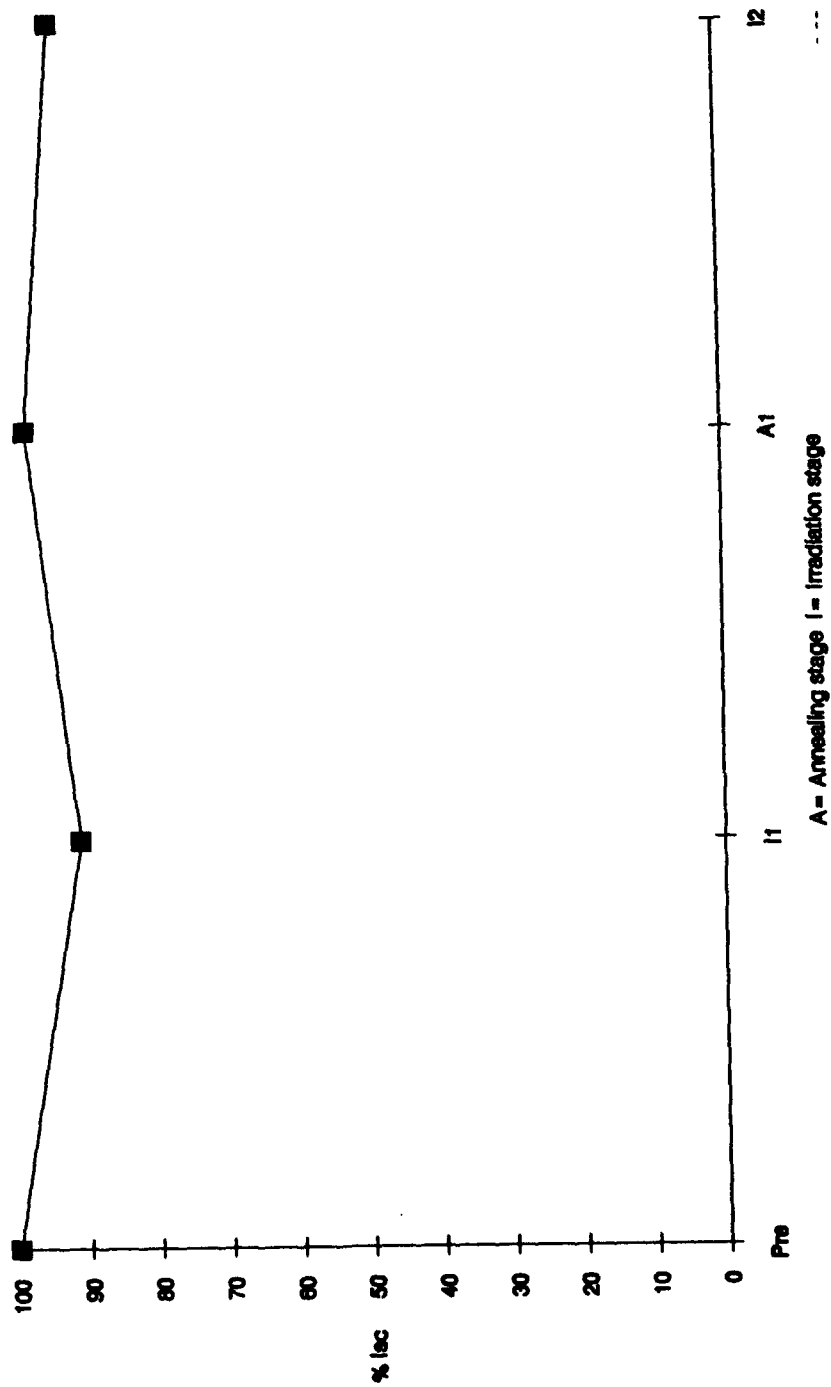


Figure E.2. Normalized I<sub>sc</sub> plot for InP cell No. 1073

IrP #1073

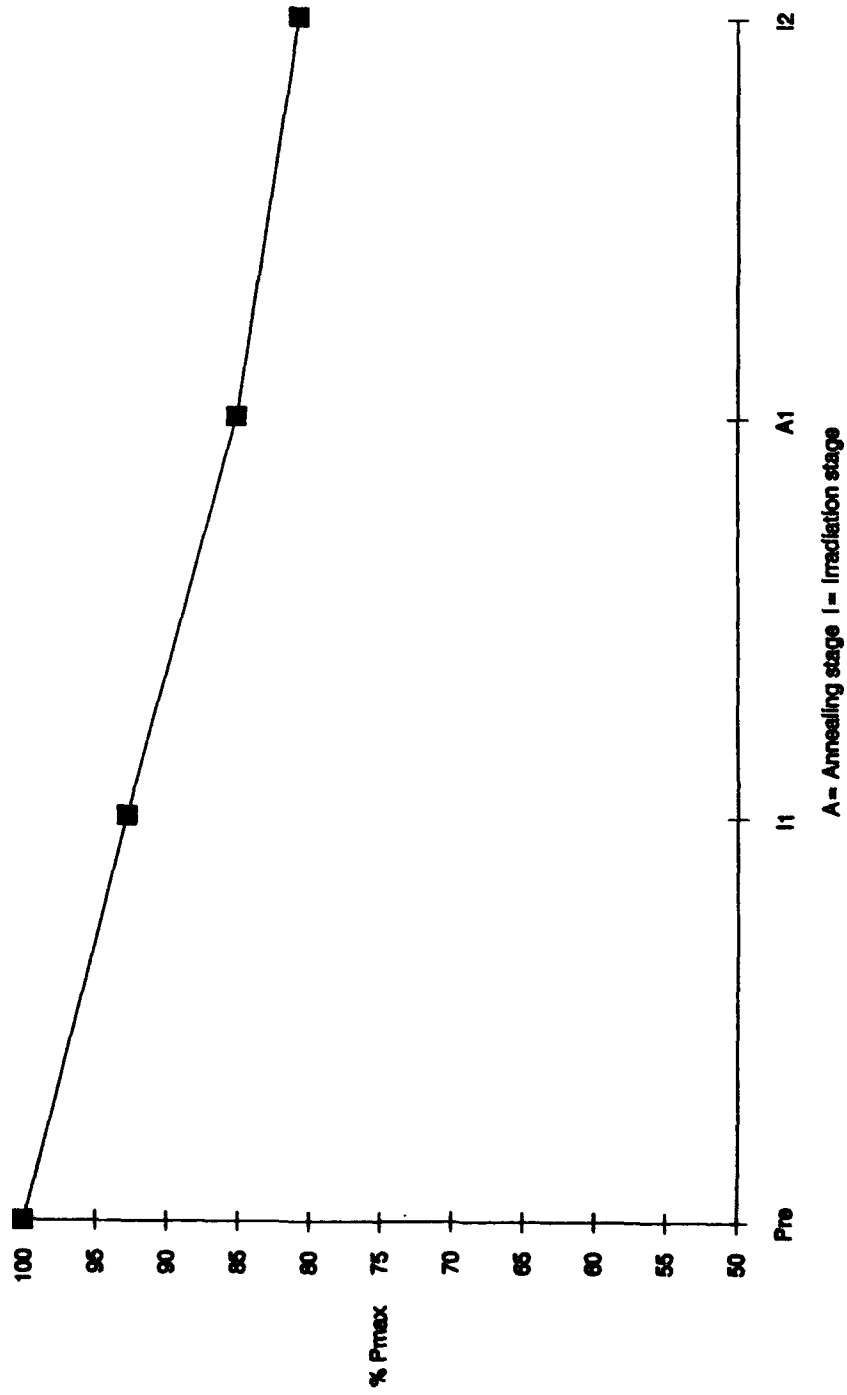


Figure E.3. Normalized P<sub>max</sub> plot of I<sub>np</sub> cell No. 1073



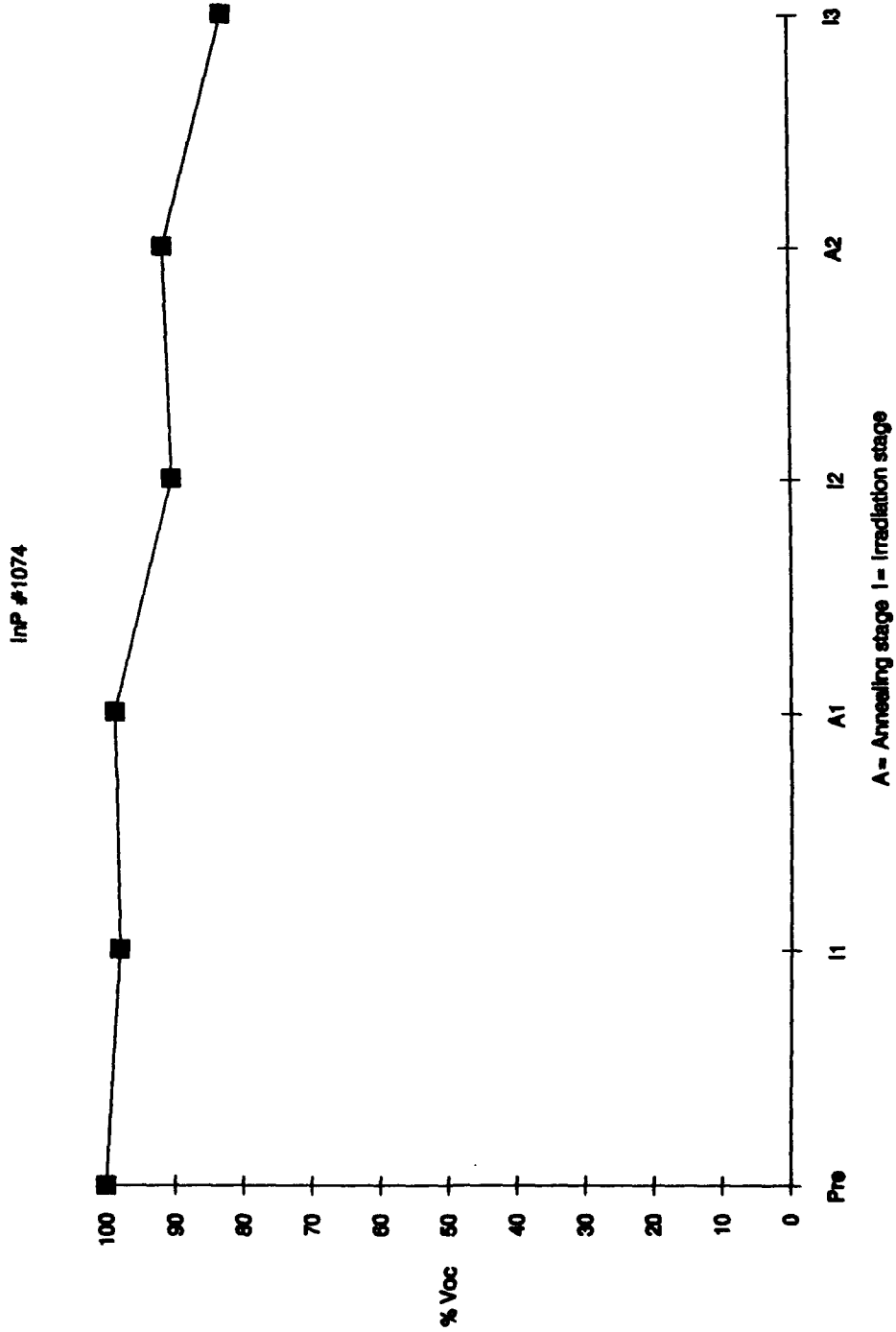


Figure E.4. Normalized  $V_{oc}$  plot of InP cell No. 1074

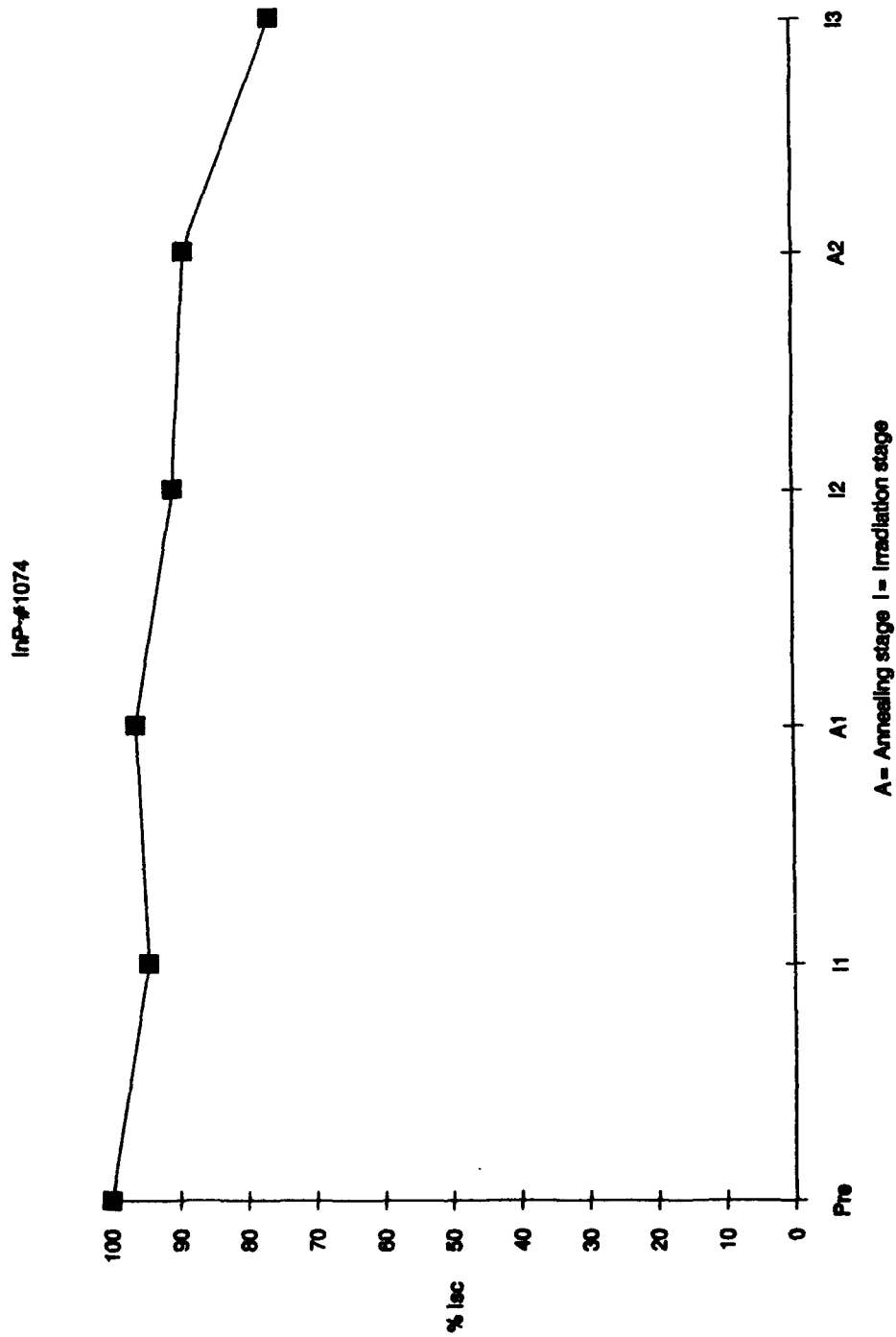


Figure E.5. Normalized  $I_{sc}$  plot for InP cell No. 1074

InP #1074

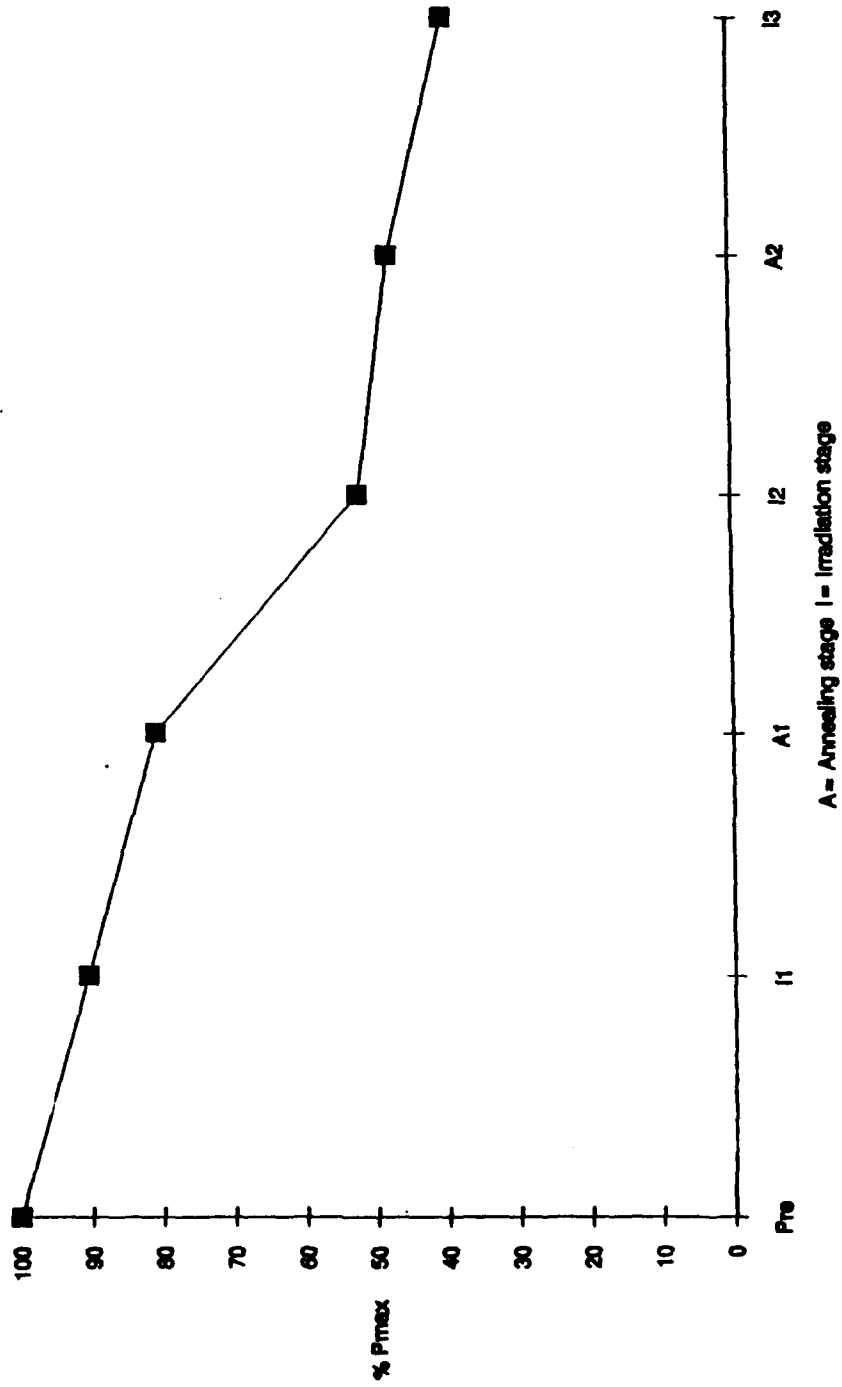


Figure E.6. Normalized  $P_{max}$  plot for InP cell No. 1074

APPENDIX F  
EQUATIONS AND SAMPLE CALCULATIONS FOR DLTS ON InP  
CELL 1073 ALONG WITH ENERGY AND CAPTURE CROSS SECTION PLOTS

The equations used for LDTS calculations in thjis research are based on Refs. 22 and 23 and are listed below.

### Energy Calculation

$$e_p = \frac{1}{\tau}$$

where  $e_p$  = emission rate  
 $\tau$  = 4.3 x delay

delay is the value set on the spectrometer

The energy level of the trap ( $E_t$ ) is a function of the slope of the line of the Arrhenius plot of  $\ln(e_p/T^2)$  vs  $(1/T)$ . Then

$$E_t = \text{slope}/k$$

where  $k$  is Boltzman's constant =  $8.62 \text{ E-}0.5$

### Sigma Calculation (capture cross section)

$$v_T = (3kT/m^*)^{1/2}$$

where

$v_T$  = thermal velocity  
 $m^*$  = effectivenss mass for holes in InP =  $0.4m_0$   
 $m_0$  = free electron mass

A similar plot of  $\ln[1 - (\text{Sig}/S_{\text{max}})]$  versus pulse width where  $S$  is the DLTS signal in volts. Then

slope =  $\sigma n v_T$   
 where  $n$  = carrier concentration (assumed  $6.5\text{E}16 \text{ cm}^{-3}$ )  
 $\sigma$  = capture cross section

### Concentration ( $N_t/N_d$ )

$$N_t/N_d = 2\Delta C_0/C$$

where  $\Delta C_0$  =  $0.6 \times$  DLTS signal in mV  
 $C$  = gain setting x capacitance at peak of signal  
 x 1000  
 $N_d$  = carrier concentration ( $6.5\text{E}16 \text{ cm}^{-3}$ )

	A	B	C	D	E	F	G	H	I	J	K	L	M	N	O	P	Q	R	S
1	InP 1073	Reference																	
2																			
3	Energy	Calculation																	
4																			
5																			
6																			
7																			
8																			
9																			
10																			
11																			
12																			
13																			
14																			
15																			
16																			
17																			
18																			
19																			
20																			
21																			
22																			
23																			
24																			
25																			
26																			
27																			
28																			
29																			
30																			
31																			
32																			
33																			
34																			
35																			

Figure F.1. Sample DLTS calculations for energy level and capture cross section on InP cell No. 1074

	A	B	C	D	E	F	G	H	I	J	K	L	M	N	O	P
36																
37																
38	Concentrations															
39	$40 \text{ Ni/Nd} = 2 \times 10^4 \text{ Co/C} = 2 \times 10^4 \text{ (S}^2\text{Y)} / (10^{-14} \times 1000)$															
41	$41 \text{ S}^2\text{Y} = \text{signal in mV}$															
42		C range =	1000	1000												
43		G =	100	100												
44																
45																
46		$\text{S}^2\text{Y (rms)}$	100	$4.27E+02$												
47		MA	0.034	0.498												
48																
49		$\text{Ni/Co/C}$	$1.36E-03$	$1.83E-02$												
50		$\text{Ni/Nd}$	$2.76E-03$	$3.67E-02$												
51																
52		suppose Nd =	$6.8E+16$													
53		then Ni/Nd =	$1.0E+14$	$2.36E+15$												
54																

Figure F.2. Sample DLTS calculations for trap concentration levels on InP cell No. 1073

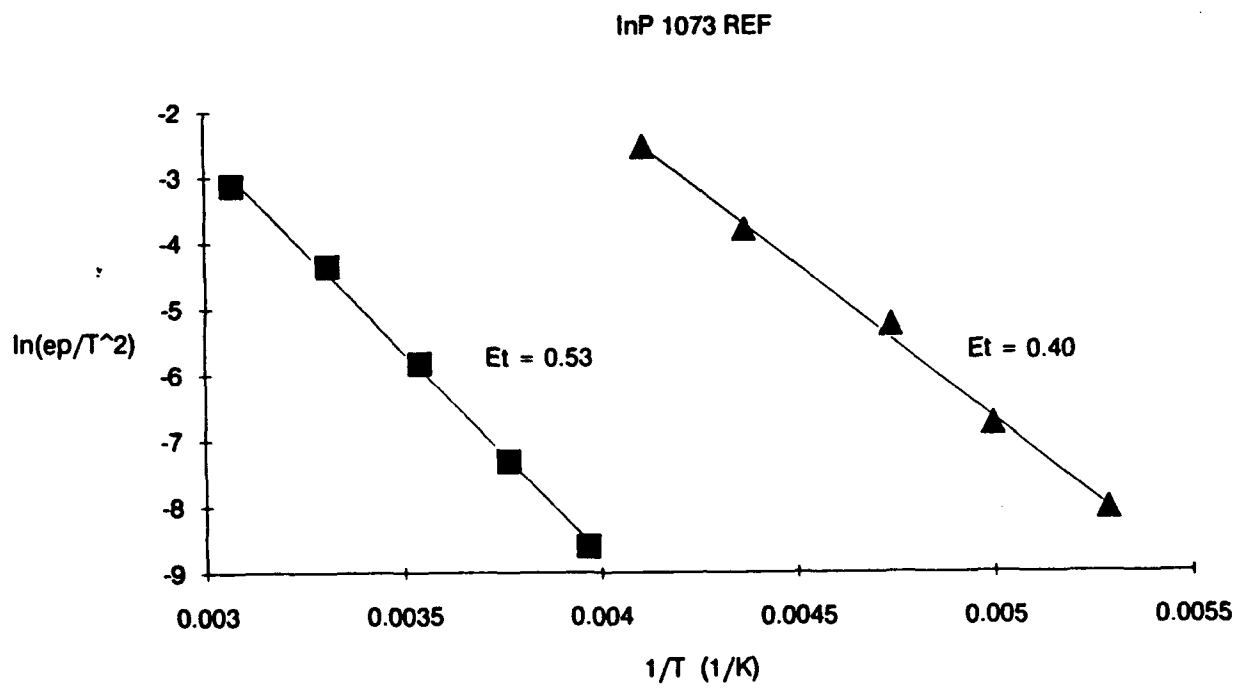


Figure F.3. Energy level Arrhenius plot for InP cell No. 1073 reference



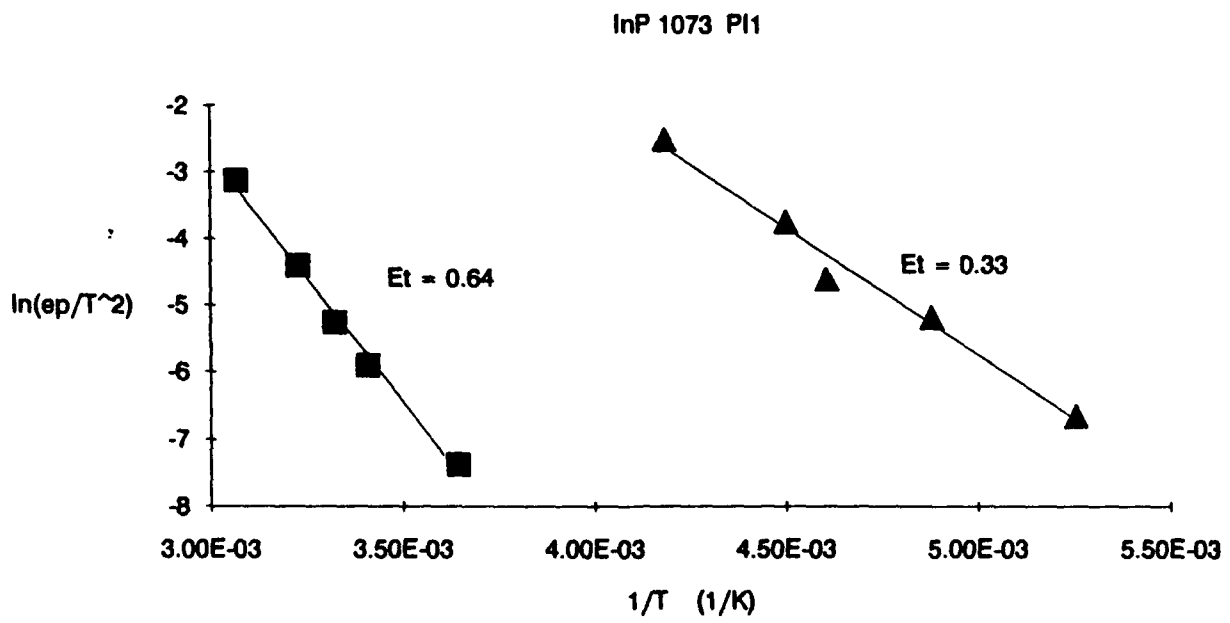


Figure F.4. Energy level Arrhenius plot for InP cell No. 1073 post irradiation 1

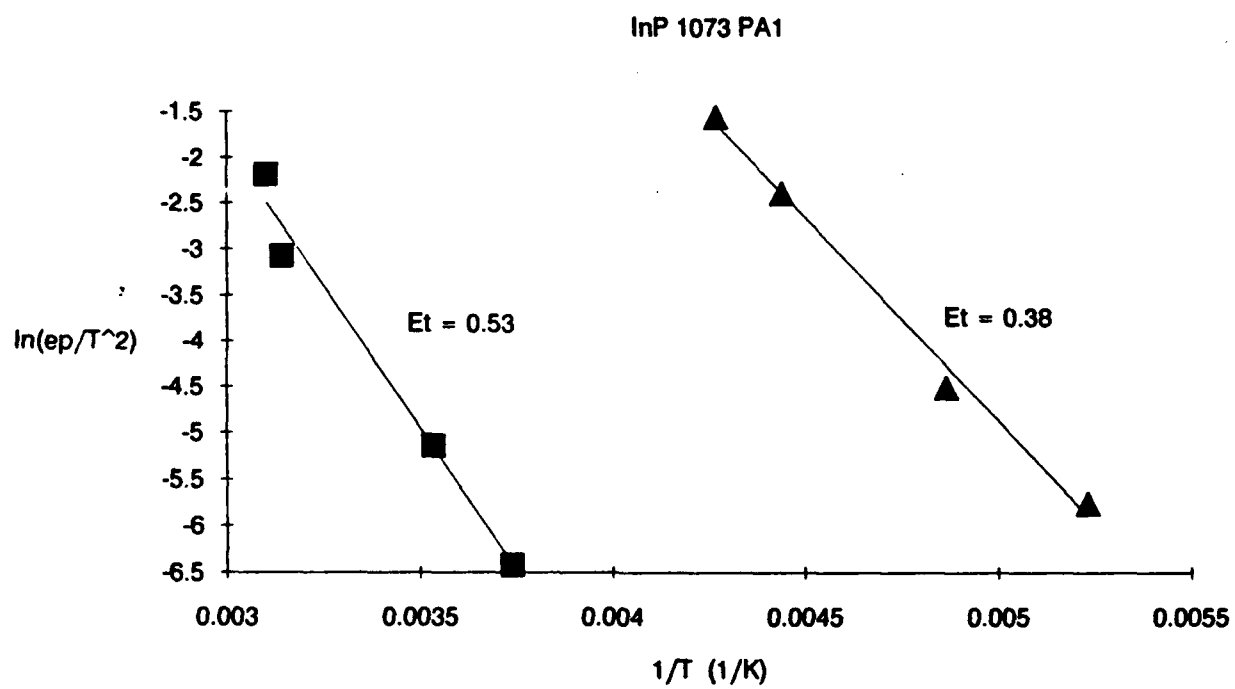


Figure F.5. Energy level Arrhenius plot for InP cell No. 1073 post anneal 1

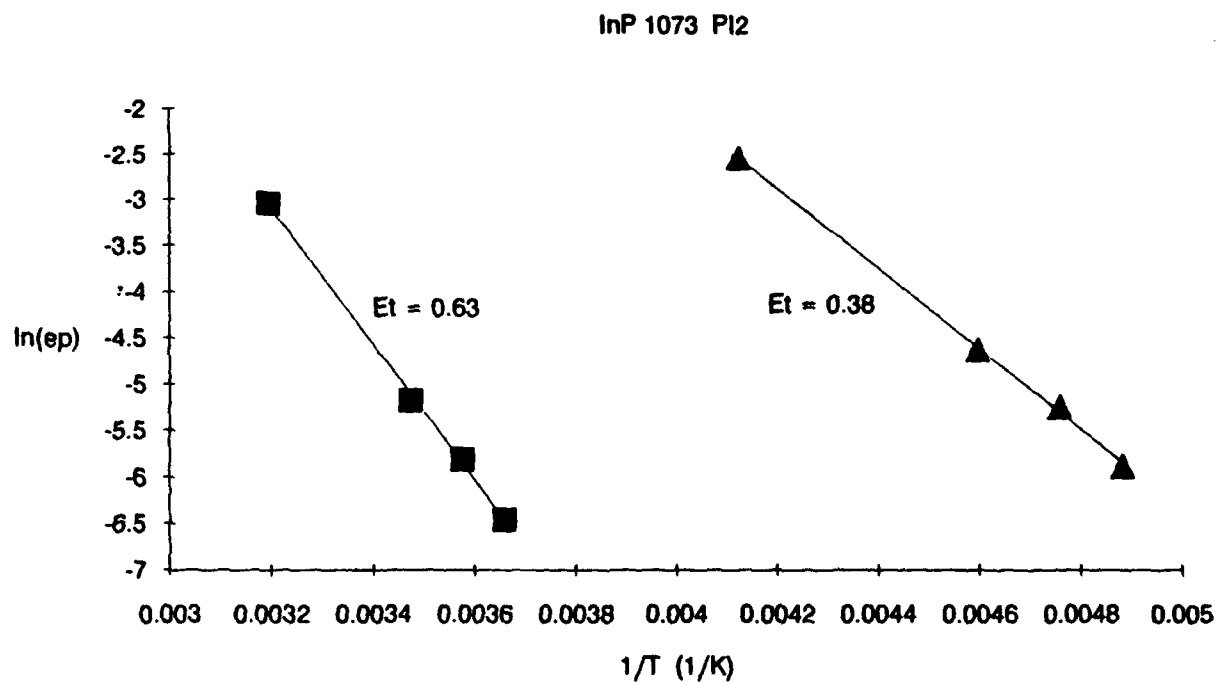


Figure F.6. Energy level Arrhenius plot for InP cell No. 1073 post irradiation 2

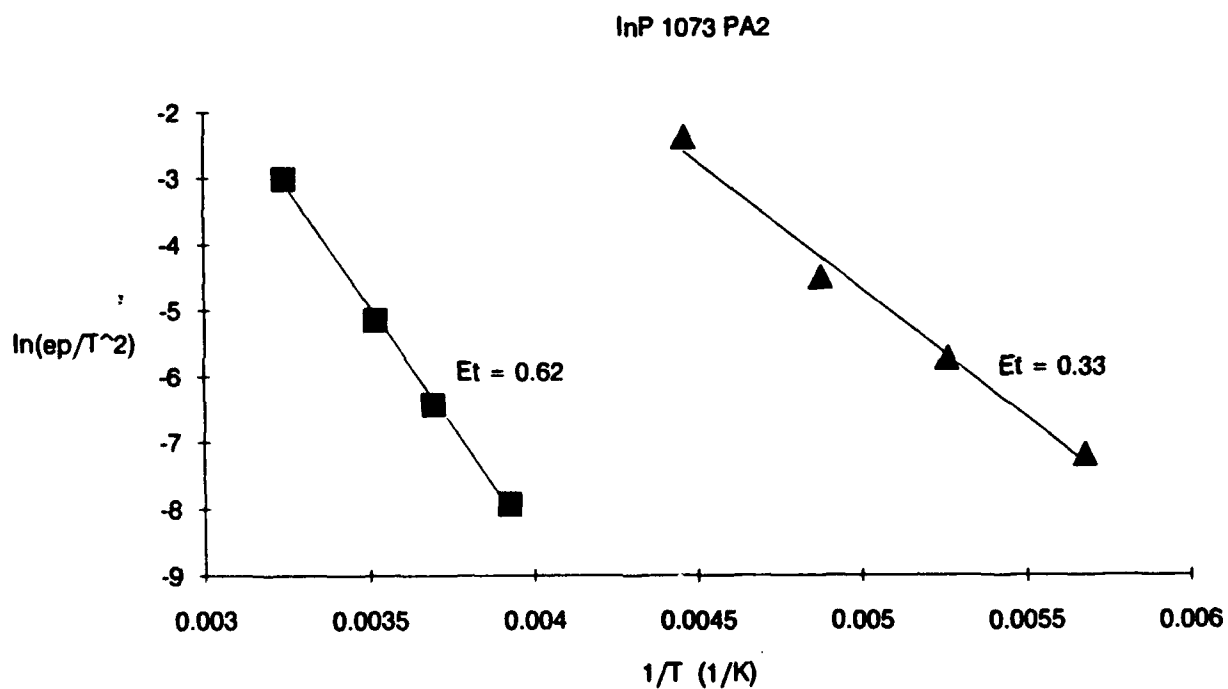


Figure F.7. Energy level Arrhenius plot for InP cell No. 1073 post anneal 2

InP 1073 REF Sigma Calculation

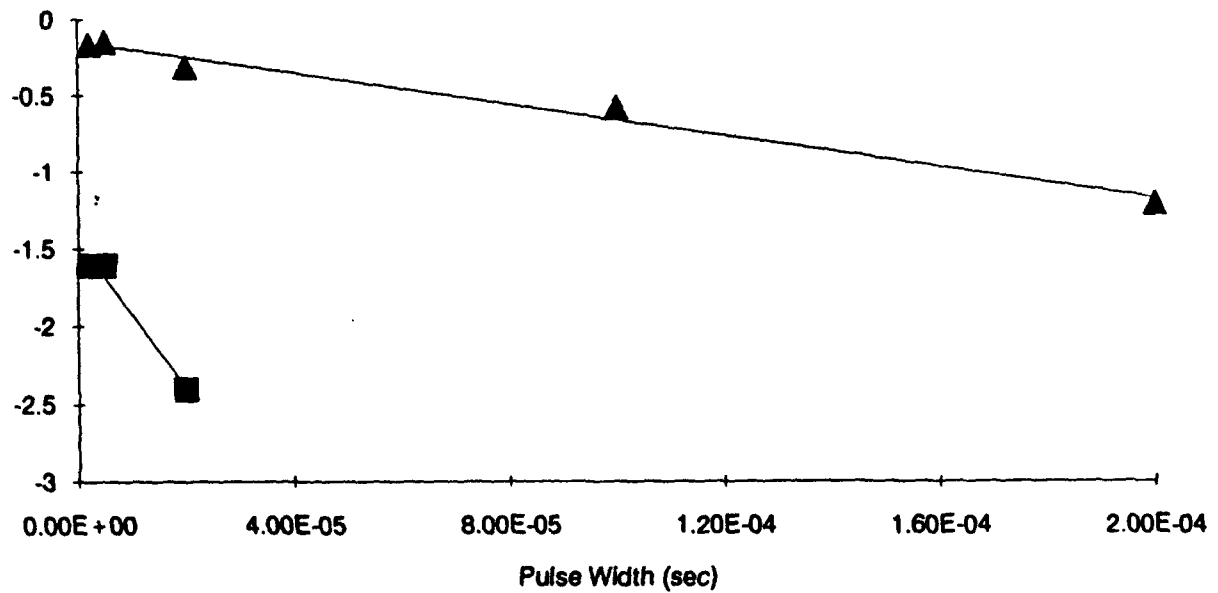


Figure F.8. Capture cross section plot of InP cell No. 1073 reference

InP 1073 PI1 Sigma Calculation

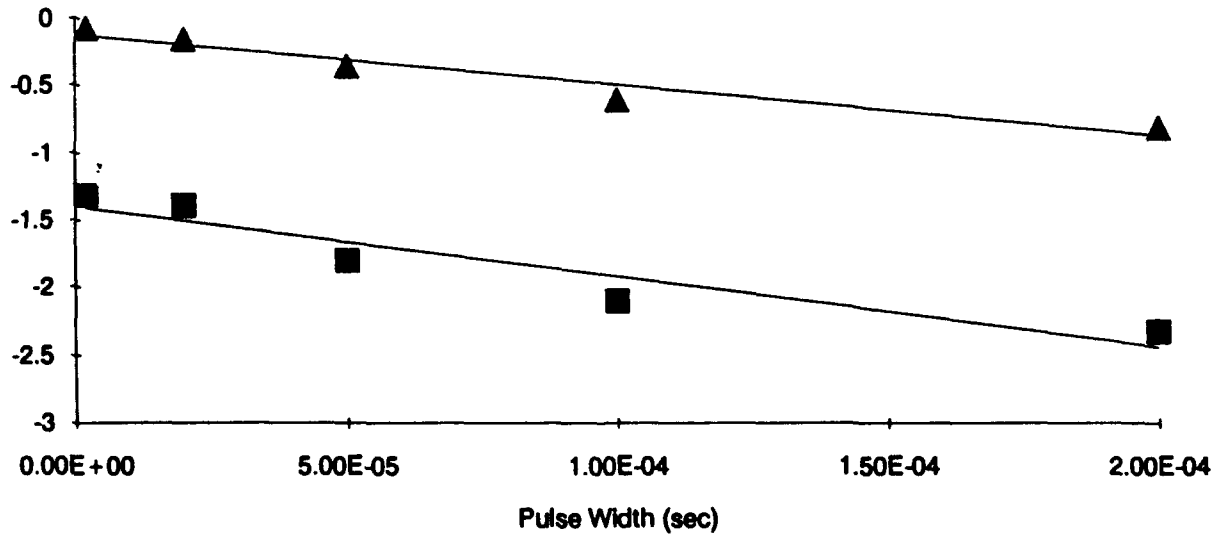


Figure F.9. Capture cross section plot of InP cell No. 1073 post irradiation 1

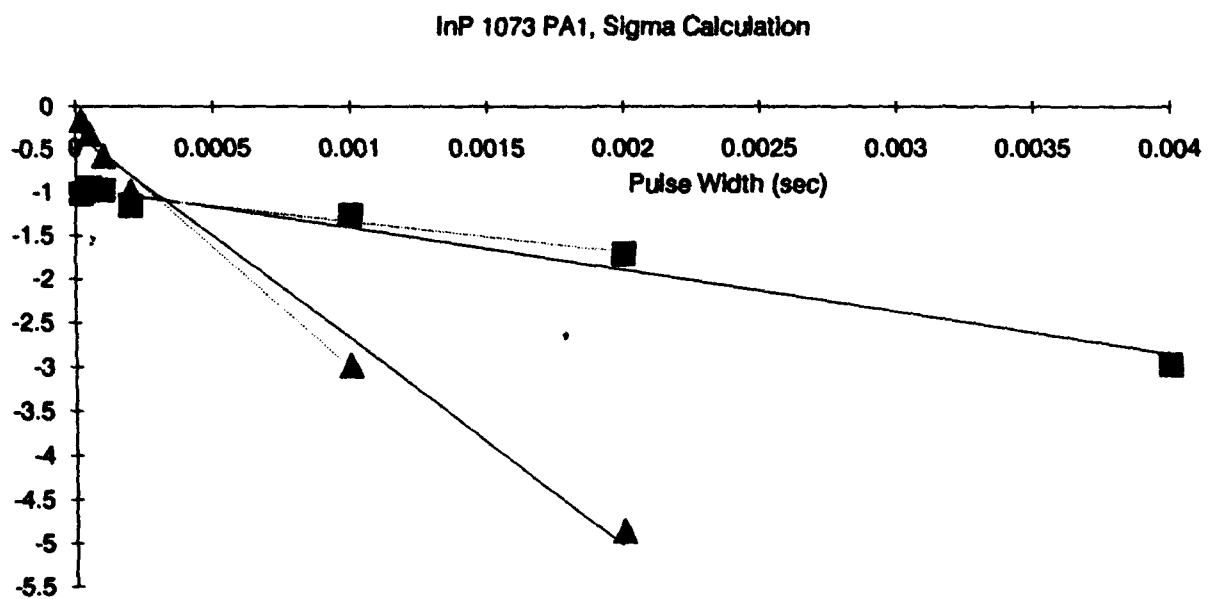


Figure F.10. Capture cross section plot of InP cell No. 1073 post anneal 1

InP 1073 P12, Sigma Calculation

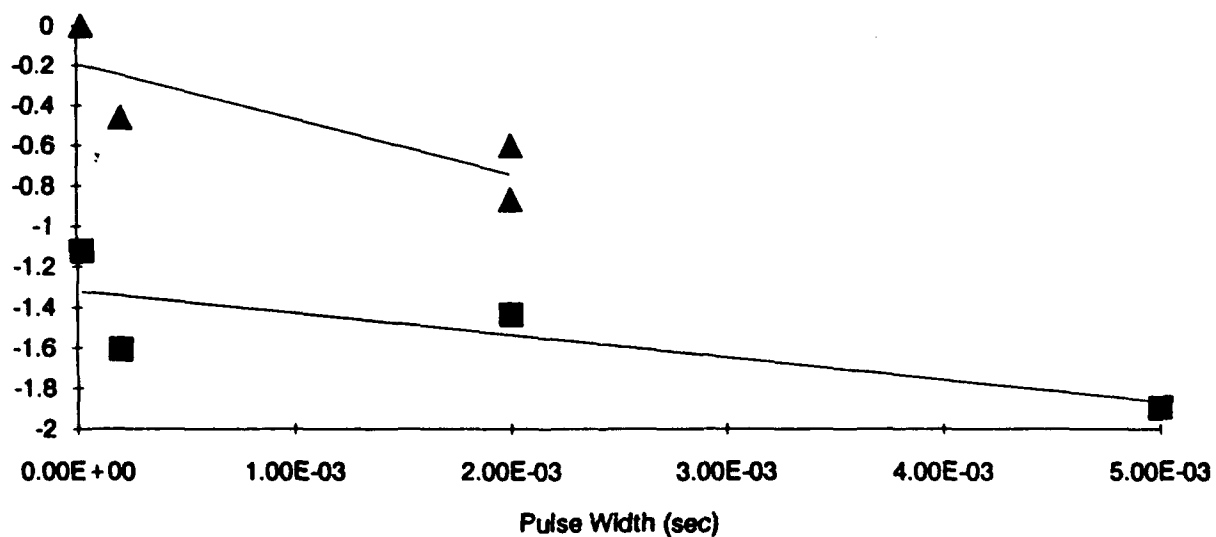


Figure F.11. Capture cross section plot of InP cell No. 1073 post irradiation 2



InP 1073 PA2 Sigma Calculation

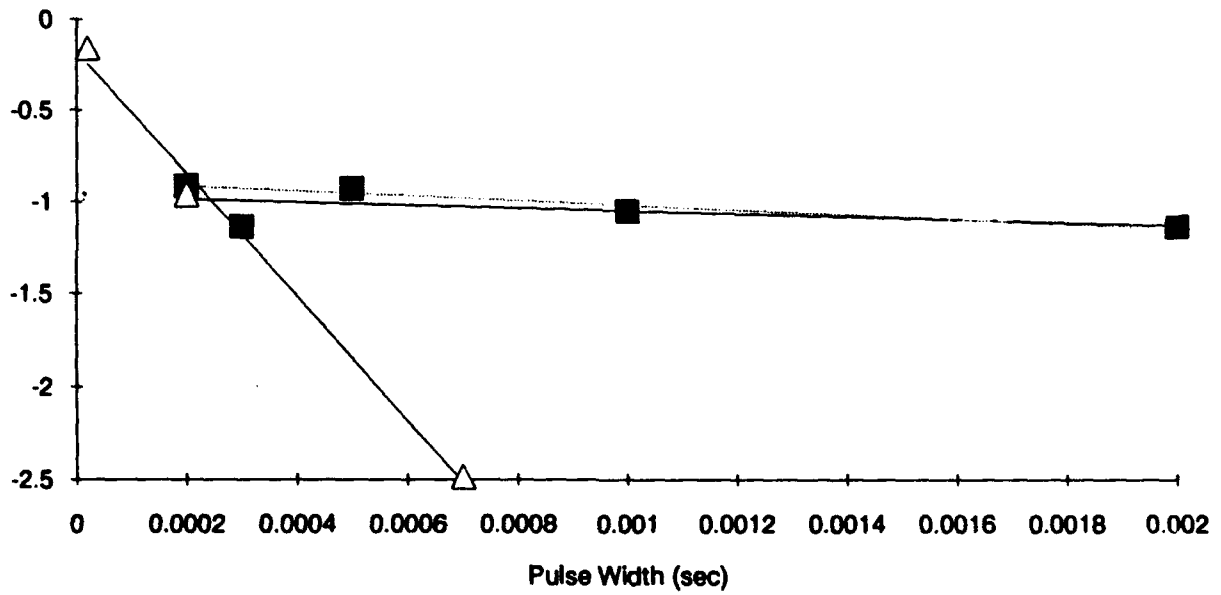


Figure F.12. Capture cross section plot of InP cell No. 1073 post anneal 2

## REFERENCES

1. Clark, T.F., An Experimental Test of Minority Carrier Annealing on GaAs Solar Cells Using Forward Biased Current, Master's Thesis, Naval Postgraduate School, Monterey, CA, September 1986.
2. Cypranowski, C., Power Recovery of Radiation-Damaged Gallium Arsenide and Indium Phosphate Solar Cells, Master's Thesis, Naval Postgraduate School, Monterey, CA, December 1989.
3. Staats, R.L., Forward-Biased Current Annealing of Radiation Damaged Gallium Arsenide and Silicon Solar Cells, Master's Thesis, Naval Postgraduate School, Monterey, CA, September 1987.
4. Brick, R.M., Gordon, R.B., Phillips, A., Structure and Properties of Alloys, McGraw-Hill Book Company, 1965.
5. Sze, S.M., Physics of Semiconductor Devices, John Wiley and Sons, 1981.
6. Fahrenbruch, A.L., Bube, R.H., Fundamentals of Solar Cells, Academic Press, 1983.
7. Hu, C., White, R.M., Solar Cells: From Basics to Advanced Systems, McGraw-Hill Book Company, 1983.
8. Solar Energy Research Institute, Photovoltaics, Technical Information Guide, Van Nostrand Reinhold Co., 1984.
9. Solar Energy Research Institute, Basic Photovoltaic Principles and Methods, Van Nostrand Reinhold Co., 1984.
10. Green, M.A., Solar Cells, Prentice Hall, 1982.
11. Azaroff, L.V., Brophy, J.J., Electronic Processes in Materials, McGraw-Hill Book Company, 1963.
12. JPL Publication 43-48, Solar Cell Array Design Handbook Vol. 1, October 1976.
13. JPL Publication 82-69, Solar Cell Radiation Handbook, Third Edition, November 1982.
14. Hovel, H.J., Semiconductors and Semimetals, Vol II, Solar Cells, Academic Press, 1975.
15. Larin, F., Radiation Effects in Semiconductor Devices, John Wiley and Sons, 1968.

16. Agrawal, B.N., Design of Geosynchronous Spacecraft, Prentice-Hall, 1986.
17. Loo, R., Knechtli, R.C., Kamath, G.S., Enhanced Annealing of GaAs Solar Cell Radiation Damage, Fourteenth IEEE Photovoltaic Specialists Conference, pp. 33-37, 1981.
18. Stievenard, D., Bourgoin, J.C., Degradation and Recovery of GaAs Solar Cells Under Electron Irradiation, Seventeenth IEEE Photovoltaic Specialists Conference, pp. 1103-1107, 1984.
19. Lang, D.V., Deep-Level Transient Spectroscopy: A New Method to Characterize Traps in Semiconductors, Journal of Applied Physics, Vol. 45, No. 7, July 1979.
20. Sheng, S. Li, Wang, W.L., Lou, R.Y., and Rahilly, W.P., Deep Level Defects and Annealing Studies in One-MeV Electron Irradiated (AlGa)As - GaAs Solar Cells, Sixteenth Photovoltaic Specialists Conference, pp. 211-215, 1982.
21. Yamaguchi, M. and Ando, K., Mechanism for Radiation Resistance of InP Solar Cells, Journal of Applied Physics, vol. 63, No. 11, June 1988.
22. Sula Technologies, Short Form DLTS Operating Manual, Preliminary version, March 1986.
23. Barnes, C.E., Materials Research Society Short Course on Deep Level Transient Spectroscopy, Aerospace Corporation, April 1987.
24. Chung, M.A., Meier, D.L., Szedon, J.R., and Bartleto, J., Electron Irradiation and Annealing of MDCVD GaAs and GaAs/Ge Solar Cells, IEEE, pp. 924-929, 1988.
25. Johnson, N.M., Deep-Level Transient Spectroscopy: Characterization and Identification of Electronic Defects, Optical Engineering, Vol. 25, No. 5, May 1986.
26. Kreider, J.F., Kreith, F., Solar Energy Handbook, McGraw-Hill Book Company, 1981.
27. Friedman, H., Sun and Earth, Scientific American Library, 1986.
28. Chopra, K.L., Das, S.R., Thin Film Solar Cells, Plenum Press, 1983.
29. Fonash, S.J., Solar Cell Device Physics, Academic Press, 1981.

30. Richtmyer, F.K., Kennard, E.H., Cooper, J.N., Introduction to Modern Physics, McGraw-Hill Book Company, 1969.

31. Michael, S., EO 3740 class notes, "Space Power and Radiation Effects," Naval Postgraduate School, Monterey, CA

INITIAL DISTRIBUTION LIST

Defense Technical Information Center Cameron Station Alexandria, VA 22304-6145	2
Library, Code 52 Naval Postgraduate School Monterey, California 93943-5002	2
Chairman, Code EC Department of Electrical and Computer Engineering Naval Postgraduate School Monterey, California 93943-5000	1
Prof. Sherif Michael, Code EC/Mi Department of Electrical and Computer Engineering Naval Postgraduate School Monterey, California 93943-5000	2
Space Systems Academic Group Prof. R. Panholzer, Code SP Naval Postgraduate School Monterey, California 93943-5000	1
Commandant of the Marine Corps Code TE-06 Headquarters US Marine Corps Washington, DC 20360-0001	1
Dr. Bruce E. Anspaugh Jet Propulsion Laboratory 4800 Oak Grove Drive Pasadena, California 91109	1
Dr. Linda Halle Aerospace Corporation 270 Coral Circle M2/275 EXT 65215 El Segundo, California 90245	1
Dr. Joseph L. Capitano Applied Solar Energy Corporation 15251 E. Don Julian Road City of Industry, California 91749	1
MAJ Dimas Pinzon 2 Dutchess Drive Orangeburg, New York 10962	3